eman ta zabal zazu

Universidad del País Vasco
Euskal Herriko Unibertsitatea

Fabrication and characterization of magnetic thin films and multilayers

Lorenzo Fallarino

- PhD Thesis-

Supervisor: Dr. Andreas Berger

2017


CIC
nanoGUNE
nanoscience cooperative research center

E ti diranno parole rosse come il sangue nere come la notte
Ma non è vero, ragazzo che la ragione sta sempre col più forte
Io conosco poeti che spostano i fiumi con il pensiero
E naviganti infiniti che sanno parlare con il cielo
Chiudi gli occhi, ragazzo e credi solo a quel che vedi dentro
Stringi i pugni, ragazzo
Non lasciargliela vinta neanche un momento
Copri l'amore, ragazzo
Ma non nasconderlo sotto il mantello
A volte passa qualcuno
A volte c'è qualcuno che deve vederlo
Sogna, ragazzo sogna
Quando sale il vento
Nelle vie del cuore
Quando un uomo vive
Per le sue parole
O non vive più
Sogna, ragazzo sogna
Non lasciarlo solo contro questo mondo
Non lasciarlo andare sogna fino in fondo
Fallo pure tu!

Roberto Vecchioni

Resumen

En la actualidad, el estudio de nuevos fenómenos físicos que aparecen cuando los sistemas magnéticos se reducen a la nano-escala está dando lugar a impresionantes descubrimientos científicos. Es por tanto una cuestión clave entender y controlar estos fenómenos magnéticos en los sistemas nanométricos. Entre las principales preguntas que esperan respuesta y que están relacionadas con este proyecto de tesis, se encuentran dos aspectos de relevancia fundamental y tecnológica. Por un lado, el desarrollo de metodologías y herramientas avanzadas para la fabricación de películas y multicapas magnéticas de alta calidad y con alta reproducibilidad. Estas deberían estar ordenadas cristalográficamente, para un futuro empleo en la fabricación de nano-estructuras magnéticas funcionales de alta calidad. Por otro lado, esta tesis tiene como objetivo la comprensión y modelización de los fenómenos magnéticos a dichas escalas de longitud y tiempo en sistemas sujetos a diversas interacciones que compiten entre sí.

Tal comprensión es de crucial importancia y también es clave para identificar nuevas direcciones y caminos que permitan superar las limitaciones actuales en varios campos tecnológicos. Además, es necesaria para el desarrollo de una visión física coherente para alcanzar una sólida comprensión de los mecanismos que gobiernan el magnetismo. Las propiedades magnéticas de los materiales a la nano-escala están siendo investigadas exhaustivamente con una amplia variedad de técnicas experimentales, y los esfuerzos dedicados a su estudio son cada vez mayores para el desarrollo de nuevas herramientas tecnológicas.

Este trabajo de tesis presenta los resultados de la investigación llevada a cabo en cuatro años de doctorado y está organizado en seis capítulos. El primer capítulo presenta los conceptos básicos de los fenómenos físicos estudiados en esta tesis. La sección uno revisa los aspectos fundamentales del Ferromagnetismo e ilustra el modelo de macrospin utilizado para describir la dinámica de inversión de la magnetización en películas y multicapas magnéticas. La segunda sección presenta el Antiferromagnetismo y el concepto básico de magnetización de superficie, característica que posee el sesquióxido de cromo Cr_2O_3.

En el segundo capítulo se describen los equipos empleado para fabricar y caracterizar las muestras estudiadas en esta tesis. Estas muestras se han fabricado en un sistema de pulverización catódica desarrollado por AJA Internacional Inc, el cual permite utilizar tanto corriente continua (DC), para capas metálicas, como corriente alterna (RF), para capas aislantes. Para la caracterización de la estructura cristalina y la medición del espesor de las películas se ha usado la técnica de difracción y reflectividad de rayos-X. Las mediciones magnéticas presentadas en esta tesis se han llevado a cabo por medios de técnicas de magnetometría de muestra vibrante (VSM), dispositivos superconductores de interferencia cuántica (SQUIDs), microscopia magneto-óptica de efecto Kerr y de microscopía de fuerza magnética (MFM). Además, se ha utilizado la espectrometría de neutrones polarizados (PNR) con el propósito de medir las transiciones de fase ferromagnéticas en películas delgadas diseñadas para obtener un gradiente de la energía de canje.

El capítulo tres presenta el estudio de las propiedades magnéticas de películas delgadas epitaxiales de aleaciones de cobalto y cromo y su dependencia de la composición y temperatura. Dichas muestras presentan una composición que posee un perfil de profundidad similar al de una "bañera", específicamente siguiendo la secuencia de capas $Co/Co_{1\rightarrow 1-x_c}Cr_{0\rightarrow x_c}/Co_{1-x_c}Cr_{x_c}/Co_{1-x_c\rightarrow 1}Cr_{x_c\rightarrow 0}/Co$, con la concentración más alta de Cr (x_c) en el centro de la muestra (Fig. R.1(a,b)).

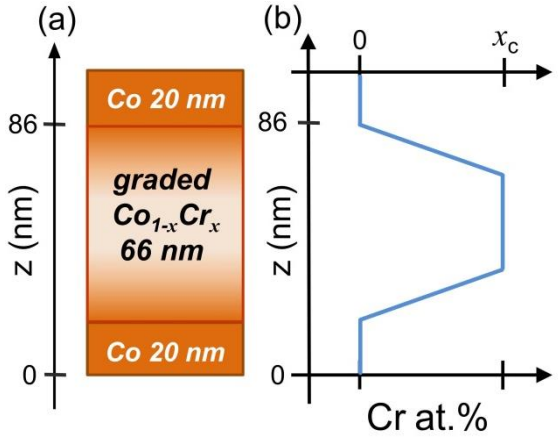

Figura R1: (a) esquemática de la secuencia de crecimiento de las capas magnéticas, mientras (b) muestra el perfil de Cr a lo largo del eje z, perpendicular a la superficie de la muestra, para el tipo de estructuras estudiada en este trabajo.

El estudio por medio de reflectometría de neutrones polarizados, llevado a cabo en el centro de investigación NIST-NCNR por el Dr. Brian J. Kirby, muestra que la temperatura de Curie varía en función de la profundidad y presenta su mínimo en el centro de la estructura, donde la concentración de cromo es máxima (Fig. R1(a,b)). En consecuencia, se ha observado que el acoplamiento efectivo entre las dos capas exteriores de Co es fuertemente dependiente del perfil de la magnetización de la capa intermedia de CoCr. Además, este acoplamiento se puede ajustar de forma continua a través de x_c y de la temperatura externa T. En particular, para $x_c = 0.28$, la magnetometría SQUID revela que en función de la temperatura la inversión de la magnetización se da por medios de dos procesos diferentes: para temperaturas T < 260 K la inversión ocurre en un paso, mientras que para T > 260 K se da en dos pasos. Esto indica una transición desde un sistema magnético totalmente correlacionado a baja temperatura a un sistema desacoplado que contiene dos subcapas magnéticas casi independientes. Las medidas de PNR obtenidas para la muestra $x_c = 0.28$ corroboran estas hipótesis, lo que demuestra que por medio de la temperatura y del campo magnético externo se puede controlar la aparición de una alineación antiparalela de la magnetización de las dos capas externas de cobalto.

En el cuarto capítulo, se ha estudiado el proceso de inversión de la magnetización en función de la temperatura y del ángulo de aplicación del campo magnético externo en muestras de cobalto y cobalto-rutenio que tienen una anisotropía magnetocristalina perpendicular a la superficie.

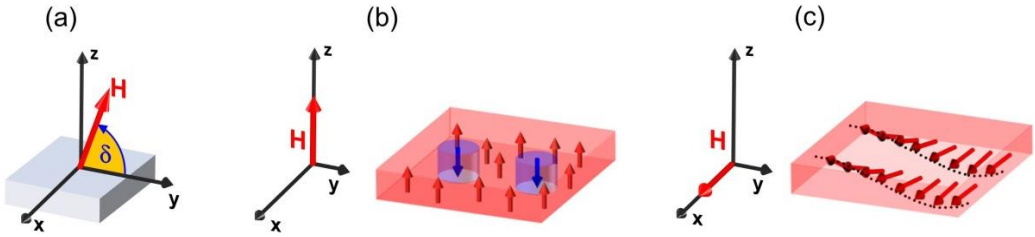

Figura R2: (a) orientación del campo magnético con respecto al plano de la muestra; (b) esquemática que muestra el proceso de nucleación de dominios; (c) inestabilidad del estado uniforme.

A temperatura ambiente, la caracterización magnética en muestras de cobalto revela dos mecanismos de inversión de magnetización. Para ángulos del campo aplicado δ (Fig. R2(a)) cercanos a δ=90°, i.e. perpendicular a la superficie de la muestra, la inversión de la magnetización se lleva a cabo por medio de nucleación de dominios (Fig. R2(b)), mientras

que para orientaciones del campo magnético en el plano de la muestra ($\delta = 0°$), la inversión de la magnetización se da a través de la inestabilidad del estado magnético uniforme (Fig. R2(c)). Mediciones en función de la temperatura han permitido la modificación de la anisotropía magnetocristalina. Esto ha revelado la desaparición gradual del proceso de nucleación de dominios durante la inversión de la magnetización para temperaturas elevadas, para las cuales la inversión se da exclusivamente por medio de la inestabilidad del estado uniforme para todas las orientaciones de campo.

Para verificar que en el régimen a alta temperatura las muestras de cobalto siguen teniendo una orientación preferencial de la magnetización fuera del plano, se han llevado a cabo mediciones magnéticas comparativas de muestras de aleación de $Co_{90}Ru_{10}$ a temperatura ambiente. Estas imitan el comportamiento a alta temperatura del cobalto, permitiendo un estudio a condiciones accesibles experimentalmente por nuestro sistema MFM. Así se ha identificado y confirmado que el estado de magnetización remanente del cobalto a alta temperatura corresponde a dominios magnéticos a rayas típicos en materiales con anisotropía magnética perpendicular a pesar de la reducción de la anisotropía magnetocristalina. Asimismo, detalladas simulaciones micromagnéticas, realizadas por el Prof. Dr. Ondrej Hovorka (Universidad de Southampton, UK), han complementado los resultados experimentales y corroborado la comprensión física del comportamiento magnético en función de la temperatura. Por otra parte, estas también han permitido una identificación completa del complejo balance energético en películas magnéticas con anisotropía magnética perpendicular, debido al cual se producen tres fases magnéticas diferentes para valores suficientemente altos de anisotropía, cuyo punto de coexistencia es tricritico en su naturaleza.

En la capitulo cinco, se ha estudiado la posibilidad de inducir la inversión de la magnetización de superficie por medio del campo magnético en el óxido de cromo Cr_2O_3 orientado (0001). Esto se ha hecho mediante magnetometría SQUID, estudiando películas delgadas de diferentes grosores. De hecho, el óxido de cromo es conocido por poseer una magnetización de equilibrio neta en la superficie (0001), llamada magnetización de superficie (BM), que está totalmente acoplada al parámetro de orden antiferromagnético del material. La inversión exclusivamente por medios magnéticos se ha evidenciado experimentalmente en películas suficientemente delgadas a diferencia de películas muy

gruesa donde la inversión requiere la aplicación simultánea de campos eléctricos y magnéticos.

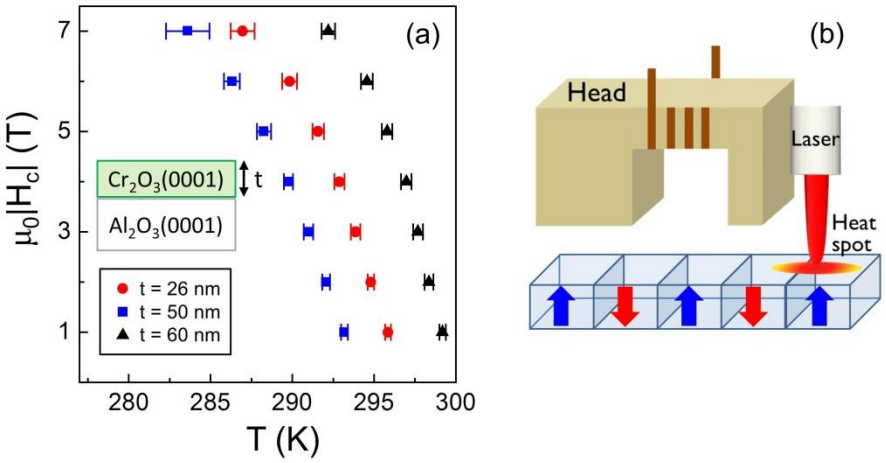

Figura R3: (a) campo coercitivo de la magnetización de superficie en función de la temperatura; (b) esquemática elemental de la técnica de grabación magnética asistida por calor.

Además, este material, que es antiferromagnético por debajo de T_N = 307 K, muestra en capas finas una dependencia gigante en temperatura del campo coercitivo, fluctuando en unos teslas en pocos grados de temperatura (Fig. R3(a)). Este efecto resultaría ser óptimo para una prometedora técnica de memorias magnéticas, llamada grabación magnética asistida por calor (HAMR) (Fig. R3(b)), la cual consiste en almacenar datos en medios de alta estabilidad térmica con la ayuda de un láser para calentar el material.

Con el fin de poder modificar la temperatura crítica de estos materiales y de verificar si esta magnetización de superficie puede persistir en aleaciones, se ha investigado el impacto de la dilución de películas delgadas de Cr_2O_3 con el isoestructural Al_2O_3. Se han fabricado películas epitaxiales delgadas de $Cr_{2-x}Al_xO_3$ con orientación (0001) en el rango de concentración $0 \leq x \leq 0.6$. Para estas muestras, se ha encontrado que se preservan la estructura cristalina corindón, el orden antiferromagnético, y, lo más importante, la magnetización de superficie. También se ha observado que la temperatura crítica T_N se puede modificar mediante la aleación con Al_2O_3, utilizando la BM como una sonda para estudiar la transición de fase antiferromagnética. Por otra parte, ha sido posible evaluar el exponente crítico y los valores absolutos de magnetización de superficie para diferentes muestras. Ambas propiedades corroboran que las señales magnéticas observadas se originan de la BM en lugar de la mayor parte de las muestras.

El capítulo final resume los resultados presentados en esta tesis, planteando nuevos retos y proyectos relacionados con los estudios desarrollados, con el fin de abordar experimentalmente nuevas cuestiones fundamentales de interés científico y tecnológico.

Abstract

This thesis studies in detail the fabrication of epitaxial thin films, alloys and multilayers and their structural and magnetic characterization. Several topics are covered, but the primary focus lies in the investigation and optimization of magnetic properties of various sputter deposited metal and oxide thin-film structures by alloying with different materials.

As multiple topics are to be covered, this thesis is sub-divided into three parts: (i) an innovative and timely study of the effect of compositional gradients being transferred into depth dependent magnetic states in structures that are dominated by ferromagnetic exchange coupling; (ii) an extensive experimental and theoretical investigations of the magnetization reversal behavior as a function of field strength, field orientation and temperature on high-quality epitaxial thin-film structures with perpendicular magnetic anisotropy (PMA); (iii) a thorough investigation of the structural and magnetic properties of epitaxial magnetoelectric antiferromagnetic oxide materials.

The first part of the thesis presents the study of the compositional and temperature dependent magnetic properties of epitaxial CoCr thin films. Their composition has a designed bathtub-like depth profile $Co/Co_{1\rightarrow 1-x_c}Cr_{0\rightarrow x_c}/Co_{1-x_c}Cr_{x_c}/Co_{1-x_c\rightarrow 1}Cr_{x_c\rightarrow 0}/Co$ with the highest Cr concentration (x_c) at the center of the sample. Polarized neutron reflectometry (PNR), conducted together with Dr. Brian J. Kirby (research beam scientist at NIST Center for Neutron Research), shows that the effective Curie temperature varies as a function of depth and, as intended, exhibits a minimum in the center of the structure. Correspondingly, the effective coupling between the two outer Co layers has been observed to be strongly dependent on the magnetization of the graded CoCr spacer and can be continuously tuned via x_c or temperature T. In particular, for $x_c = 0.28$, magnetometry reveals a transition from one-step to two-step magnetization reversal behavior at $T = 260$ K, indicating a transition from a fully correlated magnetic structure to an uncoupled system containing effectively two independent magnetic sublayers. Corroborating evidence of the temperature dependent coupling of the top and bottom regions for $x_c = 0.28$ was revealed by PNR, which demonstrated the field dependent occurrence of antiparallel magnetization alignment on opposite interfaces at sufficiently high temperatures only.

In the second part, the magnetization reversal process of *hcp* (0001) oriented Co and $Co_{90}Ru_{10}$ thin films with perpendicular magnetic anisotropy has been studied as a function of temperature and applied magnetic field angle. Room temperature magnetic characterization reveals two characteristic reversal mechanisms for pure Co. For angles near in-plane field orientation, the magnetization reversal is found to proceed via an instability of the uniform magnetic state, whereas in the vicinity of the out-of-plane orientation, magnetization inversion takes place by means of domain nucleation. Temperature dependent measurements enable the modification of the magnetocrystalline anisotropy and reveal a gradual disappearance of the domain nucleation process during magnetization reversal for elevated temperatures. Ultimately, this suppression of the domain nucleation process leads to the exclusive occurrence of uniform state instability reversal for all field orientations at sufficiently high temperature. Comparative magnetic measurements of $Co_{90}Ru_{10}$ alloy samples allow the identification and confirmation of the high temperature remanent magnetization state of cobalt as an out-of-plane stripe domain state despite the reduction of magnetocrystalline anisotropy. Detailed micromagnetic simulations, performed by Prof. Dr. Ondrej Hovorka (University of Southampton), supplement the experimental results and corroborate the physical understanding of the temperature dependent behavior. Moreover, they enable a comprehensive identification of the complex energy balance in magnetic films with perpendicular magnetic anisotropy, for which three different magnetic phases occur for sufficiently high anisotropy values, whose coexistence point is *tricritical* in nature.

In the last part, the magnetic field-induced reversal of surface spin polarization for the magnetoelectric antiferromagnet Cr_2O_3 (chromia) is studied via magnetometry in (0001)-oriented thin films of various thicknesses. Hereby, chromia is known to possess a roughness insensitive net equilibrium magnetization at the (0001) surface, called boundary magnetization (BM), which is coupled to the bulk antiferromagnetic order parameter. The experiments evidence the reversal solely by magnetic means in sufficiently thin films. It sets the field-response of chromia films apart from bulk behavior, where switching requires the simultaneous presence of electric and magnetic fields. In the detailed experiments, a giant temperature gradient of the coercive field has been observed, thus, indicating the potential of magnetoelectric antiferromagnets as promising candidates for energy assisted

magnetic recording media. In order to verify whether this symmetry sensitive BM persists in alloys, the impact of diamagnetic dilution has been investigated on chromia thin films alloyed with the isostructural Al_2O_3 (alumina). Single-crystalline $Cr_{2-x}Al_xO_3$ thin films with (0001) surface orientation and varying stoichiometry have been grown in the concentration range between x=0 and x=0.6. For these samples, the corundum crystal structure, the antiferromagnetic ordering, and the boundary magnetization have been found to be preserved. Is has been also found that the critical temperature T_N can be tuned by alloying with Al_2O_3, using the BM as a probe to study the magnetic phase transition. Furthermore, the critical exponent and the absolute BM values have been evaluated for different samples. Both properties corroborate that the observed magnetic signals originate from the BM rather than the bulk of the samples.

Contents

1. Introduction

This chapter presents an introductory overview of the main theoretical concepts employed in this thesis, identifying units, terms and models utilized in subsequent chapters. Section one reviews the basic aspects of Ferromagnetism and introduces the macrospin model utilized to describe part of the samples investigated in this thesis. Section two discusses key features of Antiferromagnetism and the basic concept of boundary magnetization.

1.1. Ferromagnetism

Any kind of material subjected to a magnetic field ***H*** exhibits a magnetic moment ***m***, whose density per unit volume is defined as magnetic polarization or magnetization ***M.*** In most of the cases, ***M*** is simply linearly proportional to the externally applied magnetic field ***H***, and it is defined as:

$$\boldsymbol{M} = \chi \boldsymbol{H} \tag{1.1}$$

with χ being the magnetic susceptibility. However, after the removal of the external magnetic field ***H***, few materials still exhibit a net magnetization that is spontaneous in its nature below a characteristic temperature. This class of distinguished substances is called *Ferromagnets*, and numerous applications ranging from data storage to power generation have made and are making widespread use of them [1]. One distinct property that makes these materials so exclusive lies in the relationship between the magnetization ***M*** and the external magnetic field ***H***, which is non-linear [2], and furthermore exhibits a lag between ***M*** and ***H***, which is typically visualized as a hysteresis loop, depicted in Fig. 1.1, where the component of ***M*** parallel to the direction of the external applied field is plotted as a function of the field strength.

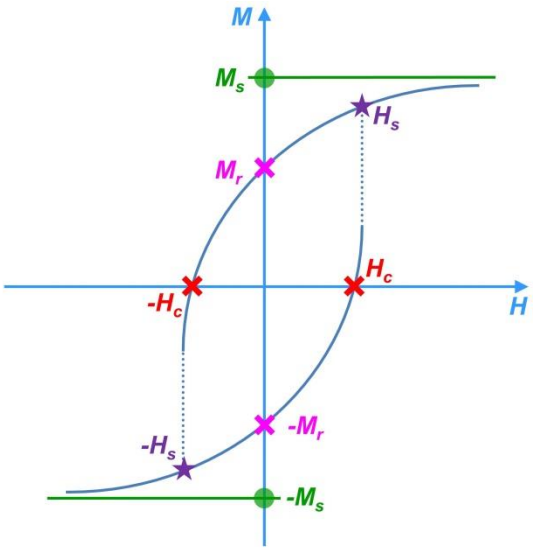

Figure 1.1: Exemplary hysteresis loop for a ferromagnet. Green points and lines indicate the saturation magnetization $\pm M_S$, the pink crosses represent the remanent magnetization values $\pm M_r$, the red crosses indicate the coercive field $\pm H_C$ and the purple stars the switching field $\pm H_S$.

If a sufficiently strong magnetic field is supplied, a nearly maximized material response can be produced, as shown in Fig. 1.1, and a further increase in strength of ***H*** causes only

very small changes in magnetization. This situation corresponds to an almost complete alignment of the magnetization with respect to the external field, exhibiting a magnetization value close to its maximum, which is defined as saturation magnetization M_S. When the field is then reduced down to zero, a magnetization is retained by a ferromagnet, which is called remanence or remanent magnetization M_r (pink crosses in Fig. 1.1), and it needs a certain value of a reversed magnetic field, called coercive field H_C (red crosses in Fig. 1.1), to completely demagnetize the material. Indeed, depending on the value of H_C, ferromagnetic materials are classified as either hard, in which the application of large fields is needed to reduce their magnetization to zero, or soft, which are easy to demagnetize. By further increasing the strength of the applied field, the magnetization might switch, presenting a discontinuous jump in the $M(H)$ dependence (dotted lines in Fig. 1.1), and finally reaches saturation in the opposite direction. The field at which this discontinuous jump happens is called switching field H_S. It is worth mentioning that in some cases H_S may coincide with H_C and other ferromagnetic materials might actually not show a discontinuous switch of the magnetization. By sweeping the field back and forth between high positive and negative values sufficient to saturate the system, the component of the magnetization along the direction of $\boldsymbol{H}$, shown in Fig. 1.1, exhibits a hysteretic behavior as long as the material temperature is lower than its characteristic ordering temperature.

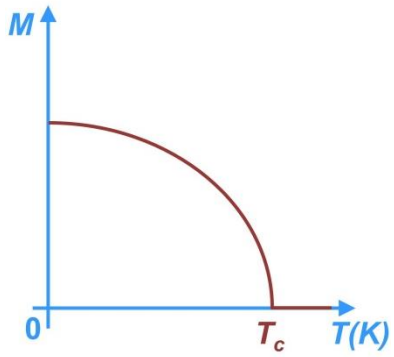

Figure 1.2: Schematic of the second order phase transition that the spontaneous magnetization of a generic ferromagnetic material exhibits when the temperature approaches the corresponding Curie temperature in the absence of internal magnetic field [1].

In fact, above a material specific temperature, ferromagnets no longer exhibit a spontaneous magnetization, and the relationship between $\boldsymbol{M}$ and $\boldsymbol{H}$ becomes linear, as described by Eq. 1.1. Indeed, the material undergoes a *second order phase transition* as a

function of temperature, and the critical temperature, at which the ferromagnetic (FM) phase changes to the paramagnetic (PM) phase, and vice versa, is called Curie temperature (T_C). The corresponding order parameter is the spontaneous magnetization $\boldsymbol{M}$, and a schematic of its temperature dependence in the absence of internal magnetic field is displayed in Fig. 1.2. The FM state corresponds to $M \neq 0$, whereas the PM state to $M = 0$. The origin of the spontaneous magnetization in ferromagnetic material lies in the alignment of neighboring microscopic magnetic moments, which add up to a non-vanishing macroscopic $\boldsymbol{M}$ of the material even in the absence of an externally applied magnetic field. At $T = 0$ K all the magnetic moments are fully aligned and the material exhibits its maximum value of magnetization. As the material is subjected to finite temperatures, the thermal energy activates a misalignment of the magnetic moments. This results in a decrease of the net total magnetization, which varies according to the simple Bloch law at low temperature, while following a power law for temperatures close to T_C [1-5]. The material continues behaving as a ferromagnet as long as the free energy of the ferromagnetic state is lower than that of the paramagnetic one. At T_C, the free energies of both states are equal, and for $T \geq T_C$ the spontaneous magnetization vanishes even if short range and short time ferromagnetic correlations might still persist.

Undoubtedly, the key distinguishing property of a ferromagnet is the appearance of a spontaneous magnetization below the Curie temperature, which is in stark contrast to the vast majority of materials. While it seems reasonable to assume that the origin of ferromagnetic order is the classical direct interaction in between magnetic moments $\boldsymbol{m}$, its characteristic energy scale is far too low to explain conventional *ferromagnetism*, given that it would lead to an ordering (Curie) temperature of only about 1 K, much lower than is found in many materials [3]. In the next section the origin of *ferromagnetism* is introduced and discussed, which is rooted in quantum mechanics.

1.1.1. Origin of the spontaneous magnetization

The existence of the spontaneous magnetization was first described by Pierre Weiss in 1907. He conceived the existence of an inherent or molecular field responsible for the alignment of individual magnetic moments, which originates from all the other magnetic moments present in the material [3]. Almost 20 years later, quantum mechanics

successfully disclosed the nature of this so-called molecular field, which arises from the description of electron spins and associated wave function symmetries. Uncompensated electron spins are key contributors to the local magnetic moments in individual atoms and the origin of long-range ferromagnetic order arises from spin symmetry effects on electron interactions [3]. This specific quantum mechanical interaction is called exchange interaction and derives from the combination of electrostatic Coulomb repulsion between electrons on nearby atoms and the Pauli exclusion principle, since they are fermions having half-integer spin [4]. As a consequence of their identical nature, the total wave function of two electrons, which is a combination of space and spin wave functions, has to be antisymmetric upon exchanging the two fermions. If the two electrons have same spin, the exclusion principle requires an antisymmetric spatial wave function, which prevents the two fermions from getting close to each other. Conversely, if the two spin numbers are opposite, a close approach is possible. This argument can be extended to multi-electron systems and Heisenberg demonstrated that it is fundamentally important for *ferromagnetism* [5]. In fact, by taking into account that the corresponding energy is determined by the total spin, which dictates the symmetry of the spatial wave function part, Heisenberg constructed a new effective spin Hamiltonian, in which the parallel or antiparallel alignment of the spins depend on the sign of the exchange integral. The electron Hamiltonian can be then replaced by an effective spin dependent Hamiltonian, which has the same eigenvalue spectrum. By restricting the summation to nearest-neighbor pairs, because of the small spatial extent of atomic wave functions, the *exchange energy* per unit volume can be written as:

$$E_{ex} = -\frac{1}{V}\sum_{\{i,j\}} J_{ij}\hat{S}_i \cdot \hat{S}_j \tag{1.2}$$

where $J_{i,j}$ is exchange integral, which has units of energy, $\hat{S}_i$ and $\hat{S}_j$ are dimensionless spin operators and the sum with curly brackets is applied to nearest neighbors [3]. In the case of $J_{i,j}$ being positive, E_{ex} will be minimal when the interacting spins are in the same quantum state, meaning that a positive value of the exchange integral is therefore necessary for *ferromagnetism* to occur. Although this original quantum mechanical approach led to many relevant conclusions, including the accurate prediction of ferromagnetism in some materials, it was not able to account for experimentally determined exchange constants in

ferromagnetic transition metals, such as cobalt, iron and nickel, as well as their non-integer values of the magnetic moments expressed in unit of Bohr magnetron. Indeed, in these materials the *d* electrons, which are responsible for *ferromagnetism*, are not localized on the atoms but instead are itinerant, and the available energy states form energy bands. As a consequence, a collective-electron theory was introduced by Stoner, Mott and Slater in 1933 [1,2,3,5], in which exchange interaction acts among band electrons creating a permanent large spin imbalance, which gives rise to a non-vanishing spontaneous total magnetization.

Up to this point the spontaneous magnetization has been considered completely isotropic, but it may have preferential orientations. Also, it has been assumed that all the magnetic moments ***m*** are pointing towards the same directions throughout. Indeed, many ferromagnetic materials, in the absence of an external magnetic field, break into regions with different orientations of the magnetization. The reason lies in additional energy contributions to the *exchange* term, which are introduced and discussed in the next section. It is worth mentioning that the exchange interaction is the strongest energy contribution, which is directly responsible for ferromagnetism. However, the actual appearance of different ferromagnetic states strongly depends on other energy terms, even if they are generally weaker, because the expression in Eq. 1.2 is isotropic and thus, it does not predetermine a specific magnetization orientation or arrangement.

1.1.2. Energy contributions

The energy landscape of a ferromagnetic system is indeed defined by different energy terms. Each of them might favor a different magnetic configuration, and the resulting ground state is the result of the minimization of the total free energy expression. The most important energy is the *exchange energy*, which is the origin of *ferromagnetism* and which leads to a preferred alignment of neighboring magnetic moments. At the same time, those magnetic moments carry a classical dipole moment, and the interaction due to the magnetic field created by these dipole moments themselves gives rise to the *magnetostatic energy* [1-6]. The expression of this energy term per unit volume for a system of *N* magnetic moments is:

$$E_m = -\frac{\mu_0 M_s}{2N} \sum_i^N \hat{\boldsymbol{m}}_i \cdot \boldsymbol{H}_{(i)} \tag{1.3}$$

where $\boldsymbol{H}_{(i)}$ is the field vector or magnetostatic vector generated at the position of $\hat{\boldsymbol{m}}_i$, which represents the magnetic moment's unit vector, created by all other moments $\boldsymbol{m}_j$. It is given by:

$$\boldsymbol{H}_{(i)} = -M_s \sum_j^N \overline{\overline{N}}_{ij} \cdot \hat{\boldsymbol{m}}_j \tag{1.4}$$

with $\overline{\overline{N}}_{ij}$ being the demagnetizing tensor. Although the calculation of $\overline{\overline{N}}_{ij}$ is generally not simple, in the presence of homogenous magnetization distribution and ellipsoidal sample shapes, the demagnetizing or stray field is uniform and the tensor can be calculated exactly, resulting in a symmetric matrix with a unitary trace [7,14]. Indeed, other simple shapes, such as thin films, spheres or long needles, can be approximated to ellipsoids as far as the magnetization state is uniform [7]. In such cases, the magnetostatic energy can take the form of an effective anisotropy, known as *shape anisotropy*, which for instance in thin film systems favors in-plane orientation of the magnetization [7].

The expression for the exchange energy provided in Eq. 1.2 is invariant under global spin rotation. However, in crystalline solids, depending on the crystal structure of the material, preferential orientations of the magnetization corresponding to certain crystallographic axes are energetically favored. For instance in Cobalt, which adopts the hexagonal closed packed (*hcp*) structure, a small magnetic field is sufficient to magnetize a demagnetized sample to saturation if applied parallel to the [0001] direction, known as easy-axis (EA), whereas stronger fields are needed to magnetize the material if applied along a perpendicular direction, known as hard axis (HA). This anisotropy of the total energy is called *magnetocrystalline anisotropy* [1-3,5]. Its origin lies in the combination of spin-orbit coupling and the crystal field. The spin-orbit interaction can be interpreted as the coupling between the spin and the "magnetic field" created by electron orbital motion around the nucleus. At the same time, this orbital motion in solids is directly coupled to the crystal lattice. As a consequence, the energy contribution corresponding to the spin-orbit coupling will reflect the symmetry of the crystal lattice and causes the fact that orientations of the magnetization along certain crystallographic directions are energetically preferred.

Depending on the crystal structure, the magneto-crystalline anisotropy can be uniaxial, biaxial, cubic, etc. For certain materials, this is an important energy term that controls the preferential direction of the magnetization, as will be presented and discussed in Chapters 3 and 4. In other cases, it can be very weak, so that it can be considered effectively absent. The magnetocrystalline anisotropy energy term can be formulated by means of a series expansion in orthonormal spherical harmonics with anisotropy coefficients. However, it is more commonly given as a power series expansion in terms of polar and azimuthal angles of the magnetization direction. The conventional energy density expression for the specific case of uniaxial symmetry, in which all the odd terms vanish because of time-inversion symmetry, is therefore:

$$E_K = \frac{1}{N}\sum_{i}^{N}(K_0 + K_1 \sin^2 \alpha_i + K_2 \sin^4 \alpha_i + higher\ order\ terms) \tag{1.5}$$

where K_0, K_1 and K_2 are the zeroth, first and second order anisotropy constants, whose dimensions are given in energy per unit volume, and α_i are the angles in between the magnetization orientations and the uniaxial symmetry axis. Generally, the magnitude of higher order terms decrease rapidly with their order and the series expansion can be stopped at the second one. Furthermore, K_0 does not contribute to the minimization of the free energy, given that it does not vary with the direction of magnetization. A positive value of K_1 and (K_1+K_2) corresponds to an easy-axis anisotropy, whereas a negative value of both to an easy plane anisotropy.

The interaction energy between the magnetization vector and the external magnetic field is called *Zeeman energy* and represents the last energy contribution to the magnetic free energy that is considered here (given the type of physical system and materials that are relevant in this thesis, any other contribution has been neglected). The expression of the Zeeman energy density term is given as:

$$E_Z = -\frac{\mu_0 M_s}{N}\sum_{i}^{N} \widehat{\boldsymbol{m}}_i \cdot \boldsymbol{H} \tag{1.6}$$

where $\boldsymbol{H}$ is the external applied field. The final expression of the total free energy of a ferromagnetic body type studied in this thesis is given by:

$$E = E_{ex} + E_K + E_m + E_Z \tag{1.7}$$

Most of the time the different energy contributions are not minimized by the same magnetization distribution: although a uniform magnetic state would certainly minimize the *exchange* and *anisotropy* contributions to the total energy, such a configuration will significantly increase the *magnetostatic energy*. As a consequence, the formation of non-uniform magnetic states and especially the creation of separated regions with different orientations of the magnetization, known as domain structure, are an efficient way for a ferromagnetic material to minimize its total energy.

1.1.3. Magnetic domains

The magnetostatic energy in large-scale systems strongly favors the formation of magnetization configurations that lead to a sample averaged magnetization close to zero. In the presence of magnetocrystalline anisotropy, an effective means for a ferromagnetic material to minimize its energy is to break up into different regions with different magnetization orientations, inside which the magnetization is uniform. These are called domains, and they are separated by regions in which the magnetic moments rotate coherently, known as domain walls [8]. The *magnetostatic energy* is the principal driving force for the formation of the magnetic domains, while their shape and size are strongly influenced by the *exchange energy* and *magnetocrystalline anisotropy* [8]. Historically, the concept of magnetic domains was postulated in 1907 by Weiss while almost thirty years later Bloch introduced the concept of domain walls at the boundary between two regions of different magnetic moment orientations. In 1935 Landau and Lifshitz provided a first quantitative energy description of non-uniform magnetic regions in ferromagnetic crystals, which is the starting point of modern domain theory [9]. Fig. 1.3(a) illustrates a magnetic system, in which the *anisotropy* and *exchange energies* are minimized, resulting in a uniform magnetization lying in the direction of the EA. It is also apparent from the schematic that the magnetization causes large stray fields. In order to reduce the corresponding magnetostatic energy, the system can break into regions with antiparallel magnetic configuration, Fig. 1.3(b). On the other hand, the magnetic moments at the boundary between the two domains are not able anymore to align parallel, causing an

increase of the *exchange* and *anisotropy energy* terms due to the formation of domain walls[1].

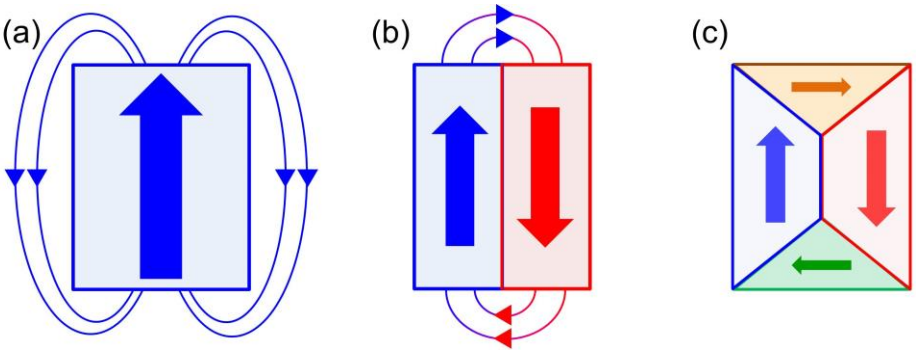

Figure 1.3: Schematic illustration of domain creation: (a) shows a uniform magnetic state with the corresponding stray field lines, (b) displays two magnetic domains with the reduced stray field and (c) closure domains with the absence of relevant stray field.

Finally, the configuration displayed in Fig. 1.3(c) allows the almost complete avoidance of stray fields through the formation of closure domains. However, the *exchange* and *anisotropy* energies increase even further, and this configuration is possible only in the presence of weak uniaxial anisotropy or in materials with four-fold anisotropy. Overall, domain formations can be expected until the energy required to form a domain wall is greater than the reduction in *magnetostatic energy* in the entire domain pattern [8]. Thus, the competition between *exchange*, *anisotropy* and *magnetostatic* energies leads to the formation of domains, as will be presented and thoroughly discussed in Chapter 4. At the same time, their competition leads to energy landscapes that are complex due to the existence of many meta-stable possible domain configurations. Consequently, in real samples, the formation and evolution of multidomain states is rather complex as well, due to the large number of possible configurations that have very similar energies. Furthermore, the generation of a new domain typically requires the system to overcome an activation barrier.

However, once an external magnetic field is applied, the *Zeeman energy*, which can be easily adjusted by controlling the field magnitude, might control the formation and evolution of domain configurations. In the next section the role of the external magnetic field is presented and analyzed, especially in relation to processes that lead to an inversion

[1] In the presence of atomically sharp domain walls, the anisotropy energy would still be minimized, whereas the exchange energy would be yet higher.

of the magnetization vector with respect to its initial direction, called magnetization reversal.

1.1.4. Magnetization reversal processes

Field induced magnetization reversal together with its eventual hysteretic properties is the most common approach to identify the magnetic characteristics of any sample. However, despite the straightforward basic concept of a complete inversion of the magnetization, the problem is more complicated than it seems. In fact, it is almost impossible to predict the reversal path of a generic ferromagnetic material in a quantitative manner. Overall, the shape of the $M(H)$ hysteresis loop and the reversal processes of M are the result of the complex energy landscape, described in the previous section. Consequently, the magnetization reversal can occur by different mechanisms and the hysteresis loop shape is strongly affected by this. As mentioned in the previous section, Pierre Weiss introduced the concept of the coexistence of regions with different orientation of the magnetization in a ferromagnetic material. Their existence is triggered mainly by the *magnetostatic energy* that favors spatially non-uniform magnetization configuration, for which the stray field is minimized. This, in turn means that typically non-uniform magnetization reversal occurs. In fact, when an external magnetic field is applied, the regions in which the magnetization is pointing parallel to the direction of $\boldsymbol{H}$ are energetically favored and they grow in size. At the same time, magnetization rotation can occur within each of the domains to minimize the *Zeeman energy* contribution of every domain. Consequently, for a sufficient strength of the magnetic field, a uniform magnetic state can be achieved, even in the presence of magnetostatic energy contributions. If the field is now reversed, domains of opposite magnetization will appear and progressively, by increasing their sizes and by magnetization rotation, the magnetic field is again sufficient to induce a single domain state but with reversed magnetization. The simpler case of a coherent reversal process is possible, but only in systems, in which the *magnetostatic energy* is weak and thus insufficient to support domain formation, and instead the *exchange* and *anisotropy energy* are the only relevant contributions, in addition to a varying *Zeeman energy* term driving the reversal process. Designed thin film systems with in-plane magnetocrystalline easy axes and thicknesses in the nanometer range, fulfill this condition (Chapter 3). As a

consequence, single domain magnetic configurations are more favorable and the corresponding magnetic behavior can be very well described by means of a simple macrospin model without the requirement of any further non-uniform magnetization state refinement [10-14].

1.1.5. Macrospin model

The macrospin model considers a ferromagnetic material as represented by a single magnetization vector, and thus it represents a single domain state. This has been originally devised for magnetic nano-particles, in which spatially non uniform states can be excluded in good approximation. Therefore, the exchange energy is a constant term, given that it does not depend on the absolute orientation of magnetization, and the magnetostatic energy becomes an effective anisotropy contribution. The simplest case to consider is a uniaxial in plane magnetic anisotropy system, which is also the most appropriate model to describe the samples shown in Chapter 3. Nevertheless, in this situation in-plane demagnetization fields still exist but they are extremely small and consequently they can be neglected.

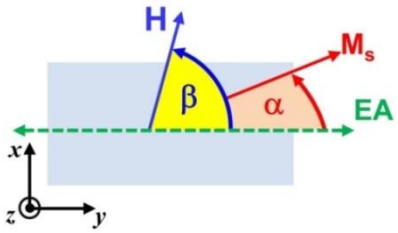

Figure 1.4: Schematic of the macrospin model described by Eq. (1.8).

Given that the *exchange energy* term does not vary with the magnetization orientation, only *anisotropy* and *Zeeman energies* play a role in the energy minimization [10-14]. With the additional assumptions of only the first order (K_1) anisotropy energy term and in-plane orientation of a uniform magnetic field, the energy density is given by:

$$E = -\mu_0 M_S H \cos(\beta - \alpha) + K_1 \sin^2 \alpha \qquad (1.8)$$

with α being the angle between $\boldsymbol{M}_S$ and the anisotropy easy axis and β the angle defined by the external magnetic field and the EA (Fig. 1.4). The first term in the equation describes the *Zeeman energy*. Moreover, Eq. (1.8) assumes that the magnetization vector is confined to the plane *x-y* defined by $\boldsymbol{H}$ and the EA, so that the out-of-plane component can be ignored. This condition is matched by the sample structures investigated in Chapter 3 by

assuming that the magnetic field is in plane. For a given field direction, the equilibrium position of the magnetization can be obtained by minimizing the energy with respect to α, such that:

$$\frac{dE}{d\alpha} = 2K_1 \sin\alpha\cos\alpha - \mu_0 H M_S \sin(\beta - \alpha) = 0 \tag{1.9}$$

and the second derivative $d^2E/d\alpha^2$ is positive. In the absence of the external magnetic field, the magnetization lies along the EA. If the magnetic field is applied perpendicular to the easy axis, i.e. $\beta = 90°$ (Fig. 1.5(a)), by increasing its strength the magnetization continuously rotates from the EA towards the HA. The field strength needed to saturate the magnetization of a uniaxial crystal along the hard direction is:

$$H_{sat} = \frac{2K_1}{\mu_0 M_S} \tag{1.10}$$

which is defined as the anisotropy field H_{K_1}. In this case the magnetization does not undergo any switching during the reversal process and correspondingly, there is no hysteretic behavior as shown in Fig. 1.5(b), which corresponds to a completely reversible change in the magnetization.

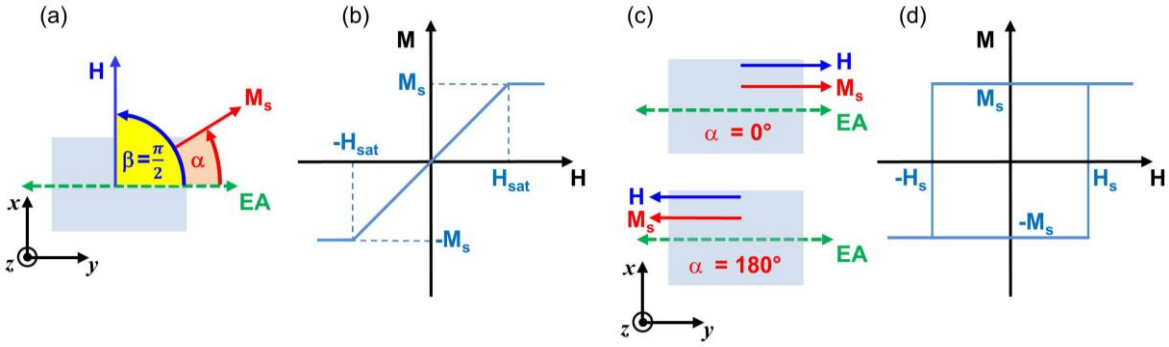

Figure 1.5: (a) schematic for the *β*=90° case. (b) *M(H)* curve obtained for the situation depicted in (a). (c) displays the configuration in which *H* is applied parallel to EA and (d) the corresponding magnetization curve. In both *M(H)* is considered the component of M parallel to *H*.

In the case of the magnetic field applied parallel to the EA (β = 0°) the magnetization lies always along the easy direction, namely at α = 0° (Fig. 1.5(c) top schematic) or α = 180° (Fig. 1.5(c) bottom schematic). Upon the removal of the external applied field, i.e. H = 0, and in the absence of thermal excitation or tunneling processes, the magnetization stays in the same direction in which it was oriented previously. When an

opposite external magnetic field is subsequently applied, the magnetization is unaffected until at a certain field strength $\pm H_S$ it switches direction abruptly, as shown in Fig. 1.5(d). This is due to the fact that the original energy minimum at α = 0° (180°) changes to a maximum when $H = \pm H_S$, thus becoming unstable.

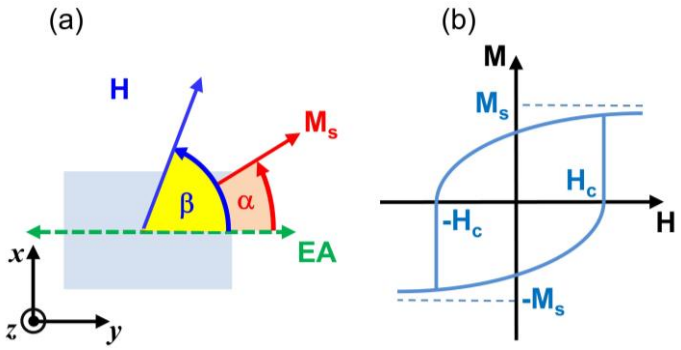

Figure 1.6: (a) schematic representing the situation with *H* applied at an angle *β* with respect to the easy axis. (b) *M(H)* curve corresponding to the situation depicted in (a).

If one considers now that the applied field is swept cyclically from negative to positive values and vice versa, the magnetization will switch repeatedly between α = 0° to α = 180° any time that the magnetic field is antiparallel with respect to the magnetization and its strength equals $\pm H_S$. This behavior is represented by square hysteresis loops, where the magnetization takes values of $\pm M_S$ (Fig. 1.5(d)). If ***H*** is applied at some arbitrary angle β with respect to the anisotropy field, then the behavior is partly reversible and partly irreversible as shown in Fig. 1.6(b). A discontinuity occurs in the projection of the magnetization along H at a switching field H_S. The corresponding rotation is represented by a continuous reduction of the absolute magnetization value in the hysteresis loop, which results in a decrease of the projection of the magnetization along the applied field direction (Fig. 1.6 (b)). Also in this geometry, at a certain field strength of opposite sign with respect to the original magnetization orientation, the system suddenly switches its direction and thus exhibits a discontinuous jump in the $M(H)$ curve. For higher reverse fields, coherent rotation proceeds towards the applied field direction. This rotation is also visible in the hysteresis loop, where the absolute value of the magnetization increases towards $\pm M_S$ after the magnetization switch (Fig. 1.6 (b)) with M_S being an asymptote.

1.2. Antiferromagnetism

Antiferromagnetic (AFM) materials possess a small positive susceptibility χ at any temperature, and at a first glance they may therefore be considered as anomalous paramagnets (PM) [5]. However, the way in which the AFM susceptibility varies with temperature, shown in Fig. 1.7 (a), is really exclusive: as the temperature decreases, χ increases similar to a paramagnet but at a certain temperature it goes through a maximum and then decreases again. Furthermore, unlike ferromagnets in which χ diverges at a critical temperature, in the AFM material class the susceptibility is a continuous function with a weak cusp at a distinct temperature. This point is singular and it represents the critical temperature of a PM-AFM *second order phase transition*, which is called Néel temperature T_N [15]. In addition, neutron scattering measurements [16] revealed that the underlying magnetic structure is indeed entirely different with respect to a ferromagnetically ordered material, with antiparallel alignment of the neighboring magnetic moments. Above the critical temperature the system is in its paramagnetic state, whereas at T_N the antiparallel alignment of the magnetic moments is established with a non-vanishing expectation value of the order parameter for $T < T_N$. The corresponding order parameter of the PM-AFM *second order phase transition* is the so called *staggered magnetization* and its conjugate field is the *staggered magnetic field* which alternates positive and negative values following the specific AFM order. As in ferromagnets, the corresponding *staggered susceptibility* diverges at the critical temperature.

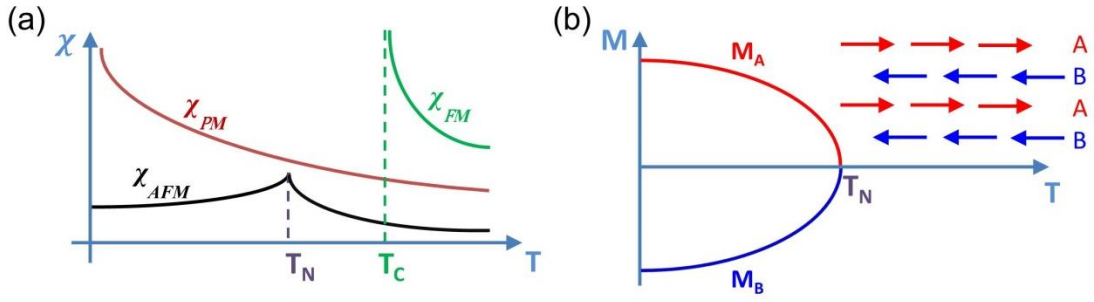

Figure 1.7: (a) schematic representing the temperature dependence of the susceptibility χ for an AFM (black line), PM (dark red line) and above the Curie temperature for a FM (green line). The two dashed lines refer to the critical temperature T_N (purple) and T_C (green). (b) Schematic of the second order phase transition that the spontaneous magnetization of each sublattice A and B undergo when the temperature approaches the Néel temperature.

It can be also noted that T_N plays the same role as the Curie temperature T_C. Both divide the temperature scale into two regions where a magnetically ordered phase is present below the critical temperature and a disordered paramagnetic region above. The orientation along which the sublattice magnetizations lie is determined by the magnetic anisotropy. Fig. 1.7(b) shows the second order phase transition for each sublattice in the absence of external magnetic field as red and blue lines as if they were acting separately.

The theory of antiferromagnetism was developed by Néel, in which he applied the Weiss molecular field theory. In order to explain the antiparallel alignement between the magnetic moment, Néel proposed a molecular-like field, which operates in a way that it is favorable for nearest neighbors ***m*** to lie antiparallel to one another [5]. Let's consider the simplest case possible of a bipartite lattice, depicted in Fig. 1.7(b), in which the lattice of magnetic moments can be decomposed into two identical sublattices, named *A* and *B*, where all the nearest neighbors are members of the other sublattice. It is also assumed that the only interactions are in between nearest neighbors (*AB*) and possible interactions in between second-nearest neighbors (*AA* and *BB*) are ignored [5]. Two molecular fields then arise: H_m^A, which acts on the magnetic dipoles at the sublattice *A* and it is proportional and opposite in direction to the magnetization M_B and conversely H_m^B , which is proportional to M_A but opposite to the magnetization of the *A* lattice:

$$H_m^A = -\lambda M_B \tag{1.11}$$

$$H_m^B = -\lambda M_A \tag{1.12}$$

The molecular field coefficient is expressed by λ. According to Section 1.1.1, it was shown that the origin of the Weiss molecular field is the quantum mechanical exchange integral $J_{i,j}$. A positive exchange integral lowers the energy of parallel spins whereas a negative $J_{i,j}$ favors the antiparallel (AFM) configuration as a ground state.

In common magnetic metals only direct *exchange interaction* contributes to the selection of the magnetic order. Instead, in magnetic oxides, different mechanisms are responsible for the occurrence of antiferromagnetic ordering such as *superexchange interaction*, which is mediated by the oxygen atoms, or *double exchange interaction*, in the presence of mixed valence oxide compounds. Therefore, the conceptual simplicity of bipartite lattices does not lead to a self-evident magnetic ordering. In fact, the

combinations of different exchange constants and different lattice types can lead to a wide variety of possible AFM order states [15]. Moreover, the fact that AFMs do not exhibit a net volume average moment and the consequent absence of the magnetostatic energy term would suggest that the single domain state is the thermodynamically stable domain configuration. However, local nucleations of the AFM order at T_N and their growth below the critical temperature lead to the formation of domains even if their existence may be transient. Imperfections such as grain structure, defects of the crystal lattice, structural boundaries or twinning may all act as pinning centers for domain walls, and multidomain states are often observed especially when the system undergoes the PM-AFM phase transition from above T_N [17]. In this case, unlike a FM, the external magnetic field cannot be used to drive the AFM system in a single domain state, due to the fact there is no energetic advantage for the moment to align according to the field because any energy minimization on one sublattice will be counterbalanced by the energy cost of the other sublattice.

1.2.1. Antiferromagnet chromia

Magnetic susceptibility and specific heat measurements indicated that chromium sesquioxide Cr_2O_3 (chromia) is an antiferromagnetic material. Neutron diffraction measurements showed that the AFM arrangement of the moment developed by the chromium ions occurs below the critical temperature $T_N = 307\,\mathrm{K}$ in the bulk state [18,19]. This material, similar to Fe_2O_3 or Al_2O_3, adopts the corundum crystal structure with trigonal space group R$\bar{3}$c consisting of hexagonal close-packed layers of O^{2-} atoms, Fig. 1.9(a), with two-thirds of the corresponding octahedral sites being occupied by Cr^{3+} atoms Fig. 1.9(b) [20]. The $\bar{3}$ denotes the threefold symmetry, while *c* a glide plane parallel to the *c*-axis. The oxygen anions follow an *hcp* stacking, i.e. *ababab*, while the chromium cations exhibit an *abcabc* stacking sequence as found in *fcc* lattices [21]. A schematic of the resulting crystal structure is shown in Fig. 1.9(c). The magnetism is governed by the chromium ions and below the critical temperature the system exhibits antiferromagnetic ordering ↑↓↑↓ along the rhombohedral [111] or hexagonal [0001] *c*-axis direction[2], which is also the easy magnetization axis (magnetic point group $\bar{3}$'m'), as shown in Fig. 1.9(d). As

[2] In the rest of the thesis only the hexagonal closed packed notation is utilized.

was pointed out by Shi [22], the particular antiferromagnetic arrangement is due exclusively to direct exchange coupling, whereas the super-exchange is ineffective because the Cr-O-Cr angles are close to 90°. Interesting, the ordering of the main "chain" along the *c*-direction, shown in Fig. 1.8(d), does not preserve the spatial inversion symmetry, with the dashed black lines indicating the inversion plane of the structure.

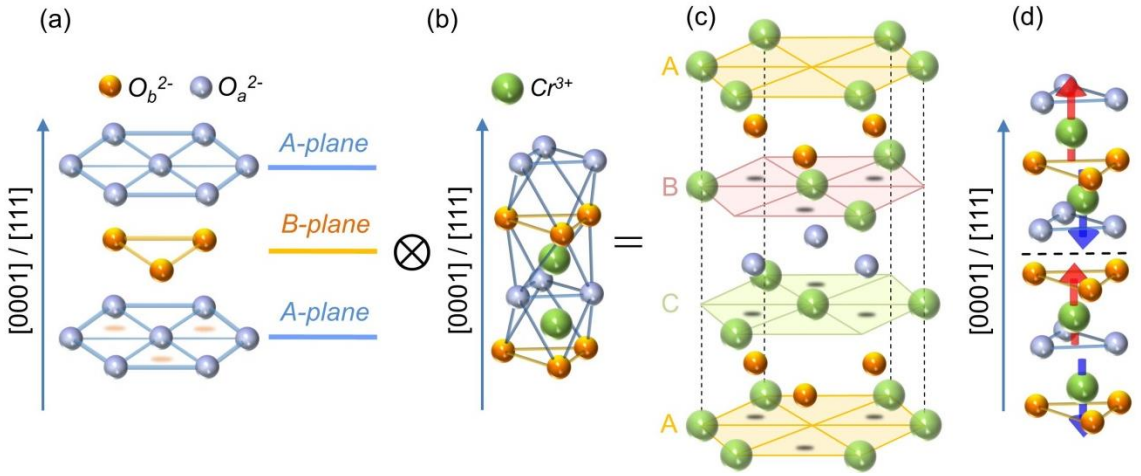

Figure 1.9: (a) hcp arrangement adopted by the oxygen atoms; (b) Cr^{3+} cations in the octahedral holes; (c) corundum crystal structure of Cr_2O_3; (d) schematic of the antiferromagnetic order along the easy magnetization axis.

Indeed, in this particular system, time-reversal and spatial-inversion symmetries are both broken and only their combined operation leaves the spin structure invariant. Thus, as predicted by Dzyaloshinskii [23], the necessary conditions for the existence of the linear magnetoelectric (ME) effect are met in Cr_2O_3. Consequently, in this class of material, an electric (magnetic) polarization can be induced by the application of an external magnetic (electric) field. [23-26]. Recently Belashchenko identified that, in the special case of ME-AFM material, the boundary develops a finite equilibrium magnetization called boundary magnetization (BM), which acquires the same magnetization component as the bulk with an electric field applied perpendicular to the surface [27]. As a result, the BM is a symmetry enabled equilibrium property and therefore robust against the potential presence of surface roughness [28]. This is in sharp contrast to surface magnetic states of conventional antiferromagnets where step-terraces at the surface create alternating local magnetizations and, hence, a vanishing net surface polarization over large areas [29,30]. The magnetoelectric antiferromagnet chromia thus exhibits an equilibrium net magnetization at (0001) surfaces, which is fully coupled to the bulk antiferromagnetic

order parameter. They can be reversed together by the combined application of *E* and *H* fields in bulk materials below the Néel temperature [28]. It is worth mentioning that the BM in ME-AFM is a well-defined concept that has triggered a lot of work on direct observations and applications [31,32]. Experimental microscopic evidence has been provided for Cr_2O_3 and Fe_2TeO_6 using X-ray magnetic circular dichroism–photoemission electron microscopy (XMCD–PEEM), spin-polarized inverse photoemission and spin-polarized photoemission [28,29,33]. Therefore, in Chapter 5, the existence of boundary magnetization has been considered as established and correspondingly, this concept has been utilized for the interpretation of experimental data, which are all found to be compatible with it.

2. Experimental methods

This chapter provides an overview of the different experimental techniques that have been used for this thesis. Section 2.1 describes the sputter deposition technique, which has been exploited to fabricate high quality thin magnetic film samples. Section 2.2 illustrates the different structural characterization methods utilized, while Section 2.3 briefly introduces microscopy techniques. Finally, Section 2.4 focuses on the methods that have been used to characterize the magnetic properties.

2.1. Samples Fabrication

Thin film deposition is a technique aimed to create a very thin film of material, with thicknesses ranging from micrometer down to below one nanometer, onto a surface to be coated, or onto previously deposited coatings. This technique is being employed in a widespread range of applications, and it can be regarded as an essential aspect of microelectronics, optics, magnetic storage media, hard and corrosion resistant coatings, and many more [34]. Different techniques can be utilized to deposit thin layers of materials, and usually they can be divided into two broad categories depending on the deposition mechanism: chemical vapor deposition (CVD) and physical vapor deposition (PVD). The former utilizes volatile precursors that produce a chemical reaction near or at the surface of a substrate to form a coating; the latter refers to a wide range of techniques where a material is released from a source and deposited onto a substrate [35]. Sputtering deposition belongs to the PVD group [36], and it has been the method selected and used in this work. It is a robust and efficient method that allows for the preparation of thin film with high reproducibility and with high quality, which is widely used in nanotechnology and semiconductor fabrication. In this technique, the process starts with the ejection of surface atoms from a target by simple momentum transfer due to bombarding ions and it completes with their subsequent deposition onto the surface of a substrate in order to form a thin coating. Sputtering is clearly a physical etching process and in fact, it can also be used as such for surface target or substrate cleaning before any actual deposition in order to remove contaminations or surface oxidation layers. The actual deposition process depends on several parameters such as the selected materials and the substrate, the substrate temperature, the sputtering geometry and the kinetic aspects of the growth. Except under very special conditions, the deposition of thin films usually leads to polycrystalline arrangements consisting of many crystallites or grains with different relative crystallographic orientation. They can be randomly oriented, due to statistical randomness or they can show preferential orientations, i.e. a crystallographic texture. A crystallographic texture can appear for instance as a consequence of the different surface energies at different crystal orientations. An example are *face-centered-cubic* (*fcc*) metals, which frequently exhibit a predominance of (111) surface planes on amorphous substrates. On the other hand, thin films with specific crystallographic order can be fabricated by

epitaxial growth, meaning that the crystallographic order of the deposited layer is induced and controlled by that of the substrate. In particular, in the case in which the epitaxial film is deposited onto a substrate or layer made from the same material, the process is called *homoepitaxy*, whereas *heteroepitaxy* describes the case in which the materials involved are different from each other [34,35]. In general, a single crystal substrate is mandatory in order to produce a highly oriented crystalline epitaxial layer and, moreover, both substrate and deposited layer must be crystallographically compatible with each other by exhibiting a good lattice match and similar crystal symmetries. This requirement can be mitigated by the introduction of intermediate layers of other materials in order to adapt the substrate crystallographic alignment towards the desired one. Unfortunately, the compliance with these requirements does not prevent failures. For instance, although a desired particular orientation of a specific material has a perfect lattice match condition with the substrate or with an intermediate layer, interdiffusion or chemical reactions may occur at the film/substrate interface, which might interrupt the epitaxial growth. Furthermore, any possible contamination at the substrate or layer surfaces and interfaces may cause the deterioration of the crystalline quality or suppress epitaxial growth altogether. In order to minimize any possible source of process poisoning, ultra-high vacuum (UHV) conditions prior to any deposition are needed. Once the epitaxial growth is successfully achieved, it assures the fabrication of thin films with designed crystallographic orientations, which can strongly influence and control many physical properties. In this thesis, metal, oxide and alloy thin films of varying thickness, crystalline structure and composition have been grown by means of sputter deposition and the next section is dedicated to explain the main aspect of the selected technique.

2.1.1. Sputter deposition

In a basic sputtering process, a target material is bombarded by energetic ions generated by the glow discharge plasma situated in close vicinity to the target [36]. To ignite the plasma, a suitable pressure of an appropriate gas is introduced into the ultra-high vacuum chamber. Usually, the most common gas used is the inert gas argon (Ar) in order to avoid unwanted chemical reactions with the target materials or substrate. A voltage is then applied between the chamber wall (anode) and the sputtering source target (cathode). The ubiquitous

background radiation is already sufficient to produce a small fraction of ions and free electrons. They are both accelerated towards the cathode and anode, respectively, and consequently the electrons can generate new ions and free electrons via collisions with the Ar atoms. In addition, secondary electrons are generated at the cathode surface. All the "new" free electrons are then accelerated by the electric field, and generate additional Ar^+ ions and more free electrons, thus starting an "avalanche" ionizations process. If the applied power is sufficiently high, a stable plasma is created and then maintains itself upon reaching a balance between charge losses and charge generation via the supplied energy. Under these plasma conditions, the so-created Ar^+ ions are accelerated towards the negatively charged target and they strike it with enough kinetic energy to tear off atoms from it. The extracted atoms then move away from the cathode towards an appropriately positioned substrate. A schematic of the deposition process is depicted in in Fig. 2.1(a), where the green spheres represent the material leaving the target source.

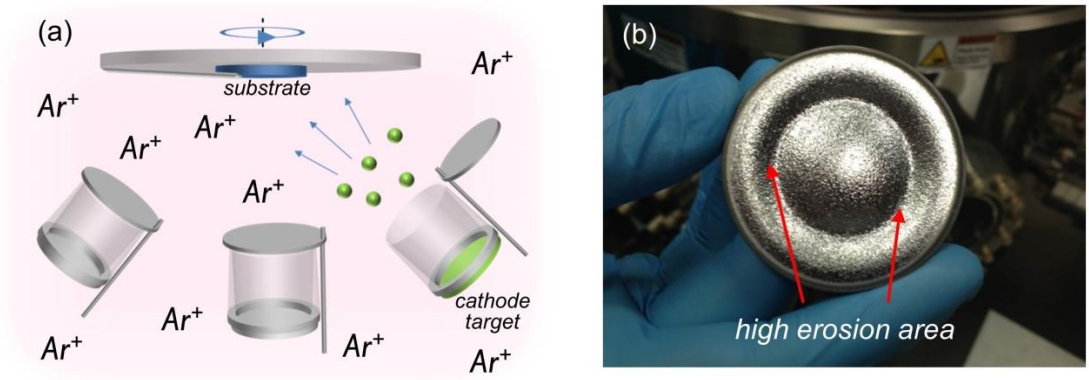

Figure 2.1: (a) schematic of the sputtering deposition process; (b) photograph of a Cr-sputter target, in which magnetron erosion produces a circular race-track.

In this type of sputtering process, the Ar^+ ions flow responsible for the erosion of the target is continuously generated by the plasma itself, with no need of any external ion supplier. The rate of the material leaving the target depends primarily on the number of bombarding ions. It is therefore desirable to increase the plasma density close to target material, because otherwise low deposition rates due to limited ionization efficiencies of the plasma would result as a severe limitation of the technique. This possible downside has led to the development of the magnetron sputtering technique [37]. By placing an array of permanent magnets behind the target, in a way that one pole is positioned at the center of the sputtering source and the second pole in a ring around its perimeter, a static magnetic field

is generated over the cathode. The free electrons are now obligated to move in a direction perpendicular to both H, which is parallel to the target surface, and E, which is normal to the surface. This leads to much longer paths for the electrons, which in turn enhances the probability of collisions substantially, leading to much higher self-regeneration yields for the plasma. As a consequence, the ion flux increases and consequently the achieved deposition rates are higher. Fig. 2.1(b) shows a chromium target with the typical impression of the higher sputter erosion, which forms an annular ring. The magnetic field configuration of magnetrons is not unique and it can be divided in two main different categories: balanced, in which the magnetic flux created by the outer magnets is compensated by the central pole; and unbalanced, where the flux of the central magnet is not fully compensated by the outside ring [38,39]. The sputtering process described is usually generated by a direct current (DC). Unfortunately, in the case of non-conductive target materials, a DC also generates a charge accumulation at the cathode surface impeding the plasma discharge. In order to avoid this, the removal of the positive charging is accomplished by supplying an alternating radio frequency (RF) power, instead of a DC power [35,36]. By the application of a periodic electric field, during the positive half cycle the electrons neutralize the positive charging at the target surface and during the consecutive negative half cycle the Ar^+ ions bombard the cathode causing sputtering. Consequently the sputtering process occurs only during half of the cycle and RF deposition rates are generally substantially lower than in DC sputtering. The deposition system utilized in this thesis is a commercial ATC series UHV sputtering system from AJA International, Inc. Company. It is composed of two vacuum chambers, displayed in Fig. 2.2(a), both equipped with turbo-molecular pumps in order to reach a pressure better than 1.33×10^{-6} Pa. The smaller chamber is a load lock chamber, i.e. a small compartment used to insert clean substrates into the main chamber by means of a magnetic arm without breaking the vacuum condition of the main chamber itself. This has two major advantages: any deposition can begin within less than two minutes after substrate introduction and, more important, the presence of residual water vapor, which breaks down in the plasma and results in unwanted oxygen and hydrogen incorporation into the film chemistry, is significantly reduced. The main chamber is thus opened only in order to replace targets or for system maintenance. It is important to mention that after these occasional openings, all

targets were cleaned by several presputtering cycles until both voltage and current stay constant at a fixed power. The sputtering process is carried out in the main chamber, which is equipped with seven different magnetron sputter guns, as shown in Fig. 2.2 (b). The different target materials are placed inside the latter. Furthermore, each individual magnetron configuration can be adjusted to compensate for the presence of room temperature magnetic materials as targets, which would otherwise lead to shunting of the magnetron magnetic field. The sputter deposition system is also equipped with three RF and four DC power supplies, and given that all the guns are compatible with both, it is possible to deposit simultaneously seven different materials, metals and insulators, mainly for alloying purpose. Alternately, by taking advantage of shutters in front of each sputter gun that can be opened or closed without breaking the vacuum (Fig. 2.2(b)), all materials can be deposited in sequence creating multilayers.

Figure 2.2: (a) UHV sputter deposition system at CIC nanoGUNE; (b) inside view of the main chamber showing the seven different sputter guns with their shutters.

In the utilized system, all sputter guns have a mechanical degree of freedom, and can be tilted towards or away from the sample holder, Fig. 2.2(b), on which the substrate is located during deposition. This permits, prior to any deposition, the alignment of one or multiple guns pointing to the substrate, which allows for the minimization of the transition time in between subsequent layer depositions. Also, this geometry allows one to easily grow alloys of different materials in any ratio with precise control. In addition, in order to avoid lateral thickness or composition variations, the sample holder is always rotating during the deposition. A thickness uniformity of better than 1 nm over a 10 cm strip for 30

nm thick Cr, Ru and Co films has been verified, as shown in Fig 2.3 (b),(c) and (d) respectively.

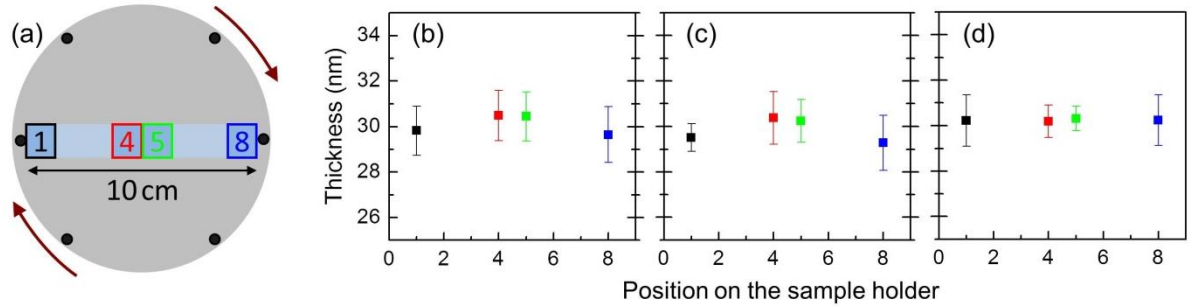

Figure 2.3: (a) schematic of the sample holder together with the 10 cm long sample strip. The thickness dependence on the position on the holder is displayed in the case of cobalt (b), ruthenium (c) and chromium (d).

In all likelihood, the uniformity is actually far better than the precision with which the thickness can be measured for these metallic films by means of X-ray reflectivity (XRR), a technique that will be presented in Section 2.2.1. All the samples fabricated in this thesis have been grown using the same argon gas pressure of 4×10^{-1} Pa, which was found suitable to ensure stable and sufficiently large deposition rates. Hereby, the sputtering pressure is controlled via a gate valve that separates the main chamber from its turbo molecular pump. Moreover, the sputter system is equipped with three lamps placed on the rear part of the substrate holder which allow heating the substrate up to T = 1123 K prior, during and after the sputtering process. The deposition rate of each individual target material has been thoroughly characterized by means of two consecutive steps. First, at a fixed gun power, depositions have been performed for different deposition times. Consequently, the thickness of each calibration sample has been measured via XRR. Figure 2.4(a) shows the measured thickness as a function of deposition time for Co and Cr, blue squares and dark yellow dots respectively, using a sputtering power of P = 100 W. Both data sets can be fitted very well by a linear function with a fixed null intercept (Fig. 2.4(a) purple and blue dashed lines) within the experimental error, indicating that the deposition rate stays constant for different deposition times. The slope calculated by means of the least-squares linear fit provides the actual deposition rate at that specific power. The second calibration step consists of verifying the generally observed linear dependence between the deposition power and rates. Figure 2.4(b) displays two examples for Co (blue squares) and Ru (orange dots), using a fixed deposition time of 600 s, illustrating this

second step of the target calibration. The dashed lines display the linear fits to the data. The accurate characterization of the linear dependency between the sputtering power and the deposited thickness has allowed for precise alloy fabrication with different concentrations (as presented in Chapters 3, 4 and 5) by means of co-deposition from two or more guns simultaneously, since it permits for efficient interpolation of deposition rates.

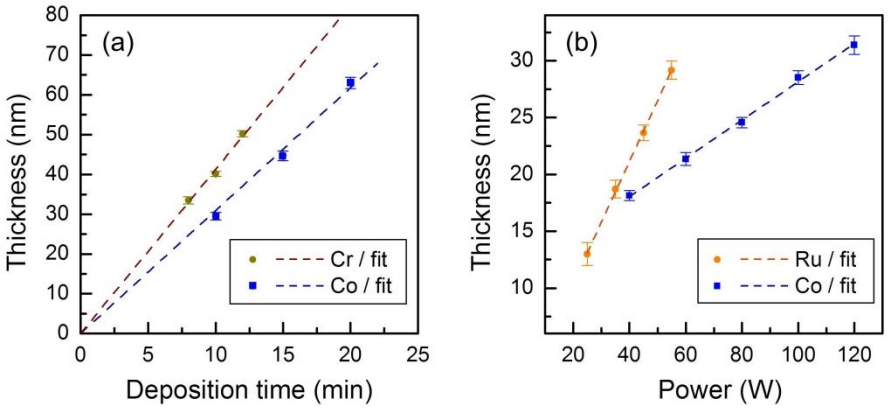

Figure 2.4: (a) shows the film thicknesses as a function of the deposition times at a fixed power of 100 W for Co (blue squares) and Cr (dark yellow dots). The dashed lines correspond to the linear least squares fits; (b) displays the film thicknesses as a function of sputtering power for a deposition time of 600 s for Co (blue squares) and Ru (orange dots). The dashed lines represent the linear least squares fits. In both cases the thicknesses have been measured by XRR.

In fact, in order to obtain the desired ratio between the alloyed materials, the deposition power and consequently the deposition rate has been adjusted by referring to the calculated linear fittings. The formula used to calculate the correct deposition rate to fabricate the desired alloy is:

$$A_{1-x}B_x \rightarrow \frac{dep.rate(B)}{dep.rate\ (A)} = \frac{x}{1-x} \times \frac{\rho_A}{\rho_B} \times \frac{m_B}{m_A} \qquad (2.1)$$

with $\rho_{A,B}$ being the density at room temperature and $m_{A,B}$ being the standard atomic mass. This expression is valid for equal deposition time of the two materials and constant deposition rates during the co-sputtering process. In the case of a very small *x*, too low or too high gun powers would be needed to obtain the specific alloy concentration. In order to overcome this problem, the dopant (lower concentration) metal or oxide target was connected to the RF power supply. By doing this, as shown in Fig. 2.5(a) for Cr, the deposition rate is reduced to half while the linear dependence between powers and the deposition rate is preserved.

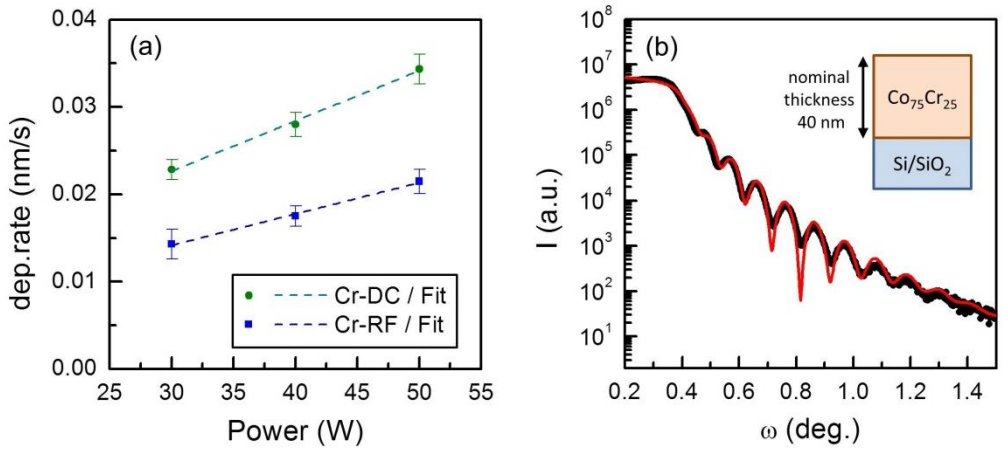

Figure 2.5: (a) deposition rate as a function of the gun power for Cr. The blue squares corresponds to deposition performed using RF whereas the green dots refers to DC-depositions. The blue and green lines correspond to the linear least squares fits to the two data sets. (b) X-ray reflectivity measurement of sputtered deposited $Co_{75}Cr_{25}$ alloy layer on top of Si substrate with its native oxide. The (red) solid lines represent the least-squares fit achieved with the X'Pert Reflectivity software.

In order to verify whether the different guns do not influence each other during the simultaneous deposition and that the resulting total deposition rate is simply the sum of the individual ones, several thickness calibrations of alloy samples have been performed. Fig. 2.5(b) shows the XRR data for a nominally 40 nm thick $Co_{75}Cr_{25}$ test sample, deposited by using previously calibrated deposition rates for the individual Co and Cr targets. From the data fit, which corresponds to the red line in Fig. 2.5(b), a thickness $t = 39.3 \pm 1.2$ nm has been determined for the $Co_{75}Cr_{25}$ film, which is in excellent agreement with the nominal target value for this alloy. Very similar results have been obtained by changing thickness, composition or materials, verifying that, by using the optimized sputter conditions described above and the proper sputter gun arrangement, the total deposition rate of multiple guns is the simple addition of the individual ones.

Finally, all the main parameters of the sputtering process are remotely controlled by a commercial software PHASE II, which furthermore allows the programing of the system in order to perform complicated multilayer or alloy deposition sequences automatically.

2.2. Structural characterization

Since crystalline structure and physical properties are closely related in most materials, the structural characterization has been a very relevant aspect of this thesis. The structural analysis of the deposited thin films has been primarily conducted by X-ray scattering

techniques, because of its suitability for thin-film analysis. In fact the X-ray photon wavelengths are of the order of atomic distances in solids, which make them especially suitable as structural probes. This technique is nondestructive and it leaves the investigated sample intact for the further characterizations. Moreover, this ex-situ method does not need any special environment and the measurements can be performed under standard ambient conditions.

2.2.1. X-ray Reflectivity

X-ray Reflectivity (XRR) measurements consist of collecting the intensity of a monochromatic X-ray beam of wavelength λ reflected by a sample. Hereby, the X-ray beam irradiates the specimen at a grazing angle ω and the reflected intensity is measured at an angle θ by a detector. The interaction between the X-ray radiation and matter happens through the scattering by the electrons of the atomic constituents via three different mechanisms: photoionization, Compton and Thomson scatterings. The first two are inelastic processes whereas the latter is elastic, i.e. the incoming wavelength λ of the X-rays is preserved. Actually, it is only the Thomson component that is detected in the experiments performed in this thesis. Fig. 2.6 illustrates the specular reflection geometry utilized by XRR, in which the incident and detection angles are equal, i.e. ω = θ. The reflection at the surface and interfaces is the result of different electron densities in the different layers, which correspond to different reflection indices in the classical optics nomenclature. Actually X-rays interact rather weakly with matter, and the refractive indices of most materials are slightly smaller than 1 at these wavelengths and are expressed as:

$$n = 1 - \delta + i\beta \tag{2.2}$$

where δ and β are the dispersion and absorption coefficients respectively [40,41]. The main consequence is the total external reflection at an air-medium interface for incidence angle smaller than a critical angle θ_c, as shown in Fig. 2.6(a). If ω equals θ_c, part of the incident light is reflected and part continues in a direction that is tangential to the boundary of the medium, marked by the red arrow in Fig. 2.6(b). If absorption is neglected, the value of the critical angle is simply proportional to the square root of the material density, X-ray wavelength and atomic number [40,41].

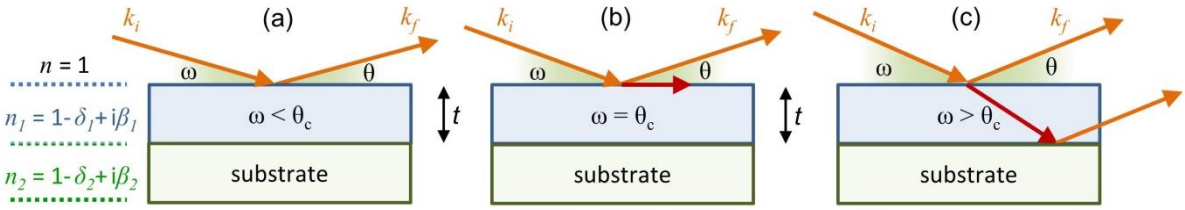

Figure 2.6: (a) incident angle ω is smaller than the critical angle θ_c; (b) the incident and critical angle are equal, so that X-rays can propagate along the sample surface; (c) $\theta > \theta_c$ the X-rays can actually penetrate into the material (red arrow).

This parameter hence contains relevant information about the material. For λ = 1.54 Å, which corresponds to the Cu K_α wavelength used in this thesis, θ_c for most material is less than 0.4° [40,41]. Finally, for incident angles greater than θ_c ($\omega > \theta_c$) the radiation penetrates inside the film and, due the presence of a second interface film (n_1) / substrate (n_2), as shown in Fig. 2.6(c), the corresponding reflected intensity I(θ) exhibits oscillations called Kiessig fringes. They are generated by constructive or destructive interference between the reflected X-rays from the top and bottom surfaces of the thin film. The period of these fringes gives an immediate approximate value of the thickness of the thin layer, with the separation of two maxima (minima) being inversely proportional to the film thickness *t*.

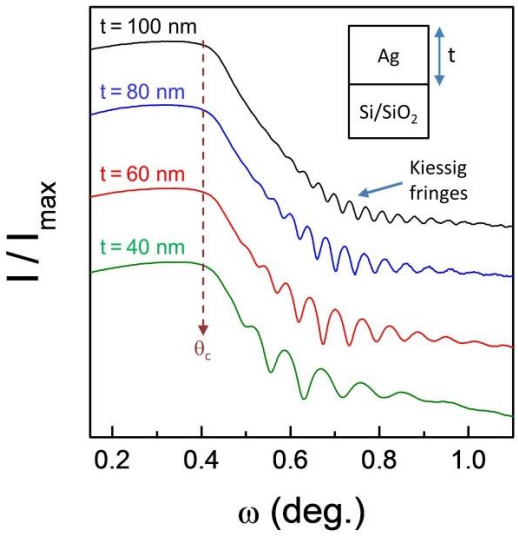

Figure 2.7: XRR measurement of sputtered deposited Ag layers of different thicknesses.

Fig. 2.7 shows XRR data of sputtered deposited Ag layers of different thicknesses. As can be clearly seen, the local maxima and minima in the normalized reflected intensity become more closely spaced upon increasing the layer thickness. At the same time, the measured

critical angle θ_c stays constant in the entire range of *t*, verifying the very good reproducibility of the material density of the sputtered films. Another important aspect is the amplitude of the oscillations, which is connected to the density contrast between the thin layer and the substrate. Moreover the decay in the total intensity and the damping of the fringes are influenced by X-ray absorption, as well as surface and interface roughness [40-42]. Therefore, X-ray reflectivity is a powerful method for studying and determining the layer thickness and material properties. In this thesis it has been primarily used to calibrate the sputter deposition rates and to verify film thicknesses.

2.2.2. X-ray Diffraction

In case the monochromatic X-ray beam irradiates a material at an angle ω, which possesses a three-dimensional periodic structure as displayed in Fig. 2.8, the scattered intensity will have a well-defined spatial distribution called the diffraction pattern, characteristic of the specific crystalline structure [40,41]. The condition of constructive interference is given by Bragg's law:

$$n\lambda = 2d \sin\theta \tag{2.3}$$

where *d* represents the interplanar spacing, λ the X-ray wavelength and *n* the reflection order. If the angles ω and θ are symmetrically changed, all the possible diffraction peaks from the specimen can be detected by recording the intensity spectrum I(θ).

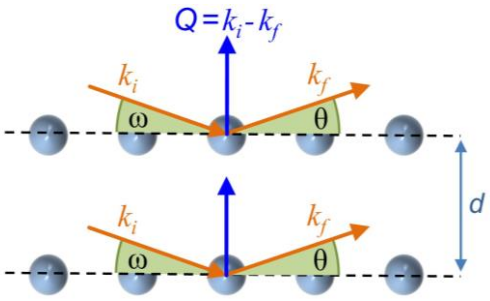

Figure 2.8: Schematic illustration of X-ray interference in crystallographic structures.

The angles at which constructive interference happens are directly related to the distance between the planes *d*, which are perpendicular to the scattering vector *Q*, defined as the difference between incoming and scattering wave vectors. Each diffracted peak can then be associated to the corresponding crystallographic plane that satisfies Bragg's law, which is typically classified using Miller indices. In order to perform a detailed structural

characterization of the sample fabricated in this thesis, four different diffraction geometries have been exploited, which are displayed in Figs. 2.9(a-d) [40,41]. Together with the canonical gonioscan method sensitive to the crystal planes parallel to the sample surface, shown in (a), rocking curve measurements have been performed in order to characterize the out of plane spread of crystalline grains, displayed in (b). Non-canonical gonioscans have been conducted by tilting the scattering plane to be parallel to crystalline plane not normal to the sample surface (c), which are also utilized in conjunction with φ-scan at the poles of preselected crystal planes in order to investigate in plane epitaxial relationship between the deposited layers and the substrate (d).

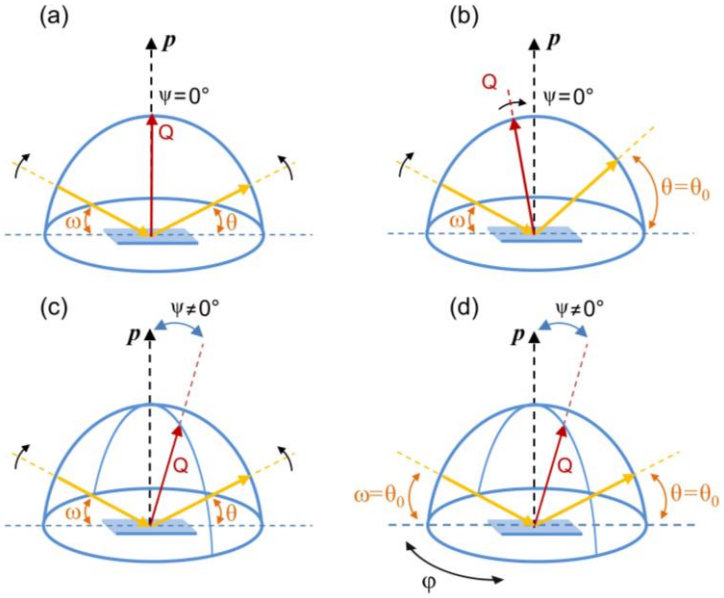

Figure 2.9: Schematic illustrations of the four different XRD measurements performed in the thesis: (a) gonioscan, (b) rocking curve, (c) "non-canonical" gonioscan and (d) φ-scan.

The entire X-ray characterization has been performed by means of a commerical X'Pert PRO PANalytical X-ray diffractometer equipped with a solid-state PIXcel detector. Copper has been selected as anode material to create the X-ray beam, and all the XRD measurements presented in this thesis have been done by using the K_α radiation ($\lambda = 0.154$ nm) after the suppression of the K_β by means of a hybrid monochromator.

2.3. Atomic and Magnetic Force Microscopy

Atomic Force Microscopy (AFM) is a powerful technique that belongs to the group of scanning probe microscopies (SPM) aimed at the measurements of local properties by

means of a probe, which typically is a cantilever with a sharp conic tip at its end [43,44]. The basic operational principle consists of recording the reflected intensity of a laser focused on the rear part of a cantilever by means of a four segment photodetector. Once the probe approaches the samples surface, the mechanical contact, Van der Waals and electrostatic forces interact with the tip deflecting the cantilever. The corresponding deflection is measured by the photodetector as a function of the lateral tip position. As a result, the topography of the sample surface can be measured. In order to scan the cantilever along the surface a piezoelectric actuator is used. In the case of a magnetically coated probe, the cantilever is additionally deflected by magnetic forces generated by the stray fields of the magnetized sample [43,44]. The corresponding Magnetic Force Microscopy (MFM) offers the possibility of high resolution imaging of various magnetic structures including domain walls, closure domains and recorded magnetic bits. MFM measurements have been carried out by performing a double-trace scanning at each image line: first the AFM scan tracks the topography and then, after lifting the magnetic probe up to a fixed distance from the surface, the second scan measures the long-range magnetic interactions between the tip and sample stray field by following the topography lines measured during the first scan. In this thesis, a high-resolution Nano-Observer CSI atomic force microscope has been utilized together with standard tips MAGT 50 from AppNano to measure the magnetic domain configurations presented in Chapter 4.

2.4. Magnetometry techniques

Magnetometry refers to a broad class of experimental techniques devoted to the macroscopic characterization of magnetic entities. They can be generally classified into two distinct types: inductive and force based. In this thesis the two most common inductive methods, vibrating sample magnetometry (VSM) and superconducting quantum interference device (SQUID) magnetometry have been used. Both techniques require the sample to be placed inside the magnetometer and by measuring its total magnetic moment as a function of temperature and magnetic field they provide information about the type of magnetic ordering as well as the presence of any phase transition that occurs at a critical temperature or magnetic field. Additionally, in order to have comparative measurements in

conjunction with volume averaged magnetometries, magneto-optical measurements and polarized neutron reflectometry were performed for the work presented in Chapter 3.

2.4.1. Vibrating Sample Magnetometer

In the VSM method [45,46], a sample is placed inside a suitably designed set of coils, known as detection or pick-up coils. By the application of a uniform magnetic field, a magnetic moment proportional to the sample susceptibility and the strength of the applied field is induced in the sample. By vibrating the latter, an electrical signal is induced into the coils according to the Faraday's law of induction [45,46], which is proportional to the magnetic moment *m* of the sample. The VSM used in this thesis is a commercial MicroMag^{TM} Model 3900 VSM System from Princeton Measurements Corporation, shown in Fig. 2.10(a). This instrument is a high sensitivity system (0.5×10^{-9} Am^2 with 1 sec. averaging time at room temperature). For these VSM measurements, the sample under study normally is glued onto a Kel-F (Polychlorotrifluoroethylene) sample holder by means of silicon grease, which in turn is screwed onto a carbon rod, Fig. 2.10(b). The latter connects the sample holder to a transducer assembly, which converts a sinusoidal AC drive signal into a sinusoidal vertical vibration to induce a sinusoidal motion of the sample. The pick-up coils are mounted directly on the poles of the electromagnet. The gap in between the electromagnet poles is adjustable and the maximum applied field achievable is $\mu_0 H = \pm$ 2.2 T, obtained with the minimum gap width of 1.3 cm. In order to place the sample in the proper and calibrated position between the coils and magnetic poles, the system has a linear translation stages that permits the movement along three axes. The experimental system also allows investigating the magnetic properties of materials as a function of temperature by inserting an oven in between the pickup-coils, as shown in Fig. 2.10(c). In order to fit into the gap, a larger distance between the poles is needed and the maximum applied magnetic field reduces to $\mu_0 H = \pm$ 1.8 T. During the oven operation, the sample zone is continuously evacuated by an extraction pump and filled with a constant flow of helium, nitrogen or argon gas in order to avoid undesired reactions with atmospheric oxygen. Moreover, to reduce temperature gradients, the oven is covered by a radiation shield. The temperature range accessible extends from $T = 293\,K$ up to $T = 1073\,K$. In order

to withstand high temperatures, a cleared fused silica (quartz) sample rod together with a MACOR (glass ceramic) sample holder have to be utilized, Fig. 2.10(d).

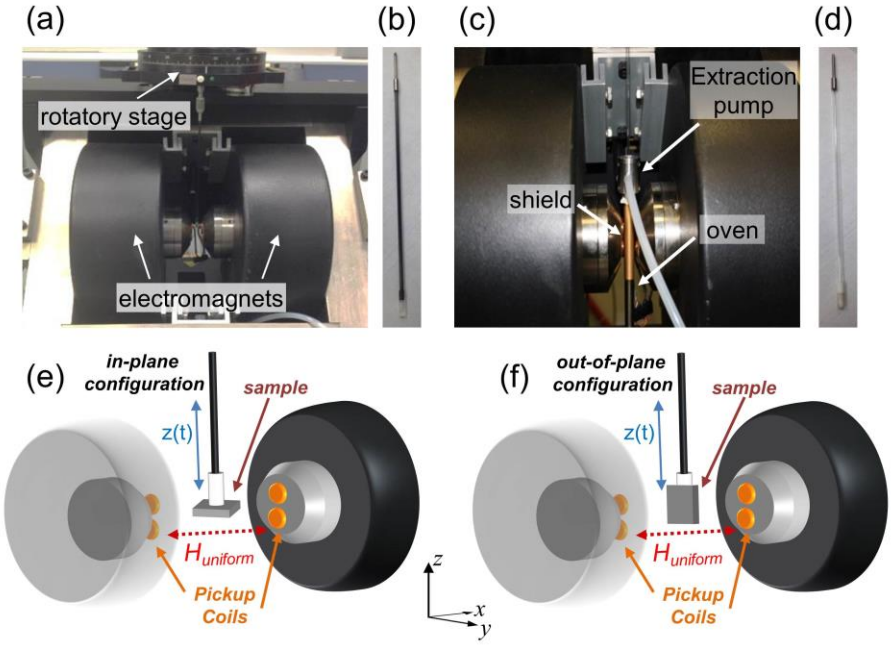

Figure 2.10: (a) front-view of the MicroMag™ 3900 model VSM system; (b) photograph of the carbon rod and Kel-F sample holder screwed at the bottom end; (c) picture of the sample area with the oven, heat shield and extraction pump; (d) photograph of the quartz crystal sample holder and MACOR sample holder screwed at the bottom end utilized for the temperature dependent measurements; (e) and (f) illustrate the schematic representation of the in-plane and out-of-plane geometries respectively.

Furthermore, different sample holder shapes allow for in-plane (IP) and out-of-plane (OP) magnetometry measurements, displayed in Fig. 2.10 (e) and (f) respectively, at any temperature. In the former geometry the external magnetic field is applied parallel to the sample surface (Fig. 2.10 (e)), whereas in the latter H is normal to it (Fig. 2.10 (f)). Moreover, angular dependent measurements of magnetic properties are possible due to a programmable rotation of the sample around the axis perpendicular to the applied field by means of a 360° rotatory stage, Fig. 2.10(a), which allows for an angular precision of better than 1°. It is worth mentioning that the absolute signal of the system has been calibrated by using an Yttrium Iron Garnet (YIG) sphere reference sample fabricated and measured at the US National Institute of Standards and Technology (NIST).

2.4.2. Superconducting QUantum Interference Device Magnetometer

The Superconducting QUantum Interference Device (SQUID) magnetometer is an instrument, which is sensitive to extremely weak magnetic signals [47]. The SQUID itself is made of two Josephson junctions in parallel and it is based on the interference of the currents from each junction. They are inductively coupled by means of a flux transformer to a set of superconducting detections coils, which are located outside the sample chamber, Fig. 2.11(a).

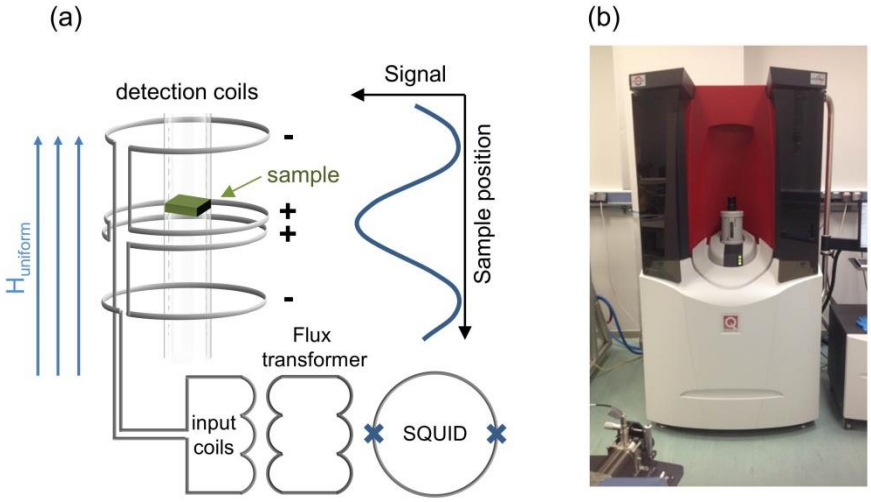

Figure 2.11: (a) simplified schematic of the SQUID detection system; (b) image of the SQUID-VSM system at CIC nanoGUNE.

The detection coils, the connecting wires, and the input coils form a closed superconductive circuit, Fig. 2.11(a). Therefore, any change of magnetic flux detected by the coils produces a change in the persistent current flowing through the detection circuit. This in turns produces variations in the SQUID output voltage that are proportional to the magnetic moment of the sample. Essentially, the SQUID acts as an extremely high sensitivity current-to-voltage converter. It is worth specifying that, in this specific case, the superconducting detection coils form a second derivative axial gradiometer (d^2B_z/dz^2), which detects a signal as a function of the sample position. A measurement can therefore be performed by moving the sample through the coils and the corresponding approximate shape of the signal detected, which is depicted in Fig. 2.11(a). By accurately calibrating the system using palladium and indium reference samples, measurements of the voltage variations from the SQUID detector as a function of a sample position provide a highly accurate measurement of the sample's magnetic moment. In order to take advantage of

lock-in techniques to isolate the sample signal from instrumental artifacts or electric noise, in this magnetometry system the sample can also vibrate at the center of the coils at a fixed frequency creating a signal at a known and desired modulation frequency [47,48]. This leads to magnetic signal sensitivity of better than 1×10^{-11} Am^2 for a one second averaging time. A superconducting magnet (a solenoid of superconducting wire) placed around the coils can apply fields up to $\mu_0H = \pm7$ T with a step resolution of $\Delta H = 5\times10^{-6}$ T [48]. The SQUID itself is usually placed well below the magnet and inside a superconducting shield in order to isolate it from external noise because of its extreme sensitivity. Given their superconductive nature, the SQUID and the magnet must be cooled with liquid helium which is also used to cool down the sample chamber from T = 400 K down to T = 1.8 K. Moreover the system is equipped with an EverCool system in order to virtually eliminate helium losses. The SQUID-VSM present at CIC nanoGUNE and utilized in this thesis is a commercial MPSM3 SQUID VSM EverCool system from Quantum Design, Fig. 2.11(b) [48].

2.4.3. Magneto-Optical Kerr effect based technique

The Magneto-Optical Kerr Effect (MOKE) describes a change in the polarization of reflected light due the spontaneous or induced magnetization of a specimen. Usually, *s* or *p* linearly polarized light is used to illuminate the sample for MOKE measurements. While the intensity of the reflected beam is almost preserved, the corresponding polarization plane rotates by an angle θ_K and the light acquires an ellipticity ε_K, resulting in an elliptical polarization state. Both quantities are linearly related (first order approximation) to the magnetization of the sample, whose evolution can be therefore traced by analyzing the polarization state of the reflected light beam as a function of the strength of the externally applied field [49-52]. In this thesis, the magnetic-optical characterization has been done in the longitudinal configuration by means of a bespoke setup, which is mounted on an optical table to suppress vibrational noise. A schematic is depicted in Fig. 2.12. The light coming from a 635 nm laser diode has been linearly polarized perpendicularly to the incident plane, i.e. *s*-polarization induced by polarizer P1. The sample is mounted on a holder connected to a high-precision motorized rotatory stage that allows full rotation around the surface normal with a resolution of 0.1°.

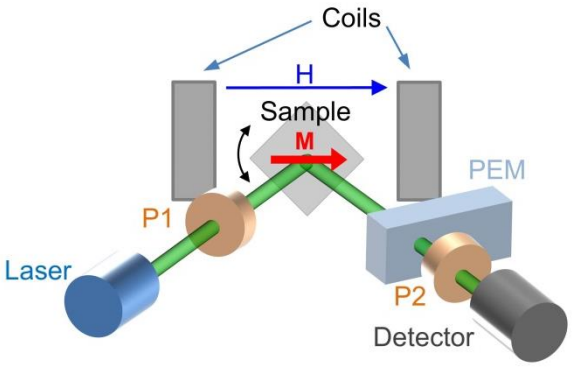

Figure 2.12: Schematic drawing of the bespoke MOKE setup.

Both are inserted within the gap of an electromagnet. The maximum strength of the magnetic field is $\mu_0 H = \pm 0.2$ T. The beam reflected by the sample passes through a photo-elastic modulator PEM, which provides a polarization modulation at a fixed frequency. After passing a second polarizer P2, the reflected light is then detected by a biased Si photodiode, whose signal is detected by a lock-in amplifier. This so-called polarization modulation technique [53] allows one to extract the ellipticity from the polarization state of the reflected light. In this way, one obtains a signal proportional to the component of the magnetization lying along the magnetic field direction, since the intersection between the surface plane of the sample and the scattering plane defines the sensitivity direction for the longitudinal MOKE configuration. It is worth mentioning that this technique is nondestructive and it can be utilized under standard ambient conditions with no need of specific sample shapes.

2.4.4. Polarized Neutron Reflectometry

Experimental techniques such as VSM and SQUID both yield volume averaged magnetic properties, whereas MOKE measurements provide information about a reduced volume of the sample proportional to the diameter of the beam spot and to the typical penetration depth of light, which is in the order of tens of nanometers in metals. Thus, none of these methods possesses depth sensitivity in order to resolve complex structural and magnetic depth profiles, which can be present in thin films and multilayers. In principle, properties of individual regions, as in the case of multilayer structures, can be deduced from careful modeling of standard magnetometry data. However, such an analysis is challenging and in most cases ambiguous when, for instance, properties of the multilayer vary along the thickness in a continuous manner, as in exchange spring structures or graded multilayers.

For such systems, a depth sensitive magnetic probe such as polarized neutrons can provide most relevant insights. Polarized neutron reflectometry (PNR) is thus a powerful technique developed as a means of studying depth-resolved magnetization in thin films and multilayers, with extraordinary spatial detail well below the surface. By measuring the neutron polarization before and after the scattering, significant information regarding the magnetization profile perpendicular to the scattering plane can be obtained [54-56]. There are several similarities between PNR and XRR techniques; however the intrinsic magnetic dipole moment μ_N of the neutron probe guarantee magnetic sensitivity through a very direct scattering interaction between μ_N and the magnetic induction of the sample. This is different from magnetic X-ray scattering contrast mechanisms, where the magnetic sensitivity arises from a more complicated absorption process. As a direct consequence, PNR is a straightforward technique able to determine magnetic moments in absolute units as well as nuclear composition as a function of depth.

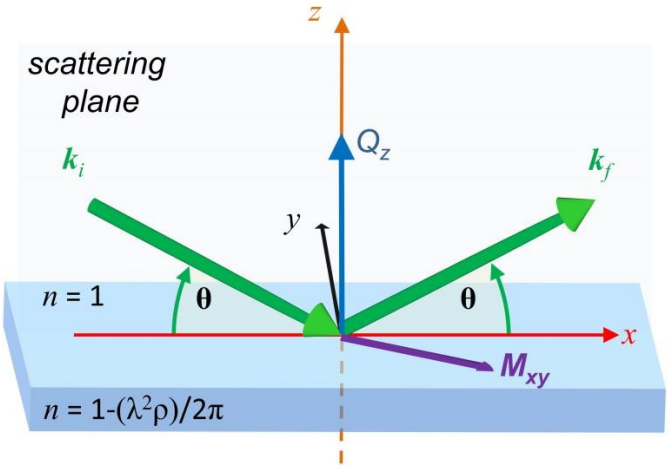

Figure 2.13: Schematic of the specular reflection.

By measuring the specular reflection as a function of the moment transfer $Q_z(\theta)$ (Fig.2.13), the in plane magnetization as a function of depth can be accurately determined. However, a basic prerequisite is the knowledge of the chemical composition and microscopic structure throughout the sample, usually determined by conventional X-ray reflectivity and diffraction. The moment transfer, which is normal to the sample surface, provides a convenient metric for characterizing the specular reflection process by measuring the reflectivity $R(Q_z(\theta))$ [54-56]. As in the case of X-rays, the neutron refractive indices of most materials are slightly smaller than 1, and given by:

$$n = 1 - \frac{\lambda^2 \rho_N}{2\pi} \tag{2.4}$$

with λ being the neutron wavelength and ρ being the spatial average of the scattering length density [54-56]. The latter quantity is defined as:

$$\rho_N = \sum_i N_i \, b_i \tag{2.5}$$

where N is the nuclei density, b is the nuclear scattering length corresponding to a particular isotope [106], and the summation is over each atom present in the scattering volume. Neutrons obey Snell's law and therefore a total external reflection at an air-medium interface happens for Q_z smaller than a critical Q_C. Beyond this limit, the neutron penetrates into the material and, in the presence of a second interface produced by the substrate, the corresponding reflected intensity $R(Q_z(\theta))$ exhibits oscillations generated by constructive and destructive interference [54-56]. In addition, $R(Q_z(\theta))$ decreases rapidly following a Q_z^{-4} law.

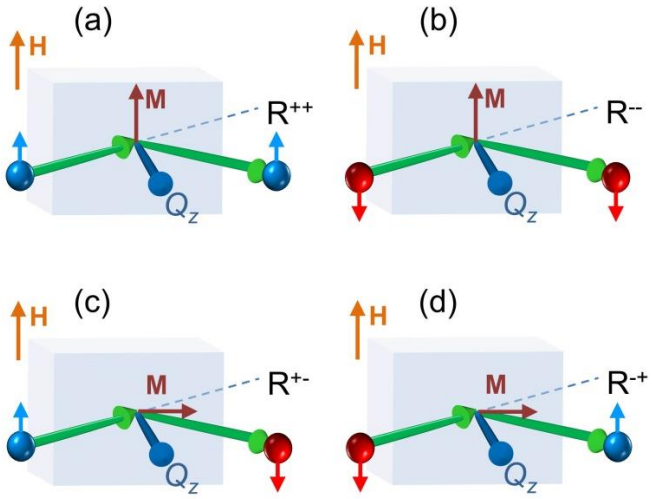

Figure 2.14: Schematic of the four different reflectivities occurring in PNR measurements: (a) and (b) show R^{++} and R^{--} non spin flip respectively while (c) R^{+-} and (d) R^{-+} spin-flip scatterings.

Furthermore, neutrons have two states of quantization and in the actual measurement they can be polarized either parallel (+) or antiparallel (-) with respect to the external field H. The sample, depending on its magnetization state, may induce a change in the polarization of the incoming neutrons. The reflectivities are then characterized by the sign of the neutron polarization before and after the reflection: R^{++}, R^{--}, R^{+-}, R^{-+} [54-56]. The first

and second superscripts denote the spin orientation of the incoming and scattered neutrons respectively. The non-spin-flip scattering, Figs. 2.14(a-b), is sensitive only to the components of the magnetization parallel to the neutron polarization whereas the spin-flip scattering, Figs. 2.14 (c-d), is associated with the perpendicular magnetization components. In this thesis, PNR measurements were carried out on the PBR beamline at the NIST Center for Neutron Research and conducted jointly with the beamline specialist Dr. Brian J. Kirby. A monochromatic cold neutron beam ($\lambda = 0.475$ nm) was incident on the sample surface, and the specular reflectivity was measured using a ^{3}He detector as a function of Q_z. An external magnetic field H was applied in the plane of the sample, and an Fe/Si supermirror / Al-coil spin flipper assembly was used to polarize the incident neutron magnetic moment either parallel (+) or antiparallel (-) to H. A second supermirror/flipper array was used to analyze the spin state of the scattered beam. The beam polarization was measured to be better than 90% for both polarization states. The data were corrected for background (determined from measurements taken with the detector offset by 0.3° from the specular condition), beam polarization, and beam footprint. Model fitting was performed using the NIST Refl1D software package [57], with parameter uncertainties determined using a Markov chain Monte Carlo algorithm [58,59]. Specular non spin-flip (R^{--}, R^{++}) and spin-flip (R^{+-}, R^{-+}) reflectivities were measured under various field and temperature conditions in order to characterize composition and magnetic depth profile discussed in Chapter 3 [56,60].

3. Artificially modulated exchange coupling structures

This chapter presents a thorough study that explores the viability of compositional effects being transferred into modulated magnetic states. Epitaxial heterostructures based on alloy thin films, whose composition mimic bathtub-like compositional profiles, reveal that by the precise tailoring of the magnetic profiles, the exchange coupling and the corresponding effective Curie temperature can be controlled over tens of nm with an excellent precision.

3.1. Introduction

Multilayer structures made from metallic magnetic and non-magnetic materials have revealed an impressive variety of novel collective properties, and they now represent an established and very successful approach to materials design with widespread applications [61,62]. The overall magnetic ordering in these artificial structures strongly depends on the interlayer and the intralayer couplings, and the corresponding basic magnetic properties, such as T_C or M_S, as well as the specifics of the multilayer dimensions [63-66]. Indeed, if the individual layers are sufficiently thick, their properties are bulk-like, and the multilayer corresponds to a simple superposition of separate layers. As they get thinner, the magnetic properties of those layers converge, and the multilayer can behave as a single new artificial material. One such example, in the limit of magnetic films in direct contact, are exchange spring permanent magnets, in which low moment magnetically hard and high moment magnetically soft layers are strongly coupled at the interfaces. As a consequence, the maximum energy product ($B{\cdot}H$) in this system is far enhanced in comparison to those of the constituent materials, if the geometry is properly designed [67-73].

This route to novel materials design has recently been taken further, with the accomplishment of a magnetic anisotropy gradient along the thickness of multilayer structures [74-80]. The key goal was hereby the decrease of the switching field down to very small values while maintaining thermal stability for the purpose of fulfilling the ever increasing demands of magnetic recording technology, and doing this by creating a new metamaterial with novel collective behavior. The fabrication of such graded media has historically been based on multilayered structures [81-87], in which extended interfaces are created by either directly tuning the thicknesses of the magnetic layers [82,84,85] or by interdiffusion via heat-treatment [81,83,86,87]. Additionally, the realization of a continuous anisotropy gradient was achieved in optimally annealed compositionally graded single layer films [88-92]. Furthermore, depth sensitive polarized neutron reflectivity (PNR) measurements allowed for a direct probing of the corresponding anisotropy gradient behavior [85,87-92]. The recently reported work in Ref. 93 demonstrated that not only an anisotropy gradient can be realized and tailored in compositionally graded single layer films, but instead the authors further disclosed an effective way to engineering phase transition and ferromagnetic phase boundaries parallel to the sample surface [93]. In fact

the specific sample structure of Ref. 93, a vertically graded Ni_xCu_{1-x} alloy films, revealed the possibility to map the temperature-dependence of the ferromagnetic order parameter onto spatial coordinates (i.e. a magnetic depth profile), which can be altered by both, temperature and magnetic field. Hereby, one has to consider that formally a magnetic material that exhibits ferromagnetic exchange coupling throughout should exhibit only one single Curie temperature, as defined in Section 1.1. Practically, however, in the presence of pronounced compositional gradients as the one studied in [93], the system can be thought of as having a continuous distribution of "local" or effective T_C, which leads to an effective spatial conversion of the M vs. T curve. The resulting depth-dependent T_C modulations were found to occur even at the nm length scale [93], which is a very relevant length-scale close to the exchange length (l_{ex}) of elemental ferromagnets and extremely important for applications, because it is fully compatible with the length-scale being employed in modern nanotechnology applications.

The main motivation of the present work is to investigate whether and how such effective Curie temperature depth profiles can be utilized to modify collective magnetic behavior, with particular emphasis on magnetization reversal, introduced in Section 1.1.4. Indeed, rationally designed composition profiles can be envisioned to achieve desired temperature and field dependencies in order to achieve complex collective or non-collective magnetic behavior. This may also have relevance for temperature-assisted magnetic recording technologies that are presently being explored for Hard Disk Drive (HDD) and Magnetic Random Access Memory (MRAM) applications. Here, the triggering of a temperature induced decoupling of different magnetic properties, namely magnetic reversibility and stability, is being pursued.

However, the fundamentals of the associated collective or only partially collective behavior will have to be studied first to allow for such applications. The work here is attempting to make a contribution towards an overall understanding of collective behavior in suitably designed gradient materials. Given this goal, $Co_{1-x}Cr_x$ alloys are an interesting model system, because they are ferromagnetic up to x = 0.35 [94-96], so that magnetic properties can be easily tuned by changing the Cr doping concentration x. Both T_C and M_S scale with the Co/Cr ratio, making the latter quantity a useful knob for their continuous tuning [93-96]. Moreover, the alloy forms a stable solid solution in a wide range of Cr

concentrations while preserving the *hcp* crystal structure characteristic of pure Co. For the present work a series of symmetrically graded samples of the form Co (20nm) / $Co_{1\rightarrow 1-x_c}Cr_{0\rightarrow x_c}$ (18nm) / $Co_{1-x_c}Cr_{x_c}$ (30nm) / $Co_{1-x_c\rightarrow 1}Cr_{x_c\rightarrow 0}$ (18nm) / Co (20nm) has been designed and studied, with x_c representing the maximum Cr content at the center of the structure, as shown in Fig. 3.1(a). The simplified nomenclature Co/$Co_{1-x}Cr_x$/Co will be used for the remainder of the chapter, with $Co_{1-x}Cr_x$ representing the "bathtub-like" compositionally graded structure, which has a total thickness of 66 nm. A key aspect and advantage of the specific sample structure is the fact that they can be grown epitaxial with uniaxial magnetocrystalline anisotropy in the plane of the film. Moreover, the selected thickness is far smaller than the lateral dimensions, resulting in negligible in-plane demagnetization fields. Correspondingly, the film magnetization is restricted to in-plane orientations only.

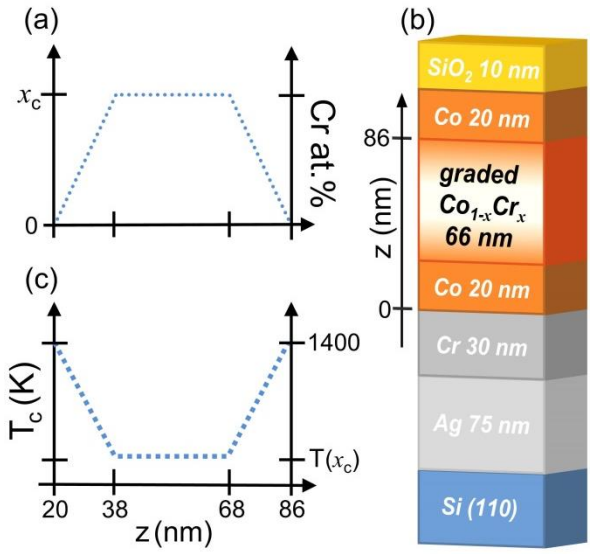

Figure 3.1: (a) shows the Cr content depth profile for the sample type studied in this work; (b) schematic of the layer growth sequence; (c) shows the associated effective Curie temperature T_C depth profile for the 66 nm thick graded $Co_{1-x}Cr_x$ layer.

The samples have therefore nearly ideal textbook magnetic behavior, which allows for comprehensive and precise quantitative data analysis and interpretation [97-99]. In contrast to the previous study where a linear composition gradient was employed [93], the symmetrically graded T_C "bathtub-like" profile here should allow for a tunable coupling of the two outer cobalt layers via the graded central region, with the coupling strength being dependent on the continuously tunable magnetization profile of the graded region itself [93-96]. In other words, the particular sample structure can be considered as having a non-

ferromagnetic "spacer" layer at the center whose thickness is continuously variable as a function of temperature. Such a tunable spacer should result in strongly temperature dependent magnetic coupling that significantly influences the magnetization reversal process.

3.2. Fabrication process

All samples have been fabricated by means of the sputter deposition system already described in Section 2.1.1. Prior to any deposition, the Si (110) substrates were cleaned in acetone to remove large particles and organic residues and subsequently in isopropanol to remove possible acetone residues. Finally the substrates were rinsed in deionized water. The native silicon oxide was then removed by using a wet hydrofluoric acid (HF) chemical etching. In this work a commercial solution of 2% HF in deionized water has been utilized at room temperature for 10 minutes, after which the substrates have been immediately transferred into the UHV sputter system.

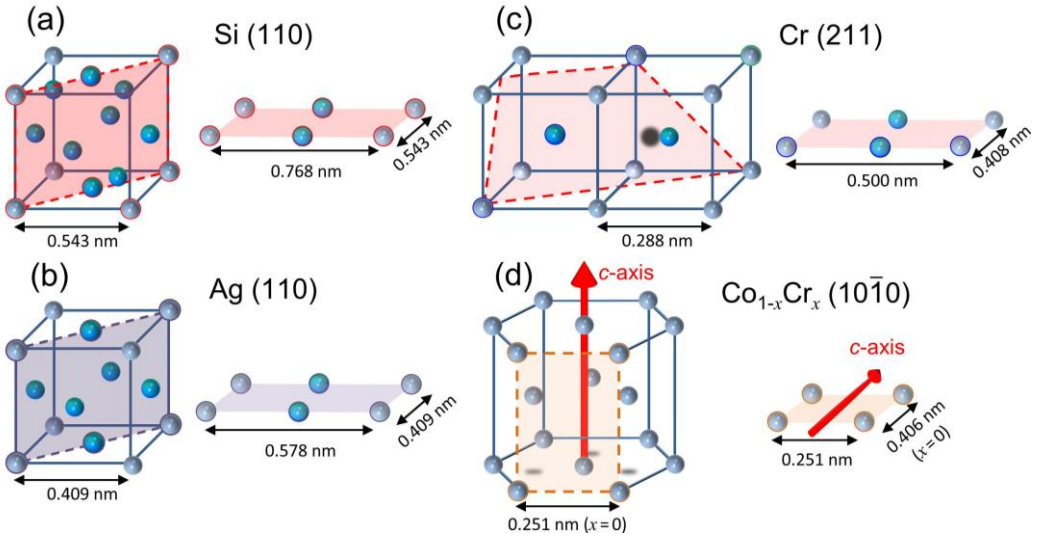

Figure 3.2: (a) single crystal orientation of the Si substrate; (b-d) crystal planes induced during the growth process with respect to the corresponding unit cells for the Ag (b), Cr (c) and $Co_{1-x}Cr_x$ (d) layers marked by rectangles delimited by dashed lines. The lattice dimensions refer to bulk parameters.

All depositions were performed at room temperature (RT) using a pressure of 4×10^{-1} Pa of pure Ar atmosphere. Graded layers were fabricated by co-sputtering of Co and Cr targets, keeping the power of the former fixed while changing that of the latter to achieve the intended composition profile. An onset layer of 75 nm thick Ag and a subsequent 30 nm thick Cr layer were deposited prior to the growth of the magnetic structure, in order to

achieve a high quality 20 nm thick $(10\bar{1}0)$ oriented Co layer [97-99]. As a reference, 106 nm thick epitaxial pure Co sample ($x_c = 0$) was fabricated using an identical underlayer sequence. The 20 nm thick Co $(10\bar{1}0)$ oriented layer served as a template for the epitaxial growth of the 66 nm thick compositionally graded $Co_{1-x}Cr_x$ layer. The fabrication of the corresponding "bathtub-like" structure was divided into three consecutive steps: the increment of the Cr content up to its maximum x_c was achieved by the stepwise increase of the Cr gun power every 3 nm of deposited film thickness; the central 30 nm thick $Co_{1-x_c}Cr_{x_c}$ layer was deposited keeping the sputter powers of both targets constant; the Cr sputter power was then progressively reduced again in 3 nm intervals. Afterwards, the 20 nm thick Co top-layer was deposited. The result was a magnetic structure that was nominally symmetric with respect to the center of the depth profile. The epitaxial relationships between the layers of the above described growth sequence can be seen in Figs. 3.2(a-d) based on their respective bulk lattices [97,99]. The Si substrate adopts a diamond cubic crystal structure with the (110) crystallographic plane resulting in a rectangular cell, as indicated in Fig. 3.2 (a). The Ag exhibits the face centered cubic (*fcc*) structure and the (110) crystallographic orientation corresponds to a rectangular unit cell (Fig. 3.2(b)). As reported by Ref. 97 and 99, despite an apparent considerable mismatch, a 2×4 Ag (110) supercell matches almost perfectly half of a 3×3 Si (110) supercell mesh. The afterwards deposited Cr adopts the body centered cubic (*bcc*) crystal structure and the (211) plane, depicted in Fig. 3.2(c), provides an excellent template for $Co/Co_{1-x}Cr_x/Co$ with its hexagonal close packed (*hcp*) crystal lattice structure and a $(10\bar{1}0)$ surface plane orientation, as shown in Fig. 3.2(d). As a final deposition step, each sample was coated with 10 nm of amorphous SiO_2 in order to avoid any oxidation or contamination. Fig. 3.1(b) shows a schematic of the described growth sequence, optimized to obtain the $(10\bar{1}0)$ orientation throughout the magnetic structure. Consequently the *c*-axis, which corresponds to the magnetic easy-axis, lays in the film plane resulting in a rather simple uniaxial in-plane magneto-crystalline anisotropy despite the complexity of the sample structure. Therefore, magnetization properties and related magnetization reversal should be simple, allowing for a comprehensive and precise quantitative data analysis by using the macrospin model illustrated in Section 1.1.5. Using the above growth scheme, a series of samples with x_c ranging from 0.25 to 0.32 has

been fabricated. It is worth mentioning that for each value of x_c the Cr concentration of the two linearly increasing and decreasing region of the sample has been adapted, i.e. a higher x_c corresponds to a steeper gradient dx/dz, while the total sample thickness was always constant. Fig. 3.1(c) illustrates the expected corresponding effective T_C distribution, derived from the combination of the compositional depth profile and the nearly linear relationship between T_C and x [93-96].

3.3. Structural characterization

Fig. 3.3 shows XRD θ-2θ measurements in the angular range $35° \leq 2\theta \leq 95°$ for several gradient samples that were grown with different maximum Cr concentrations x_c with each scan being displayed normalized to the intensity of its Ag (220) peak.

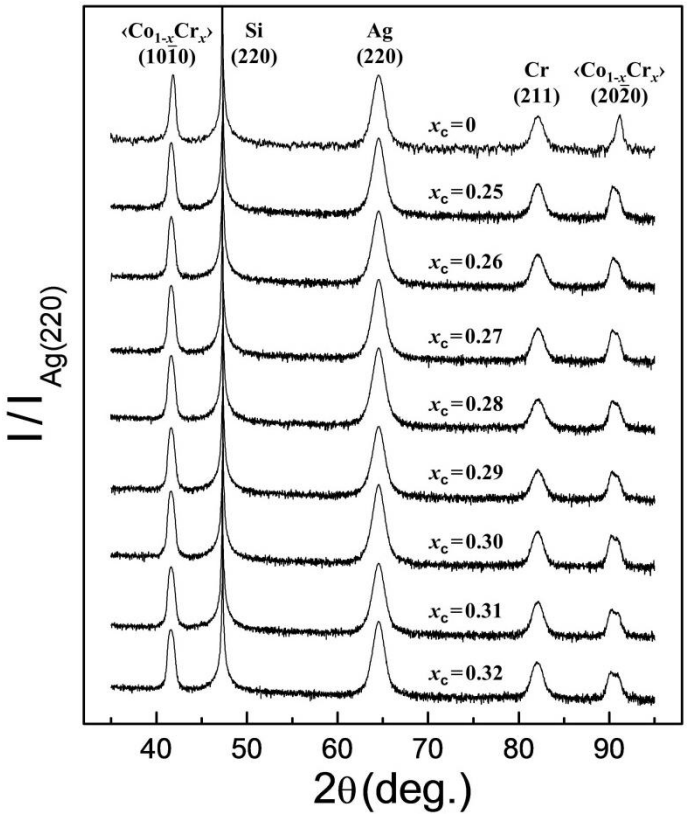

Figure 3.3: XRD θ-2θ scans for samples with different Cr concentrations x_c showing ‹$Co_{1-x}Cr_x$› (10$\bar{1}$0), Ag (220), Cr (211) and ‹$Co_{1-x}Cr_x$› (20$\bar{2}$0) diffraction peaks, in addition to the Si (220) substrate signal.

All the scans look nearly identical in their overall appearance, exhibiting only the well-defined diffraction peaks corresponding to Si (220), Ag (220), Cr (211), ‹$Co_{1-x}Cr_x$› (10$\bar{1}$0)

and (20$\bar{2}$0) crystal planes[3]. The absence of any other diffraction peak corresponding to non-epitaxial orientations and the fact that higher order diffraction signals are clearly visible in all cases are evident indicators of the excellent crystallographic quality of the samples. In addition, the full width at half maximum (FWHM) and the position of the peaks corresponding to the Ag and Cr seed layers, which serve as templates for the growth of the actual magnetic structures, are identical within the experimental precision in all cases, verifying the robustness of the fabrication process. This also permits to correlate any significant structural changes in the graded layers to the different Cr gradient compositions instead of a variable quality for the template layers. As illustrated in Fig. 3.3, it can be asserted that all graded samples show an out-of-plane crystallographic orientation quality that is very similar to the 106 nm thick pure Co reference sample (x_c = 0), despite their complex depth dependent structure. In contrast to usual X-ray diffraction peaks from homogeneous film, the nature of the peaks corresponding to the ‹$Co_{1-x}Cr_x$› (10$\bar{1}$0) and (20$\bar{2}$0) orientations is quite different and worth discussing further.

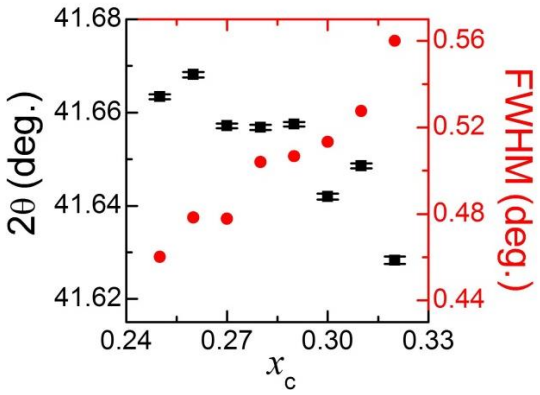

Figure 3.4: XRD ‹$Co_{1-x}Cr_x$› (10$\bar{1}$0) peak positions (black dot) and FWHM (red dots) as a function x_c.

Each of those Bragg peaks corresponds to a superposition of the signal coming from the two outer Co layers and the signal coming from the interior graded $Co_{1-x}Cr_x$ structure. By using a single Gaussian fitting function, the position of the (10$\bar{1}$0) peaks was found to decrease with increasing x_c whereas the corresponding FWHM increases, as shown in Fig. 3.4. Normally, such a peak width increase is associated with a reduced quality of the epitaxial growth. However, in the compositionally graded samples, it is primarily linked

[3] Only in this chapter ‹$Co_{1-x}Cr_x$› indicates the Co/$Co_{1-x}Cr_x$/Co “trilayer” structure.

to the superposition of the diffracted X-rays from different depth segments of the modulated structure. Indeed, it is the lattice expansion in the central part of the gradient structure that causes the enhanced width of the ‹$Co_{1-x}Cr_x$› $(10\bar{1}0)$ peak, changing from 0.46° for the x_c = 0.25 sample to 0.57° for the x_c = 0.32 structure. This evolution is even clearer for the $(20\bar{2}0)$ second order Bragg reflections where the overall graded crystallographic structure leads to a splitting of the peak upon increasing x_c. Part of this double peak structure appears at an angular position close to that of pure Co, which can be attributed to the bottom and top parts of the structure. In contrast the signal from the central region is shifted to lower diffraction angles, indicating a slight lattice expansion, which is x_c dependent.

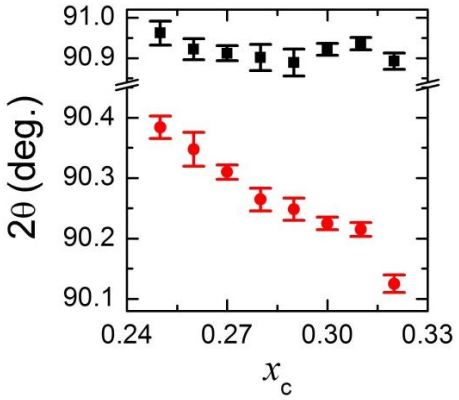

Figure 3.5: XRD ‹$Co_{1-x}Cr_x$› $(20\bar{2}0)$ peak positions as a function x_c evaluated by a double Gaussian fit function.

By using a double Gaussian fitting function, the position of the $(20\bar{2}0)$ peaks corresponding to the central region was found to decrease with increasing x_c whereas the diffraction angles corresponding to the outer parts stay constant in the entire concentration range, as shown in Fig. 3.5.

Figs. 3.6(a-d) show XRD φ-scans for four samples with different maximum Cr concentration, namely x_c = 0.25, 0.28, 0.30 and 0.32. The measurements were performed at four different crystal planes that are not parallel to the film surface and thus provide information about the in-plane orientation between the layers. The intensity has been normalized to the maximum value in each corresponding measurement. All φ-scans show two well defined diffraction peaks that are 180º apart, and whose positions match the stereographic projection of the nominal epitaxial structure [97].

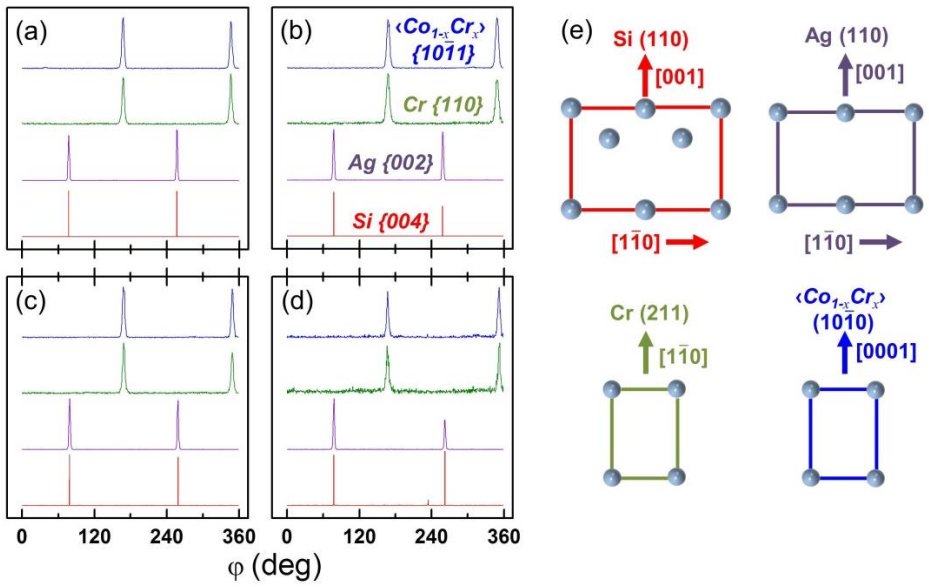

Figure 3.6: XRD φ-scans at the 2θ poles of the Si {400}, Ag {200}, Cr {110} and ‹$Co_{1-x}Cr_x$› {10$\bar{1}$1} planes for x_c= 0.25 (a), 0.28 (b), 0.30 (c) and 0.32 (d). (e) displays the corresponding epitaxial relations between subsequent layers in the sequence.

The 90° angular shift between the Si {400} and Ag {200} scans with respect to the Cr {110} indicates that the Cr [1$\bar{1}$0] and Ag-Si [001] directions are parallel [97,99]. The ‹$Co_{1-x}Cr_x$› peaks appear at the same positions as those in the Cr {110} scan, verifying the parallel alignment between the ‹$Co_{1-x}Cr_x$› [0001] and Cr [1$\bar{1}$0] directions. The overall narrow FWHM verify single crystal orientation for all samples. Moreover there is no significant change between the φ-scans for the different samples, further corroborating the quality and reproducibility of the growth procedure.

The structural analysis of all the samples thus verifies excellent crystallographic quality and well-ordered ‹$Co_{1-x}Cr_x$› graded film with in-plane *c*-axis orientation, which is the easy axis of magnetization for such alloys in the entire composition range.

3.4. Magnetic characterization

The macroscopic magnetic properties were analyzed in order to verify that the designed graded structures exhibit the expected uniaxial magneto-crystalline anisotropy with its easy axis in the plane of the film and parallel to the *c*-axis. Figs. 3.7(a-e) display room temperature normalized magnetization M/M_S data as a function of the field strength H and the field angle β, which is defined by the in-plane applied field direction with respect to the crystallographic *c*-axis. The data are shown as color-coded maps for samples with x_c = 0,

0.25, 0.28, 0.30, 0.32. To assemble these data sets, the magnetization has been measured by sweeping the field strength H, from positive saturation down to zero at every field orientation angle from $\beta = 0°$ to $\beta = 360°$ using a step size of 2°. All the data show a clear 180º periodicity, with the presence of a cone shaped structure of reduced magnetization occurring near $\beta = 90º$ and $\beta = 270º$. These cones are expected around the hard axis, because without sufficiently high external magnetic field, the system has negligible magnetization along the field axis, as shown in Fig. 1.5(b). Along $\beta = 0º$ and $\beta = 180º$, the external magnetic field has very little influence on the observed magnetization, because M is saturated along those directions even in the absence of H. These angles correspond to the easy axis (Section 1.1.5). The experimental maps indicate that all the samples exhibit uniaxial anisotropy with the easy axis coinciding with the *c*-axis, mimicking the perfect textbook behavior of the macrospin model described in Section 1.1.5. While the observed behavior is fundamentally identical in all cases, the pure Co reference sample shown in Fig. 3.7(a) exhibits a smaller "cone structure" around the hard axis than those of the graded samples. This corresponds to a lower anisotropy field H_K for the pure Co sample, whose definition in Eq. 1.10 has been modified here to take into account the second order anisotropy[4]:

$$H_k = 2\left(\frac{K_1 + 2K_2}{\mu_0 M_s}\right) \tag{3.1}$$

This might be related to a growth induced strain release with thickness [100]. Nevertheless, the $M(H,\beta)$ data exhibit only minor quantitative variations upon changing the alloy composition, which means that the anisotropy symmetry and the easy axis orientation are neither impacted by the Cr concentration, nor by the compositional gradient structure. In order to extract the volume-averaged magnetic properties, specifically H_K and M_S as a function of x_c, least-squares fits of the entire (not normalized) data sets have been performed by using the macrospin model presented in Section 1.1.5 including the second order anisotropy energy term[4] [98,101]:

$$E = -\mu_0 M_s H \cos(\beta - \alpha) + K_1 \sin^2\alpha + K_2 \sin^4\alpha \tag{3.2}$$

[4] The second order anisotropy constant has been included in Eq. 3.1 and 3.2 since its value is well known to be relevant in Co-material systems [98,101].

where α, the angle defined by the magnetization direction[5] with respect to the easy axis, is numerically determined by energy minimization for each (H,β) pair [98].

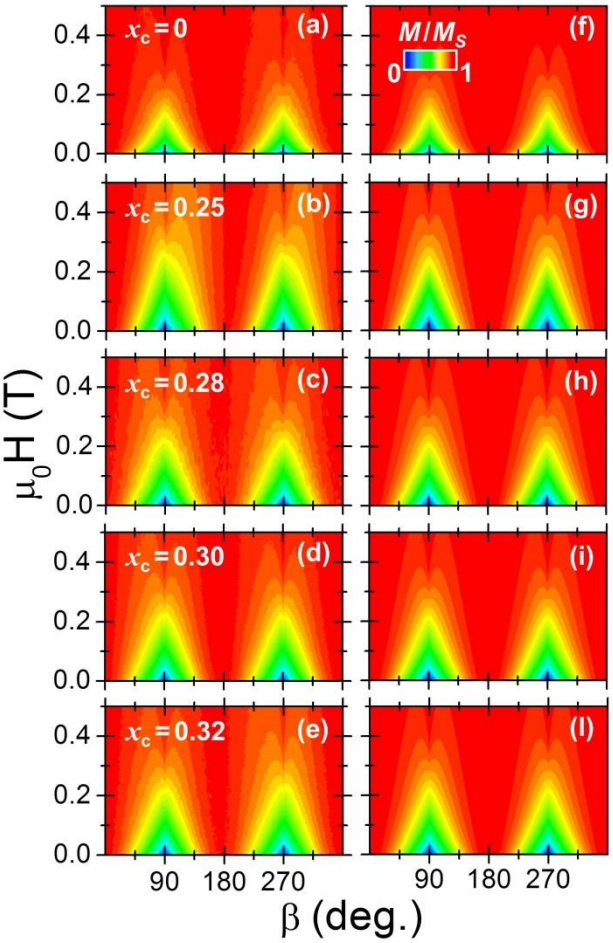

Figure 3.7: Color coded maps, representing the RT in-plane angular dependence of the magnetization measured from saturation to remanence for five samples with different Cr concentrations x_c (a-e). The data are normalized to the saturation magnetization M_S evaluated by least-squares fits using Eq. 3.2, and are plotted as a function of the applied field angle β with respect to the easy axis and the field strength H. (f-l) show the corresponding least-squares fits of the data based upon the minimization of the total energy [98].

The saturation magnetization, first and second order magneto-crystalline anisotropy constants, respectively K_1 and K_2 [101], are the only fit parameters used for each of the non-normalized magnetization maps. Results of the fits (Figs. 3.7(f-l)) exhibit excellent agreement with the experimental data (Figs. 3.7(a-e)), with an average R^2-value of 0.975. The room temperature saturation magnetization M_S values, extracted from the fits, are

[5] Both the magnetization M and the external applied field H lie in the x-y plane perpendicular to the z-axis, which is parallel to the sample surface normal.

shown in Fig. 3.8(b) as a function of x_c. As expected, M_S decreases upon increasing the Cr content [94-96]. At the same time, uniform $Co_{1-x}Cr_x$ alloy samples with x = 0.28 or larger are expected to be no longer ferromagnetic at RT (Fig. 3.8(a)) [94-96]. The reason why the extracted M_S values plotted in Fig. 3.8(b) do not drop down to zero for the high x_c regime is due to the saturation magnetization of the two Co-layers on top and bottom of the structure, which are essentially not influenced by the compositional gradient. Thus, the total volume-averaged moment has a lower bound given by the M_S of the pure Co layers times their volume fraction. The x_c-dependence of H_K is plotted in Fig. 3.8(c). It shows that the anisotropy field is nearly independent of the graded film concentration.

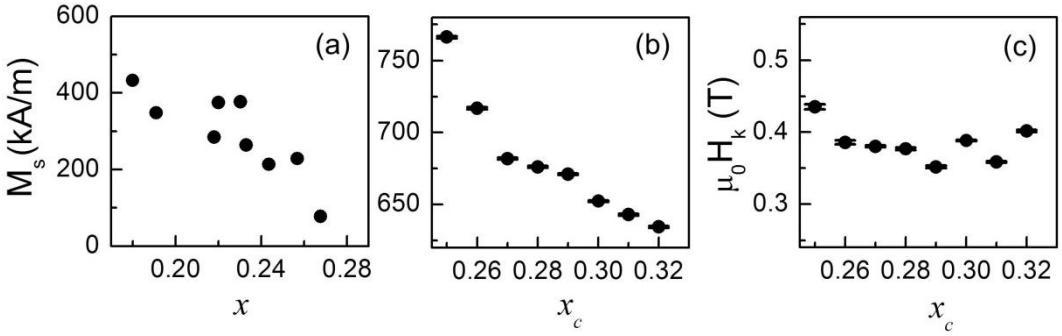

Figure 3.8: (a) room temperature M_S of uniform $Co_{1-x}Cr_x$ alloy samples adapted from [94]. RT magnetic properties for the graded epitaxial $Co/Co_{1-x}Cr_x/Co$ $(10\bar{1}0)$ samples as a function of Cr content x_c: (b) saturation magnetization M_S, (c) magnetocrystalline anisotropy field H_K.

The reduction of K_1 and K_2 upon increasing x_c is very similar to the decrease of M_S with x_c, which implies that H_K should remain nearly constant in the entire concentration range. Therefore, despite the strongly depth dependent compositional structure present in the samples, all of them exhibit a well-defined uniaxial magnetic anisotropy.

The remainder of the magnetometry investigation focused on the magnetization reversal processes occurring in these graded film structures. Figs. 3.9(a-d) show room temperature easy axis hysteresis curves for four selected samples, measured via VSM. In Fig. 3.9(a) the measurement shows a perfectly square-shaped hysteresis loop for the x_c = 0.25 sample, with an abrupt magnetization reversal at the switching field H_S, which in this particular case coincides with the coercive field H_C. In contrast, Fig. 3.9(b) displays a hysteresis loop in which the reversal of the magnetization occurs in two steps, similar to the reversal of two separated magnetic layers with distinct switching fields [102]. Figs. 3.9(c-d) show that the difference between the two H_S increases progressively with x_c while

the full remanence is preserved after positive and negative saturation. Intriguingly, the volume averaged magnetization equals zero after the first reversal step. Given the symmetry of the structure, and uniqueness of the switching fields, this intermediate state is likely to correspond to a stable antiparallel magnetic configuration of the top and bottom halves of the samples with one-half reversing before the other to produce zero net magnetization.

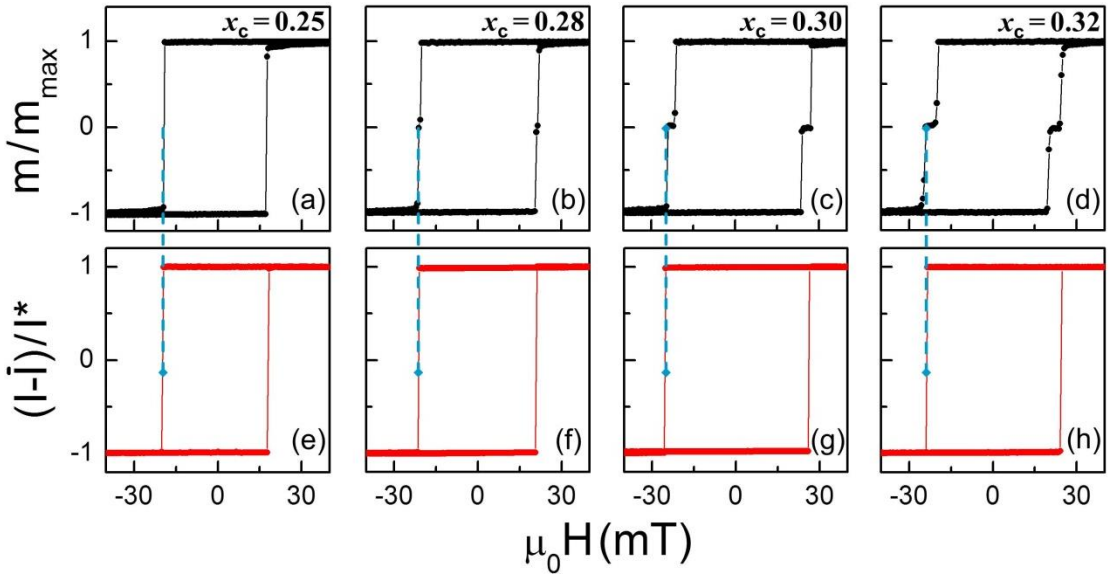

Figure 3.9: (a-d) VSM room temperature *m* (H) measurements along the EA for four different samples with Cr concentrations x_c. The data are normalized to its maximum value m_{max} in each case. (e-h) show the corresponding MOKE measurements acquired by using the same sample geometry and field resolution for direct comparison. The dashed light blue lines are guides to the eyes to compare the magnetic switching fields in between these two types of measurements. The MOKE data are processed in each case by first subtracting $\bar{I} = (I_{max}+I_{min})/2$ and then the resulting field dependent signal has been normalized by $I^* = (I_{max}-I_{min})/2$.

While VSM and SQUID both yield volume averaged magnetization values, MOKE measurements provide information about the top part of the sample due to the typical penetration depth of visible light in metals that is only tens of nanometers, less than half of the symmetric structure's total thickness [51,103]. Thus magneto-optical (MO) measurements have been performed, using the bespoke setup described in Section 2.4.3, in order to have comparative measurements and to gain deeper insight into the reversal process by comparing such MOKE data with volume averaged magnetometry results. Fig. 3.9(e) displays the MOKE loop for the x_c = 0.25 sample along the EA. The measurement shows that the reversal between the two uniform magnetization states occurs via a single abrupt transition at the same value of the magnetic field measured for the entire sample via

VSM. This confirms that for the x_c = 0.25 the magnetic correlation throughout the sample is so strong that the entire system switches collectively, even in the presence of the depth dependent concentration gradient. Since the x_c = 0.25 alloys are themselves ferromagnetic at room temperature, ferromagnetic coupling in and between all layers of the sample is expected. However, a discrepancy emerges between the MOKE and VSM measurements for $x_c \geq 0.28$. As shown in Figs. 3.9(f-h), single-step transitions are always measured by MOKE, revealing that the surface switches as a single magnetic layer. In contrast, the VSM data for these samples show two-step reversal. As can be seen from the dashed (blue) lines in Fig. 3.9, the single step transition observed via MOKE corresponds to the second switching field revealed by the VSM. This means that the bottom halves of all samples with $x_c \geq 0.28$ switch at lower fields, and the top halves at higher fields. It is likely that the different switching fields for the top and bottom halves arise from different strain fields within the layers, e.g., as a result of growth sequence. Together, these measurements imply that when x_c is sufficiently large, the samples are not correlated throughout the thickness, with the top layer switching independently from the bottom layer.

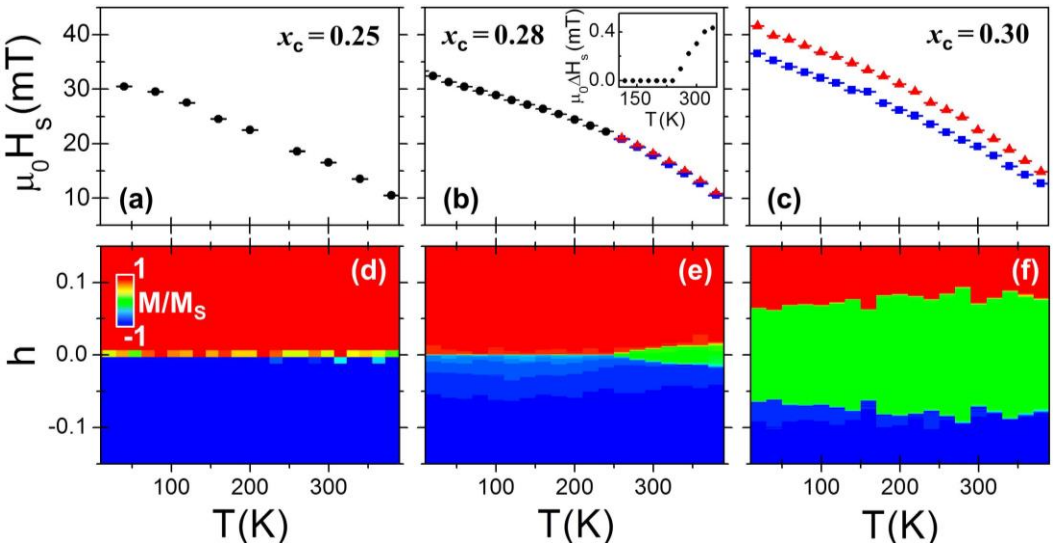

Figure 3.10: (a-c) H_S (T) for x_c = 0.25, 0.28 and 0.30. The (black) circles indicate "one step" reversal, while the (blue) squares and (red) triangles indicate the values for "two-step" behavior. The inset in the central top panel shows the difference between the two H_S for the x_c = 0.28 sample as a function of temperature. (d-f) show color coded-maps of the field dependent magnetization as a function of temperature measured along the EA for the hysteresis loop branches with decreasing field strength. The data are normalized to M_S, i.e. M/M_S equal to 1 represents positive magnetic polarization (red color), while -1 expresses negative saturation (blue color). The individual figures on the top and the bottom correspond to the same sample each.

The loss of ferromagnetic coupling between the top and bottom magnetic layers is expected when the central $Co_{1-x_c}Cr_{x_c}$ layer is approaching or is already in its paramagnetic state. Otherwise, the coupling should be strong. Therefore, a strong dependence on temperature should exist, which controls the magnetic phase at the center of the structure.

Temperature dependent $M(H)$ measurements were thus performed in order to explore the possibility of observing a temperature driven transition between a fully correlated and partially correlated magnetic structure. Fig. 3.10(a) displays H_S as a function of temperature for the $x_c = 0.25$ sample. Single switching behavior of the magnetization is observed in the entire temperature range explored despite the presence of a compositional gradient in the sample. Moreover, $H_S(T)$ behaves as expected for a "single layer material" for which K_i increases upon lowering the temperature and thermally-assisted switching is reduced.

In contrast, the $x_c = 0.30$ sample shown in Fig. 3.10(c), exhibits two-step reversal for all temperatures accessible by the experimental setup. As before, the reduction of the thermal energy leads to a shift towards higher values for the two switching fields connected to the top and bottom halves of the structure, but both shift in a similar fashion, so that a two-step reversal process persists for all temperatures. On the other hand, an intermediate $x_c = 0.28$ exhibits two-step switching above $T = 260$ K, but one step reversal below this "transition" temperature, as seen in Fig. 3.10(b). The inset shows the temperature dependence of the difference between the two switching fields H_S, which seems to follow a critical type behavior [104,105]. In order to better visualize the different switching regimes, Figs. 3.10(d-f) display normalized magnetization M/M_S color-coded maps as a function of temperature and the reduced field $h = (H-\overline{H}_S)/\overline{H}_S$, with $\overline{H}_S$ being the average of the two switching fields or the actual switching field for the one step process. Fig. 3.10(d) illustrates that one-step magnetization switching occurs for all the temperature explored for $x_c = 0.25$, highlighted by the presence of only two uniformly colored areas, whereas Fig. 3.10(f) shows in the same temperature range the constant presence of an intermediate magnetization state with $M/M_S = 0$ (marked by the green color) for $x_c = 0.30$. The transition between the two different regimes can be clearly seen in Fig. 3.10(e) where the two-step reversal, indicated by the triangular-shaped (green) area, disappears at $T \approx 260$ K.

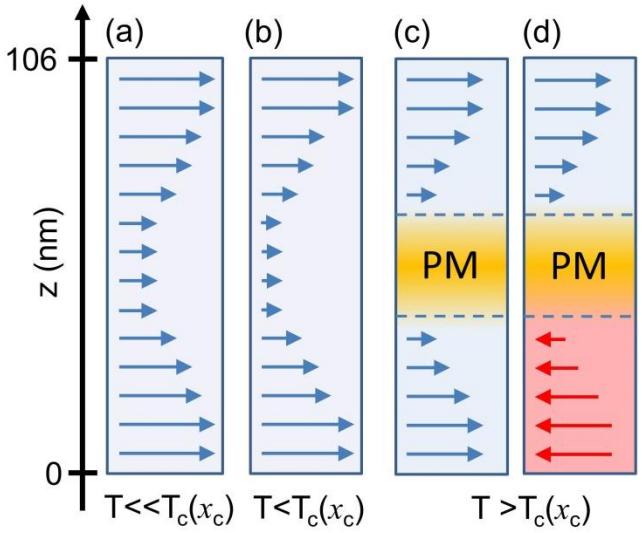

Figure 3.11: Schematics of the magnetization depth profile at remanence for temperatures below (a, b) and above (c, d) the minimum effective T_C. For high temperatures, the paramagnetic (PM) region interrupts the effect of the exchange coupling along the surface normal, allowing the system to be in either a parallel (c) or antiparallel (d) configuration.

The data in Fig. 3.10 demonstrate two things. First, the magnetization reversal mechanism can be continuously tuned by means of the alloy composition in graded structures, which allows the control of the effective exchange strength and thus the magnetic correlation along the surface normal. Second, choosing the concentration profile appropriately allows one to engineer a graded system that can undergo a transition from a collective one-step to a two-step reversal as a function of temperature.

Fig. 3.11 shows a schematic of the corresponding evolution of the magnetic depth profile for the x_c = 0.28 sample that would explain the observations. By considering the compositionally graded sample to constitute an exchange coupled multilayer system, in which each layer develops a temperature dependent magnetization that is determined by an effective Curie temperature associated with its local composition. Following the designed sample structure, the middle layer has the lowest J, M_S and effective T_C, and hence it is the layer most sensitive to temperature changes. When the temperature is below the effective T_C of this layer (Figs. 3.11(a,b)), the system exhibits a depth dependent M profile, which does not go to zero even in the center of the structure and thus the entire structure behaves like a single magnetic entity. Once the temperature crosses the minimum effective T_C of the $Co_{1-x_c}Cr_{x_c}$ layer, the structure essentially breaks into two magnetic entities, as shown in Fig. 3.11(c). In this case, the magnetizations of the top and bottom regions do not have to

be correlated allowing an external magnetic field to set the structure into an antiparallel alignment, if they have distinct switching fields (Fig. 3.11(d)).

3.5. Polarized Neutron Reflectometry

Given the impracticability, if not outright impossibility of probing the existence of the magnetic modulation and its suggested evolution by using standard magnetometry techniques, the direct measurement of the depth-dependent magnetic profile and its temperature dependence has been performed by the polarized neutron reflectivity (PNR), technique described in Section 2.4.4.

Depth dependent magnetic profiles of the x_c = 0.28 sample were obtained by PNR measurements as a function of temperature and magnetic field. After positively saturating the sample along the easy axis, non-spin-flip measurements, in which the original neutron polarization is preserved, were conducted in a near remanent field $\mu_0 H$ = +1 mT over a temperature range of 4 K ≤ T ≤ 300 K. As an example, Fig. 3.12(a) shows the R^{--} and R^{++} measured at T = 4 K as well as their associated model fit. The data exhibit spin-dependent oscillations generated by constructive and destructive interference as a function of Q_z, which indicate sensitivity towards nuclear and magnetic depth profiles. Since the difference between R^{--} and R^{++} signals scales with the component of the in-plane magnetization parallel to H, the magnetic contribution to the data is usually highlighted by plotting as spin asymmetry A:

$$A = \frac{(R^{++} - R^{--})}{(R^{++} + R^{--})} \tag{3.3}$$

The low Q_z spin asymmetry values at T = 4 K and 300 K and their model fits are shown in Fig. 3.12(b). Since the Co layers provide the dominant contribution to this signal, and their magnetizations are slightly reduced over this temperature range, the T = 4 K and T = 300 K spin asymmetries are overall rather similar. However, close inspection reveals definitive differences, demonstrating sensitivity to the temperature dependence of the magnetic depth profile. The data at all temperatures were well fit by the nuclear profile shown in Fig. 3.12(c). This model is highly constrained, with fixed literature values used for the number density N, and the nuclear scattering length b, of all elements [106]. The nuclear scattering

length density[6], defined in Section 2.4.4, is calculated using the nominal x profile for the $Co_{1-x}Cr_x$ multilayer (Fig.3.12(c)).

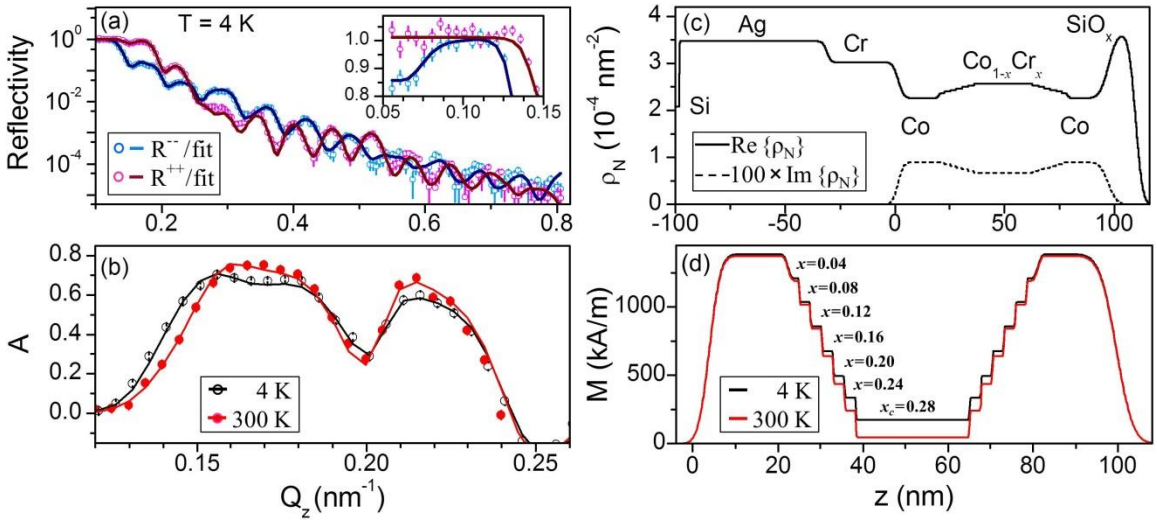

Figure 3.12: (a) fitted PNR data for x_c = 0.28 measured at T = 4 K in μ_0H = 1 mT along the easy axis following prior saturation via a μ_0H = 700 mT field; inset highlights low Q_z spin-splitting originating from the imaginary component of the Co scattering length density. (b) Low Q_z fitted PNR spin asymmetry data measured in μ_0H =1 mT at T = 4 K (open, black) and T = 300 K (filled, red). (c) Nuclear scattering length density model used to fit data for all field and temperature conditions. (d) Magnetization depth profile used to fit the data at T = 4 K (black) and T = 300 K (red). Error bars correspond to ± 1 standard deviation.

Although the imaginary component of ρ_N for Co is more than 2 orders of magnitude smaller than the real component, it has been accounted in for the model, and it leads to a distinguishing dip in R^{--} below the critical edge, as shown in the inset of Fig. 3.12(a). Magnetic profiles used to fit the data measured at T = 4 K and 300 K are shown in Fig. 3.12(d). The magnetic profiles were assumed to be spatially symmetric with respect to the central "mirror plane" of the graded structure, with the Co magnetization and the magnetizations of 4 intermediate $Co_{1-x}Cr_x$ profile values being utilized as free parameters, specifically the ones for the profile segments with x = 0.04, x = 0.12, x = 0.20, and x = 0.28. The magnetizations of the intermediate x = 0.08, x = 0.16, and x = 0.24 layers were constrained to be the average of the neighboring layer magnetizations to limit the number of free model parameters. As expected, the profiles show little change in the outer Co layers between T = 4 K and 300 K, and a progressively larger difference with increasing x down to the central $Co_{0.72}Cr_{0.28}$ layer, which exhibits the strongest reduction in magnitude

[6] The ρ_N profile has been multiplied by a single scaling factor to account for variations in density due to alloying. This is a small effect, as the fitted value of the scaling factor is 1.03.

upon T increase. The fits corresponding to the profiles displayed in panels (c,d) are exactly the ones shown as solid lines in panels (a,b). The fact that such a restricted model fits the data so well, even the low Q_z feature corresponding to the imaginary ρ_N of Co, indicates the appropriateness of the model, which in turn corroborates that the intended compositional and magnetization depth structure was indeed achieved.

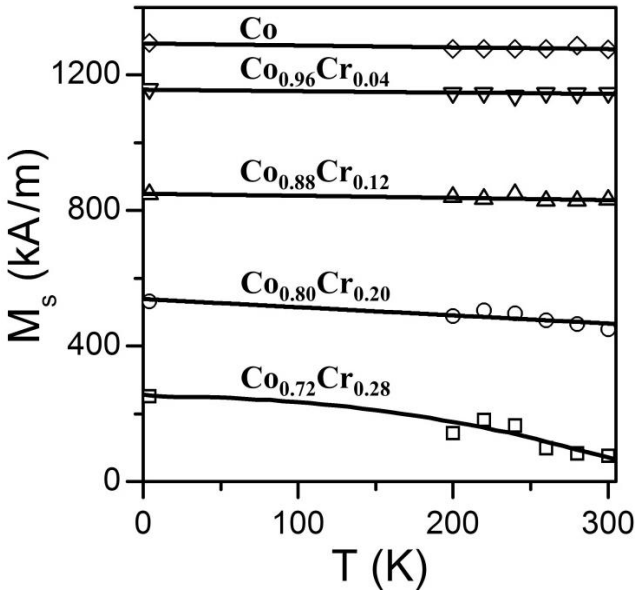

Figure 3.13: Temperature dependence of the saturation magnetization for layers in the bathtub structure as determined from PNR for the sample with Cr concentration x_c = 0.28. Solid curves are guides to the eyes. The open symbols include the errors bars corresponding to ± 1 standard deviation.

The depth distribution of the effective magnetizations is illustrated in Fig. 3.13, where the temperature dependent remanent magnetic profiles are summarized for the $Co_{1-x}Cr_x$ sublayers of the x_c = 0.28 sample. For Co and $Co_{1-x}Cr_x$ up to x = 0.12, the magnetization is basically temperature independent over the measured range. However, the x = 0.20 layer shows significant deviations at T = 200 K and above, while the x_c = 0.28 curve falls off dramatically upon increasing T. These measurements demonstrate that the effective Curie temperature is indeed changing throughout the bathtub structure, with the outermost layers having the highest inherent ordering temperature, while the lowest effective T_C, close to room temperature, is located in the center of the sample. This result corroborates the physical picture suggested by the magnetometry study that revealed a transition from a square hysteresis loop one-step reversal at low temperatures to a two-step reversal just below T = 300 K.

In order to investigate temperature dependent changes in the reversal behavior, field dependent PNR measurements were conducted at several temperatures. At each temperature studied, the sample was first negatively saturated in an applied field $\mu_0 H = -700$ mT, and subsequently PNR spectra were measured at several positive fields near the switching of the magnetization. Typically, specular PNR is modeled under the assumption that the measured signal is *coherent* - i.e. the spatial extent of in-plane features is small enough that the reflectivity corresponds to a single average in-plane sample structure.

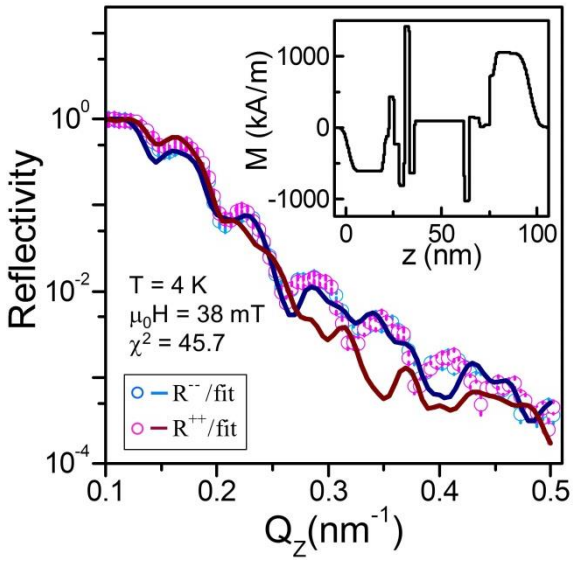

Figure 3.14: PNR data measured at T = 4 K in $\mu_0 H$ = 38 mT following prior saturation in a $\mu_0 H$ = -700 mT for the sample with Cr concentration x_c = 0.28. Solid lines are best fits corresponding to a model assuming coherent scattering from a single magnetic depth profile (shown inset). Error bars correspond to ± 1 standard deviation.

However, very close to the switching of the magnetization, it has been found that the data could not be modeled in this way. As shown in Figure 3.14, there is very little difference between the non spin-flip reflectivities R^{--} and R^{++}, which within the coherent limit would suggest that the in-plane magnetization along H has dropped to zero. However, attempting to model these data with the known nuclear model from Fig. 3.12 and zero magnetization results in a grossly incorrect fit. Even treating each layer magnetization as a free parameter, it results in the unacceptably poor fit to the data that is shown in Fig. 3.14, which corresponds to the implausible magnetic profile shown in the inset. Non-specular scans taken at several values of Q_z gave no evidence of increased diffuse scattering that might invalidate the implicit assumption of specular scattering. Since the nuclear model determined from the remanent scans cannot change as a function of H, the possibility of

magnetic domains has been considered, which are large enough for the measured signal to be *incoherent*, which means that reflectivities corresponding to distinct depth profiles are measured simultaneously. This type of modeling is challenging, as without significant constraints on the individual domain profiles, the number of free parameters can become prohibitively large, rendering the results meaningless.

Thus, an extremely restrictive model was utilized based on information already determined from the previously discussed temperature-dependent remanent scans. The nuclear profile is fixed, as are the temperature-dependent magnetizations of the individual layers. The data are then modeled as an incoherent addition of reflectivities from only three domains, parallel positive (+), antiparallel (AP), and parallel negative (-). In doing so, the only free parameters are the relative fractional populations of the three domains[7]. Since the sum of these populations must add up to one, this corresponds to only two free parameters per field condition. Fig. 3.15(a) shows the magnetization depth profiles at T = 4 K for the three domain types, that are being used to fit all field-dependent reflectivities measured at the same temperature, of which some are shown in Figs. 3.15(b-d). Following negative saturation, at $\mu_0 H$ = 2 mT the non spin-flip scattering (Fig. 3.15(b)) is almost exactly spin transposed with respect to the scattering observed at $\mu_0 H$ = 1 mT following positive saturation (Fig. 3.12(a)), i.e. R^{--} now looks like R^{++} and vice versa. This implies that the sample is uniformly negatively magnetized. This conclusion is borne out by the model fitting, which indicates 99% of the domains are in the negatively magnetized state, and results in a good fit to the data. As the field is increased to $\mu_0 H$ = 38 mT (Fig. 3.15(c)), we encounter the near-coercivity state whose reflectivity could not be fit with a coherent model (Fig. 3.14). However, the incoherent modeling approach leads to an excellent fit to the data, which allows one to deduct a nearly even population of positive and negative domains. Notably, there is no antiparallel domain population at this condition. As the field is increased to $\mu_0 H = 41$ mT (Fig. 3.15(d)), the non spin-flip reflectivities reverse with respect to Fig. 3.15(b), and the data are consistent with an essentially uniform positive magnetization. The magnetization depth profiles at T = 298 K are shown in Fig. 3.15(e) for the 3 possible domain states, with corresponding reversal data shown in panels Figs.

[7] The maximum reflectivity and a small constant angular offset are also treated as free parameters to account for variations in alignment from scan-to-scan

3.15(f-h). Again, the $\mu_0 H = 2\,mT$ data (Fig. 3.15(f)) are fit well by a uniformly negative magnetized sample. At $\mu_0 H = 21\,mT$ (Fig. 3.15(g)), near the coercive field, the reversal mechanism is different than observed at low temperature, as the antiparallel state dominates the population. At $\mu_0 H = 25\,mT$ (Fig. 3.15(h)), the sample has returned to the positively saturated state.

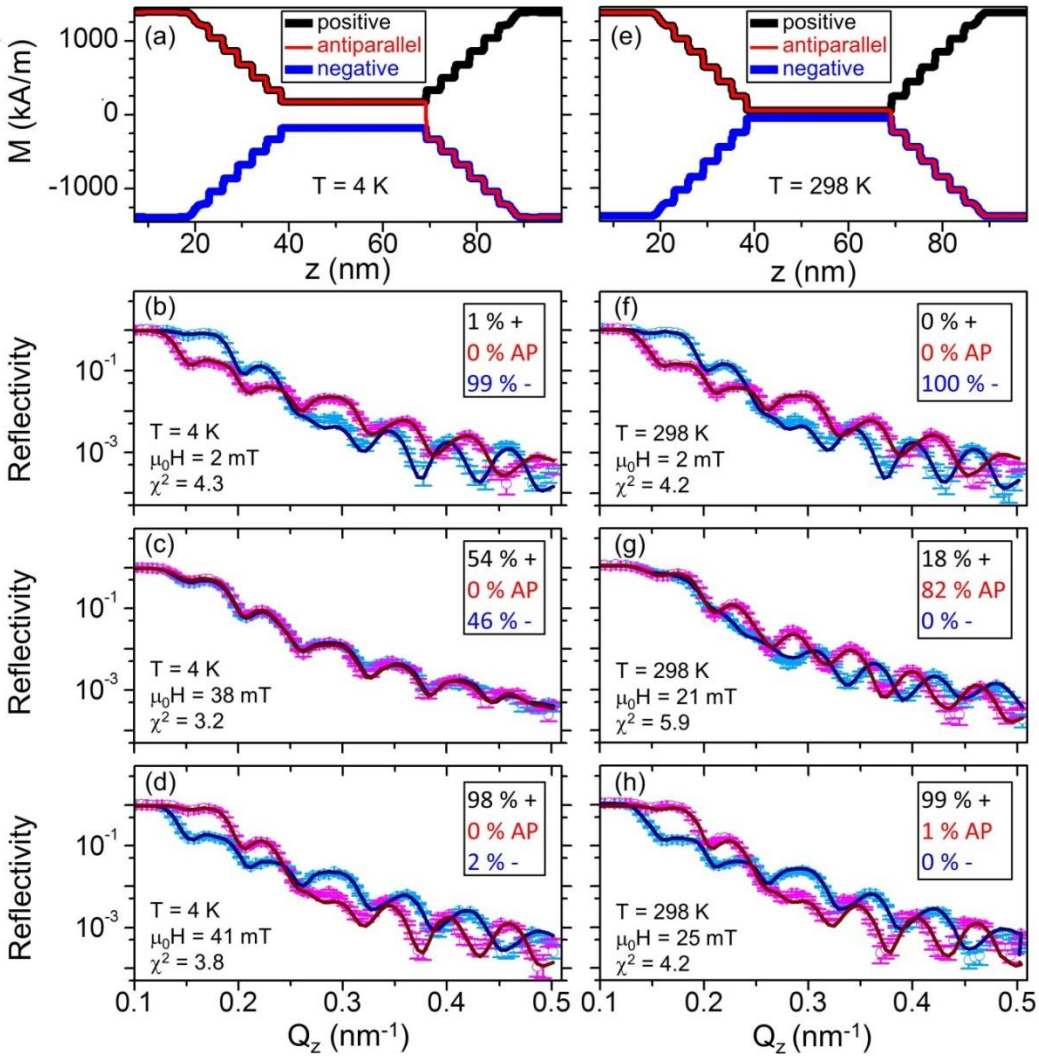

Figure 3.15: Summary of incoherent model used to fit PNR data measured for the sample with Cr concentration x_c = 0.28 at T = 4 K and T = 298 K in increasing positive field following saturation in $\mu_0 H$ = -700 mT. (a) Three magnetic domains considered for the 4 K model. (b-d) Fitted T = 4 K PNR data measured in $\mu_0 H$ = 2 mT, 38 mT, and 41 mT. (e) Domains considered for the T = 298 K magnetic model. (f-h) Fitted PNR data measured at T = 298 K in $\mu_0 H$ = 2 mT, 21 mT, and 25 mT. Error bars correspond to ± 1 standard deviation.

The overall magnetization reversal results of the PNR measurements are summarized in Figs. 3.16(a-d), which show the field-dependent domain populations at several temperatures. While all four temperatures exhibit multi-domain states near the reversal, the

antiparallel domain becomes more prominent as the temperature is increased. Thus, it has been unambiguously demonstrated that the x_c = 0.28 graded sample features completely coupled reversal throughout the entire layer thickness at T = 4 K, while domains that exhibit independent reversal of the top and bottom of the bathtub structure progressively occur as the temperature approaches the effective local Curie temperature of the central layer. It is worth mentioning that in the PNR experiments only very weak spin-flip scattering is detected. This implies that the magnetization stays essentially collinear with the magnetic field along the easy axis throughout the reversal process. This is in agreement with the quantitative model.

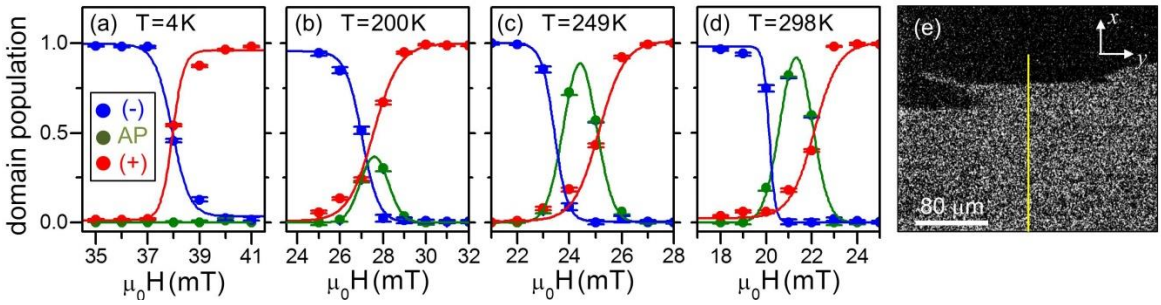

Figure 3.16: (a-d) field dependent domain populations as determined from the incoherent scattering model of the PNR data. Error bars correspond to ± 2 standard deviations. (e) room temperature MOKE microscopy image taken during reversal along the easy axis. The yellow bar represents the average projection of the neutron coherence length for the PNR measurements.

Another important question is whether or not it is plausible to have magnetic domains large enough to justify the choice of an incoherent scattering model. For this, the neutron beam is considered in terms of wave packets with coherent extent Δr perpendicular the direction of propagation, a quantity known to be of the order of 1 µm for the PBR beamline [107]. The *y*-direction has been defined to be the in-plane sample direction parallel to *H*, and *x* to be the in-plane sample direction perpendicular to *H*. In order for domains in the *x*-*y* plane of the sample to produce incoherent scattering, the spatial extent of those domains must be larger than L_x and L_y, i.e. the projections of Δr onto the sample surface. In this scattering geometry, *H* is applied perpendicular to the neutron propagation direction, so that L_y is exactly equal to Δr. Along the *x*-direction, neutrons are incident on the sample at a small angle with respect to the sample surface, stretching out L_x. Assuming Δr is 1 µm (a reasonable assumption based on Ref. 107), the scattering geometry leads to L_y = 1 µm, and L_x that varies from 265 µm at Q_z = 0.1 nm^{-1} to 53 µm at Q_z = 0.5 nm^{-1}. To

confirm whether such large domains emerge during the reversal, room temperature MOKE microscopy has been performed on the same sample, on which the PNR measurements were performed by recording videos of the magnetic domains at a frame rate of 24 s^{-1} while ramping the magnetic field in the *y* direction as a rate of approximately 0.5 mT/s. Fig. 3.16(e) shows a high contrast MOKE image of the sample during the reversal process with bright contrast indicating a magnetization in the negative *y* direction, and the dark contrast indicating a magnetization in the positive *y* direction. The image was obtained with an applied field $\mu_0 H = 20.3$ mT. The thin yellow line corresponds to the average L_x by L_y illumination area for the entire Q_z range of the PNR experiment. The image clearly indicates that the magnetic domains in the samples are large enough to engulf the entirety of the projection of a neutron wave packet on the sample surface. An incoherent model is therefore appropriate for describing the experimental PNR data. A more comprehensive model could incorporate the Q_z-dependence of L_x but such a model would add little to the evaluation of the reversal behavior of this system.

Considering the PNR results of the magnetization reversal process, there appears to be an inconsistency in between the one-step reversal behavior deduced from low temperature magnetometry data and the *incoherent* model introduced to analyze the PNR measurements, which requires the assumption of lateral domains. However, experimental details have to be considered to make this direct comparison. For the neutron characterization, 1 cm × 1 cm square samples have been employed in order to achieve an optimal balance between data acquisition time and accessible Q_z range. On the other hand, in order to fit in between the pole pieces of the VSM electromagnet, a smaller 4 mm × 4 mm square sample segment had to be used. Furthermore, in both the VSM and the PNR setups, the static magnetic field generated by the magnets, and designed to be maximized and homogeneous at the exact center in between the poles, is not truly uniform for an extended sample. Therefore, a larger sample area introduces two superimposed and thus accumulative effects: a larger absolute inhomogeneity of the sample properties as well as larger variations of the external magnetic field throughout the sample volume. Therefore, the probability of creating lateral domain structures during the magnetization reversal increases most significantly with the sample size, which is the case for the PNR experiments in contrast to the VSM magnetometry data. Also, it has to be mentioned that

the field range, in which these domain states exist is very narrow even in the case of the PNR measurements. Thus, the consistency of the experimental observations is not compromised by this minor sample size dependent effect.

3.6. Conclusions

In summary, epitaxial Co/$Co_{1-x}Cr_x$/Co films with a compositional gradient of x that follows a bathtub like shape have been successfully fabricated by means of sputter deposition. The epitaxial sample structure and in-plane uniaxial anisotropy were verified and the volume-averaged anisotropy constants measured. All the samples show simple magnetic behavior, mimicking a perfect textbook macrospin model, which allows for the study of compositional profile induced effects in great details. The sample set revealed a temperature and composition dependent magnetization reversal process. A fully correlated magnetic structure with one-step switching behavior was observed for temperatures below the effective Curie temperature of the central layer, whereas two-step switching was observed above this temperature. Specifically, $x_c \leq 0.25$ samples exhibit one-step switching for all temperatures measured, $x_c \geq 0.30$ show two-step switching for all temperatures measured, and $0.25 \leq x_c \leq 0.30$ samples have a temperature-dependent transition between one-step and two-step switching The $x_c = 0.28$ sample shows this transition at about 260 K, which is related to the magnetic ordering of the central $Co_{0.72}Cr_{0.28}$ layer at that temperature. A detailed physical picture has been developed to explain the sample behavior and it has been tested quantitatively against the experimental results. Polarized neutron-scattering measurements confirmed the graded composition and effective Curie temperature depth profile. Moreover, due to the designed symmetrically graded structure, the PNR experiments confirm the possibility to continuously shift the corresponding magnetization profiles towards or away from each other in the sample center, which in turn allows the temperature dependent tunable correlation or decorrelation of the magnetic state and the magnetic reversal behavior. The neutron characterization corroborates the physical picture based on the magnetometry data, revealing that the intermediate state of the two-step reversal is indeed a state in which the top and bottom magnetizations are anti-parallel aligned. The results demonstrate the ability to design ferromagnetic systems that can be tuned from a collective to an individual reversal behavior, with the temperature being able

to tune this correlation in a well-defined and pre-designed manner. Practically, the findings prove that the operation point of a magnetic layer system can be switched via temperature (or possibly by other stimuli) from collective to localized behavior, which should be interesting for tunable device technology in magnetic storage or spin-wave based devices.

4. Magnetization reversal in thin films with perpendicular magnetic anisotropy

The magnetization reversal process of magnetic thin films with perpendicular magnetic anisotropy (PMA) exhibits two characteristic reversal mechanisms: instability of the uniform magnetic state and domain nucleation. This chapter presents a thorough experimental and theoretical study of the corresponding magnetic phase diagram, which has revealed the coexistence of three different magnetic phases in a single point that is tricritical in nature.

4.1. Introduction

Magnetic thin films with perpendicular magnetic anisotropy (PMA) are an important research subject in the field of ferromagnetism. Interestingly, this is traditionally not related to their relevance in applications, such as hard disk drive technology, where PMA films have had a crucial importance for technological progress during the last decades [108,109]. Instead, the prominence of PMA films as research subject is related to the fact that in these systems, magneto-crystalline anisotropy and magnetostatic self-interaction (Section 1.1.2) are opposing each other. This causes the occurrence of non-uniform microscopic magnetization states as a pathway to minimize the total energy, even in materials such as the stereotypical elemental ferromagnets Fe, Co, and Ni, which otherwise have a simple ferromagnetic ground state [110-113]. These magnetic systems have been an excellent testing ground for thermodynamics and specifically for the physics of phase transitions and phase diagrams. Although in general, magnetostatic interactions are removed from the physics of ferromagnetic phase transitions by using demagnetizing factor corrections, thin films with perpendicular anisotropy belong to the group of very few magnetic systems, in which the complete phase diagram can be explored, including the exact effects of magnetostatic energy. Therefore, PMA thin films are a fundamental area of study where the understanding of ferromagnetism and phases can be investigated in great detail, making them a crucially important test object for the rigorous description of magnetic phases towards a complete understanding of ferromagnetism.

As already mentioned in Section 1.1.3, in their landmark work Landau and Liftshitz developed domain theory, conceptually introduced by Weiss in 1906, for the purpose of quantitatively describing and predicting the occurrence of non-uniform magnetic regions in ferromagnetic crystals [9]. In the 1940s, Kittel achieved the first complete description of the magnetostatic energy for a non-uniform magnetization state in a macroscopic ferromagnet by investigating magnetic films with PMA [6,114]. This solution was later extended by Kooy and Enz [115] to the case in which the sample thickness was comparable to the domain size, enabling the first quantitatively accurate description of non-uniform magnetization reversal based upon a microscopic theory [115]. Subsequently, Muller and Brown derived independently from each other the first exact analytic solutions of non-uniform magnetization states in macroscopic ferromagnets [116]. In the 1980s and

1990s, PMA films have been instrumental for the experimental discovery and exploration of surface and interface anisotropy, as well as the thickness and temperature dependent reorientation transitions [117-132], hereby addressing fundamental questions about the stability of ferromagnetism in 2-dimensional systems, spin-wave instabilities, and the energetics of domain states in ultrathin films [133-137].

All this work has led to an apparently very complete understanding of thin magnetic films with PMA, their micromagnetic states and magnetization reversal. The majority of these studies, though, either utilize an in-plane (IP) or out-of-plane (OP) orientation of the applied magnetic field, but not any intermediate field angles [138-143], since only minor domain structure differences are observed in remanence after applying different field orientations [138]. As a result, thin film PMA ferromagnets such as Co were assumed to exhibit rather simple H-δ phase diagrams, with δ being the angle between the in-plane orientation and the direction of the magnetic field, shown in Fig. 4.1(a). This is however surprising because the magnetization reversal processes for in-plane and out-of-plane applied fields are qualitatively very different. Indeed, once H is applied along the surface normal, δ = 90° (Fig. 4.1(b)), magnetization reversal occurs as a first order phase transition via nucleation, whereas processes consistent with a second order phase transition are observable in the in-plane field orientation, δ = 0° (Fig. 4.1(c)).

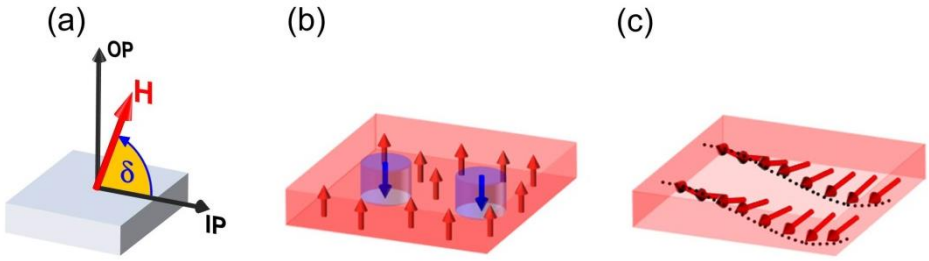

Figure 4.1: (a) displays the direction of the external magnetic field *H* with respect to the sample surface, which defines the angle δ. (b) displays a schematic of the domain nucleation reversal process occurring for δ = 90°. (c) shows a schematic of the soft spin-wave mode occurring for low δ = 0.

For pure Co-films, it was recently shown that the two regimes can cross at a certain intermediate δ value, and given the different order of the two phase transitions from a uniform to a non-uniform magnetic state, the crossing point was interpreted as a *tricritical point* [144]. As described in Section 1.1.2, magnetocrystalline anisotropy is an important energy term that controls the preferential orientation of the magnetization in materials, as

well as the specifics of resulting micromagnetic states via the competition with the magnetostatic energy. In general, the magnetocrystalline anisotropy depends on the materials composition and crystal structure [95,145-147]. Moreover, it exhibits a significant temperature dependence, which turns out to be very strong for Co just above room temperature (RT). This is in stark contrast to the saturation magnetization and thus to the magnetostatic energy, which is nearly independent of temperature in this regime [97,148]. This makes Co an attractive material to explore the magnetization reversal and the phase space of PMA films as the energy balance is changed in between magnetocrystalline anisotropy energy, characterized by its constant K, and the magnetostatic energy, which is proportional to $(M_S)^2$. This can be easily and very efficiently achieved by varying the temperature for PMA Co-films. Alternatively, a tuning of the energy balance can be obtained by alloying Co-based films with different materials [94-96,99,149-152]. Following the detailed discussion of prior knowledge of PMA films, the purpose of this chapter is to provide a complete exploration and description of the magnetization reversal of PMA films as a function of the energy balance in between magnetostatic and anisotropy energies and to verify the existence of the tricritical point in the H-δ phase diagram. Consequently, this chapter presents a detailed study of the structural, magnetic and magnetization reversal properties of epitaxial Co and $Co_{90}Ru_{10}$ thin films grown with (0001) crystallographic orientation, together with a comparison to the micromagnetic modelling performed by Prof. Dr. Ondrej Hovorka to address the above questions and goals.

4.2. Fabrication process

Co and $Co_{90}Ru_{10}$ (0001) oriented films of 200 nm thickness were prepared by DC magnetron sputter and co-sputter deposition. Si (111) substrates were cleaned following the same procedure described in Section 3.2. As a template for the growth of high quality epitaxial (0001) *hcp*-Co and *hcp*-$Co_{90}Ru_{10}$ films, a sequence of 12 nm Ag, 30 nm Ti and 20 nm Ru was deposited at room temperature. Thereafter, the Co or $Co_{90}Ru_{10}$ deposition was performed at T = 573 K, after this temperature was reached (Fig. 4.2(a)), followed by a thermal annealing at the same temperature for 30 min (Fig. 4.2(b)) in order to achieve an

improved *c*-axis alignment and correspondingly more uniform magnetic properties [149,153].

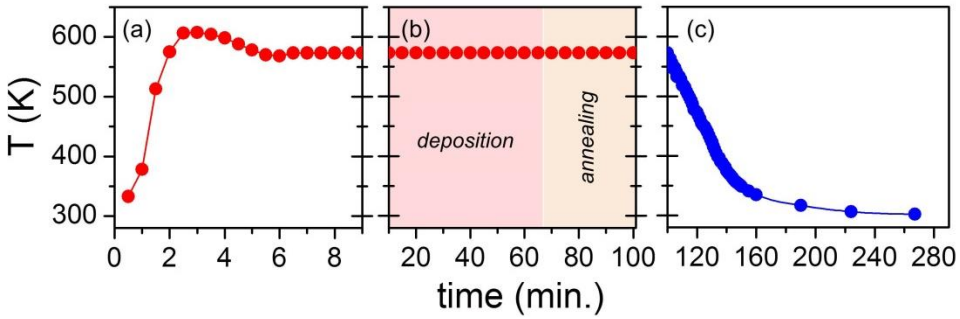

Figure 4.2: (a-c) sample temperature vs. time sequence during the sputter deposition of a 200 nm thick Co layer.

The subsequent cooling process of the completed magnetic samples has been carefully carried out at an initial rate of 5 K/min down to RT to avoid the formation of the *fcc* phase of Co or CoRu, as shown in Fig. 4.2(c). Each sample was then coated with 10 nm of amorphous SiO_2 to avoid surface oxidation and contamination after removal from the vacuum system.

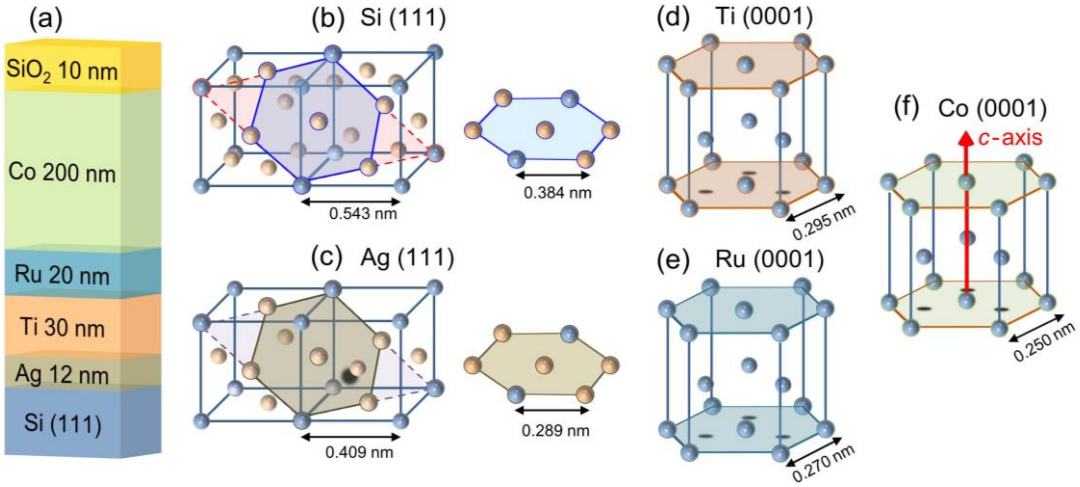

Figure 4.3: (a) schematic of the heteroepitaxial growth sequence for the sample type studied here, including relative thicknesses; (b) single crystal orientation of the Si substrate; crystal planes induced during the growth process with respect to the corresponding unit cells for the Ag (c), Ti (d), Ru (e) and Co (f) layers. The lattice dimensions refer to bulk parameters.

A schematic of such a sample, including its specific layer sequence, is shown in Fig. 4.3(a) together with the unit cell of the silicon substrate (Fig. 4.3(b)), *fcc*-silver (Fig. 4.3(c)), *hcp*-titanium (Fig. 4.3(d)), *hcp*-ruthenium (Fig. 4.3(e)) and *hcp*-cobalt (Fig. 4.3(f)) with the *c*-axis orientation along the surface normal.

4.3. Structural characterization

In order to characterize the crystallographic structure of each layer and to measure the out-of-plane crystalline grain dispersion, conventional XRD θ-2θ scans and rocking curve measurements were performed. In addition, the in-plane epitaxial relationships between the substrate and the epitaxial layers were studied by means of XRD φ-scans at specific crystallographic poles. Fig. 4.4 illustrates XRD θ-2θ scans in the angular range from 27° to 47° (a) and from 76° to 104° (b). In (a), the measurement shows four clearly separated Bragg diffraction peaks. They correspond to the Si (111) substrate, Ru (0002) and *hcp*-Co (0002) lattice planes, whereas the slightly broader peak that appears at 2θ ≈ 38.3° is the result of the overlapped signals coming from the Ag (111) and Ti (0002) diffraction planes.

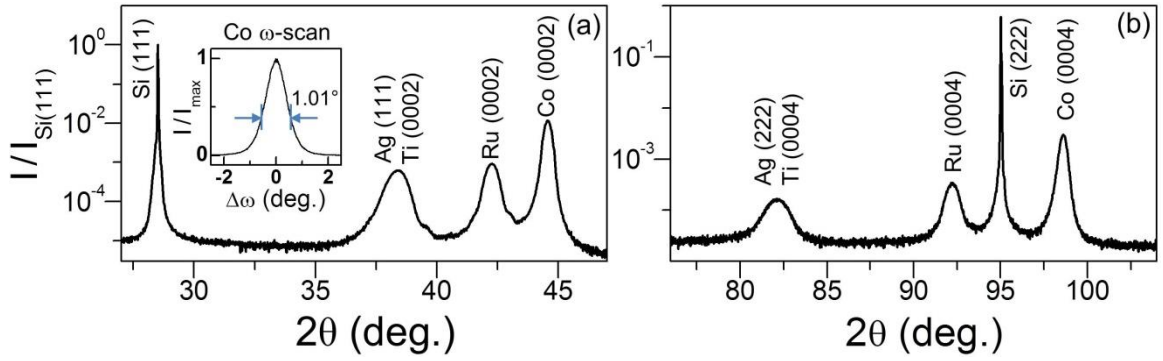

Figure 4.4: (a-b) XRD θ-2θ scans of a 200 nm thick Co sample. The inset in (a) shows a rocking curve measurement for the Co (0002) diffraction peak.

For larger scattering angles, shown in (b), four interference peaks are observed at the positions of Ru (0004), Si (222) and *hcp*-Co (0004) scattering angles and at 2θ ≈ 82.1°. Again, this somewhat broadened peak originates from a superposition of the Ag (222) and Ti (0004) Bragg peaks. Beside the substrate peaks, the total angular range shows only well-defined *fcc* (*nnn*) and *hcp* (000*l*) peaks, without the appearance of any other Bragg reflection. Thus, the structural sample analysis verifies the high crystallographic quality of the optimized layer growth sequence resulting in well-ordered *hcp* Co films with perpendicular *c*-axis orientation that is necessary for a preferential out-of-plane orientation of the magnetization, given that the *c*-axis is the easy axis of magnetization for Co. To verify the narrow *c*-axis dispersion in the samples, rocking curve measurements have been performed for the Co (0002) peak (inset in Fig. 4.4(a)). The full width at half maximum value of the peak is $1.01° \pm 0.01°$, indicating that the Co films achieve excellent alignment

of the *c*-axis orientation normal to the sample surface, if compared to previous works [109,144,154-157].

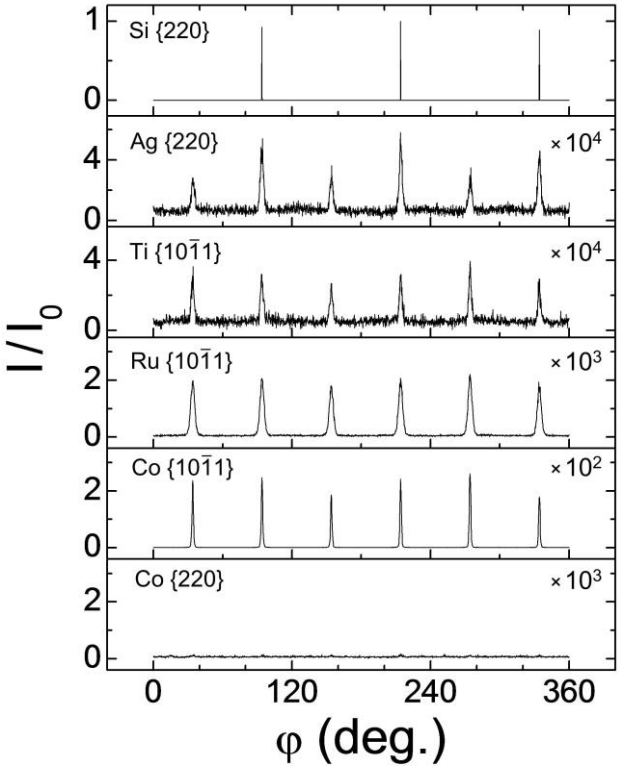

Figure 4.5: XRD φ-scans measured for an epitaxial 200 nm thick Co-film at the Si {220}, Ag {220}, Ti {10$\bar{1}$1}, Ru {10$\bar{1}$1}, Co {10$\bar{1}$1} and Co {220} poles.

In order to confirm the in-plane epitaxial alignment of the different layers in the growth sequence, XRD φ-scan measurements were carried out and are shown in Fig. 4.5. As expected from the stereographic projection, three diffraction peaks separated by 120° were measured in the Si {220} pole scan while six evenly spaced peaks were observed from the Ag {220}, which indicates the existence of twinned orientations for the Ag grains [158]. Ti, Ru and Co, at their respective {10$\bar{1}$1} poles, all show six diffraction peaks, in agreement with the stereographic projection of a single crystal *hcp* (0001) surface orientation. Also, the Ti-, Ru-, and Co-peaks appear at the correct angles with respect to the Si-substrate, thus verifying the epitaxial nature of the samples. Moreover, in order to corroborate the pure *hcp* crystal nature of the Co thin films, φ-scan measurements at the *fcc*-Co {220} pole have been performed. In the entire angular range, no presence of *fcc*-Co could be detected, as indicated by the complete absence of any constructive diffraction peak. Using the background intensity of this measurement to quantify an upper limit of possible *fcc*

concentration in these Co-films, their volume contribution has been determined to be less than 0.26% of the total Co-film.

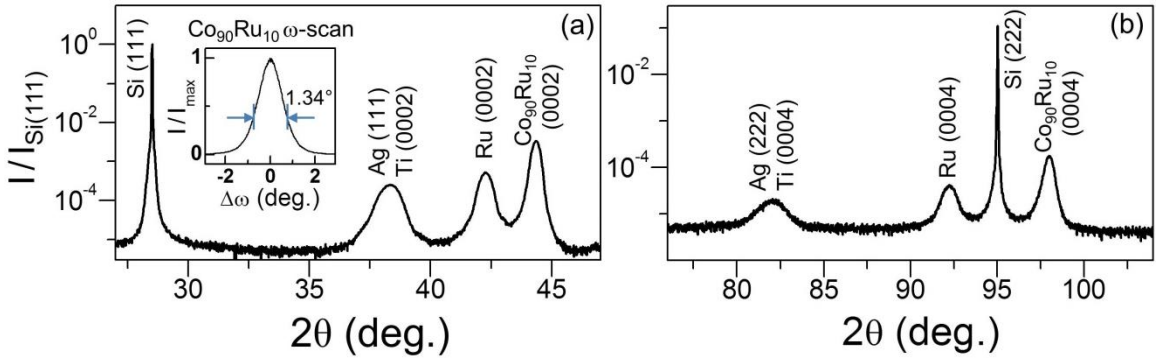

Figure 4.6: (a,b) XRD θ-2θ scan of the 200 nm thick $Co_{90}Ru_{10}$ sample. The inset in (a) shows a rocking curve measurement for the $Co_{90}Ru_{10}$ (0002) diffraction peak.

The structural characterization of the 200 nm $Co_{90}Ru_{10}$ films has also been performed via θ-2θ scans in the $27° \leq 2\theta \leq 104°$ angular range, as shown in Figs. 4.6(a,b). Together with the reference substrate peaks and the overlapping Ag- and Ti-peaks, well-defined *hcp*-Ru, and *hcp*-$Co_{90}Ru_{10}$ (0002) and (0004) peaks have been measured that exhibit nearly identical widths if compared to the pattern of the pure-cobalt sample, without the appearance of any other crystallographic diffraction peak. The *hcp*-$Co_{90}Ru_{10}$ (0002) peak position at $2\theta = 44.33°$ is shifted by 0.23° towards lower diffraction angles in comparison to the measured *hcp*-Co (0002) peak position, which is observed at $2\theta = 44.56°$. This peak shift, in the absence of significant broadening, verifies the simple Co substitution by Ru, corresponding to an increase of the lattice constants by introducing Ru into the hexagonal close packed lattice. Rocking curve measurements for the $Co_{90}Ru_{10}$ (0002) peak reveal a full width at half maximum of $1.34° \pm 0.01°$, slightly larger than that of pure Co, but still indicating the excellent *c*-axis alignment of the alloy films, especially if compared to previous findings [154-156,158]. The φ-scan measurements, shown in Fig. 4.7, revealed very good in-plane epitaxial relationships between the Si substrate and the metal layers, with an estimate of less than 0.51 % *fcc*-$Co_{90}Ru_{10}$ being possibly present in the films. For both sample types, the epitaxial quality and the narrow easy-axis dispersion verify the efficacy of the deposition procedure that has been utilized.

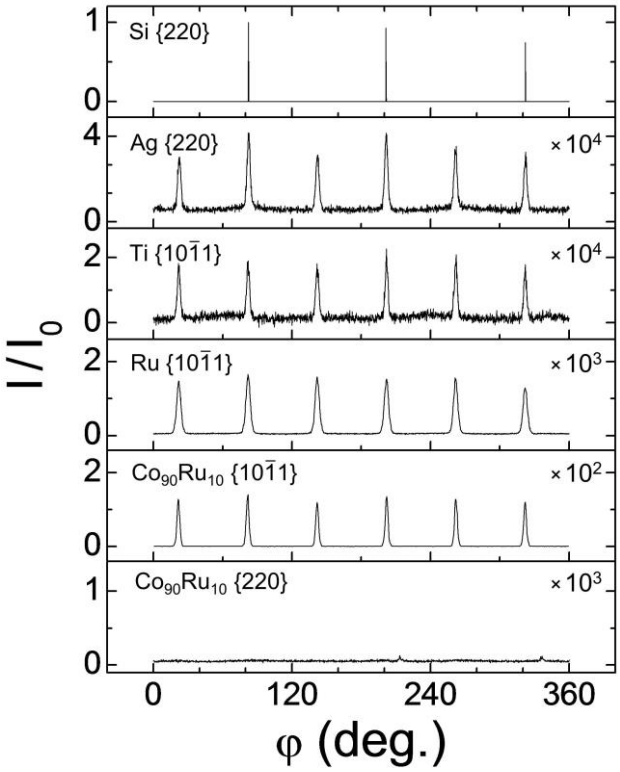

Figure 4.7: XRD φ-scans measured for an epitaxial 200 nm thick $Co_{90}Ru_{10}$-film at the Si {220}, Ag {220}, Ti {10$\bar{1}$1}, Ru {10$\bar{1}$1}, $Co_{90}Ru_{10}$ {10$\bar{1}$1} and $Co_{90}Ru_{10}$ {220} poles.

4.4. Room temperature magnetic characterization

Fig. 4.8 presents the room temperature magnetic characterization of a 200 nm thick Co (0001) sample. The left part shows the magnetization curves $M(H)$ measured for an external magnetic field applied perpendicular, Fig. 4.8(a), and parallel to the film plane, Fig. 4.8(b). The two curves, well documented in literature [137-141], are almost identical in the high field regime, for $\mu_0 H > \mu_0 H_s \approx \pm 1.5\,\mathrm{T}$, where the system exhibits a uniform magnetization state parallel to the direction of the applied magnetic field. In the OP configuration, once the field is lowered, the uniform state is altered by the formation of bubble-like domains with opposite magnetization orientation in order to minimize the total magnetostatic energy, as shown by the schematic in Fig. 4.1(b). This process starts rather abruptly at the nucleation field $\mu_0 H_n \approx 1.3\,\mathrm{T}$, leading to a drop in the magnetization. As the field is further reduced, the nucleation domain density increases and their dimensions grow, resulting in the linear field dependence of the magnetization down to $\mu_0 H = 0$ T, where a small hysteresis effect is the result of sample imperfections. In the IP field geometry, Fig. 4.8(b), the saturated state becomes unstable upon reducing the field strength

and undergoes laterally alternating magnetization rotations driven by the perpendicular magnetic anisotropy, depicted in Fig. 4.1(c), which culminates in the formation of a remanent stripe domain configuration. However, even in remanence, a relevant IP magnetization persists, which was aligned during the field sequence and which is responsible for the hysteresis that occurs for low field values in this field geometry.

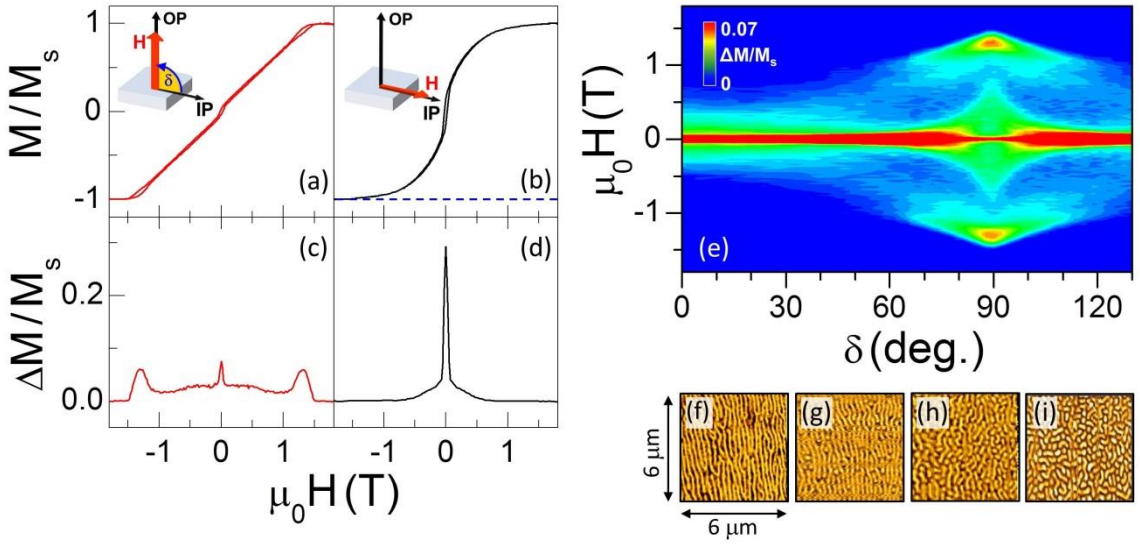

Figure 4.8: OP (a) and IP (b) hysteresis loops of a 200 nm thick Co (0001) sample measured at room temperature; the insets in (a) and (b) display the direction of H with respect to the sample surface, which defines the angle δ; $\Delta M/M_S$ data for δ = 90° (c), and for δ = 0° (d); (e) $\Delta M/M_S$ (δ, H) (color-coded) map (the signal scale is defined in the figure). (f-i) Room temperature MFM images, measured on the same Co sample, for remanent magnetic states after reducing the magnetic field from $\mu_0 H$ = 1.8 T to 0 T applied at δ = 0° (f), δ= 40° (g), δ = 80° (h) and δ = 90° (i).

Therefore, two fundamentally different magnetization processes take place. When the magnetic field is applied perpendicular to the substrate, the transition from saturated to domain state occurs as a first order phase transition, mediated by means of domain nucleation. In contrast, the uniform magnetic state becomes unstable upon lowering the magnetic field applied parallel to the sample surface, undergoing a second order phase transition.

For the purpose of analyzing these different magnetization reversal mechanisms and specifically to be able to identify them, a convenient methodology has been adopted, which was introduced in an earlier study [144]. This methodology utilizes the normalized difference in magnetization in between the two branches of $M(H)$, namely:

$$\frac{\Delta M(\delta,H)}{M_S} = \frac{M_{desc}\,(\delta,H) - M_{asc}\,(\delta,H)}{M_S} \tag{4.1}$$

here $M_{desc}(\delta,H)$ and $M_{asc}(\delta,H)$ represent the descending and ascending branches of the magnetization curve for a given magnetic field strength H and angle δ. Fig. 4.8(c) shows the $\Delta M/M_S$ values vs. H for the OP orientation of the applied magnetic field. Here, the small and narrow peak centered at $\mu_0 H = 0$ T corresponds to the low field hysteresis, whereas the two well pronounced peaks at $\mu_0 H \approx \pm 1.3$ T represent the domain nucleation hysteresis. For the IP case shown in Fig. 4.8(d), only one sharp peak at $\mu_0 H = 0$ T is present, associated with the hysteretic switching of the remanent in-plane magnetization component at low fields. Here, the high field instability driven magnetic phase transition does not appear because it is a second order phase transition and thus does not exhibit any hysteresis.

In order to investigate the magnetization reversal process in the entire field angle range, $M(H)$ curves have been measured for different applied field orientations δ in between δ = 0° and δ = 130°, in steps of 5° for δ = 0º - 70º, and in steps of 2° in between δ = 70° and δ = 130°. The complete angular dependence of the normalized magnetization difference is shown in Fig. 4.8(e) as a color-coded map of $\Delta M/M_S(\delta,H)$, as defined in Eq. 4.1. In this plot, the low magnetic field hysteresis forms a central band that extends from left to right over all magnetic field angles, even if it decreases in width near δ = 90º. In contrast, the domain nucleation hysteresis is visible in this plot via two high field "islands" centered at $\mu_0 H = \pm 1.3$ T and δ = 90º. Upon changing δ away from the out-of-plane orientation, the island width gradually reduces and they completely disappear for δ < 60º or δ > 120º. From the results in Fig. 4.8(e), which corroborate the earlier room temperature observations in Ref. 144, it can be deduce that, in the δ < 60º and δ > 120º regimes, the magnetic system is undergoing a second order rather than a first order phase transition. In order to confirm the anticipated dependence of the remanent magnetic states on the two different reversal behaviors, MFM measurements were performed as a function of the applied magnetic field angle. As expected, two different types of resulting domain structures have been found: stripe domains for small values of δ, Figs. 4.8(f) and 4.8(g), and isolated domains produced by nucleation processes, Figs. 4.8(h) and 4.8(i), for sufficient large δ.

In order to illustrate the origin of the anticipated H-δ phase diagram, Fig. 4.9 shows the calculated orientation dependence for the nucleation field H_n (first order phase transition) as a (blue) solid line and the critical field H_{cr}, that describes the stripe-domain instability (second order phase transition), as a (red) dashed line, reported for such a 200 nm thick Co-film in previous work [144]. As one can clearly see, H_{cr} shows only a rather weak angular dependence, being nearly constant from 0º up to about 50°, and then slightly decreasing with a minimum at δ = 90°. In contrast, the nucleation field depends strongly on δ, with a clear maximum if the field is perpendicular to the sample surface. More importantly, the nucleation field even vanishes for field orientations near δ = 30° due to the fact that the magnetostatic energy of the saturated state becomes smaller for small δ, and any domain nucleation cannot generate a sufficient energy reduction at a positive field value. The different angular dependence of these two processes produces a crossing near δ = 60° (indicated by a black circle in Fig. 4.9).

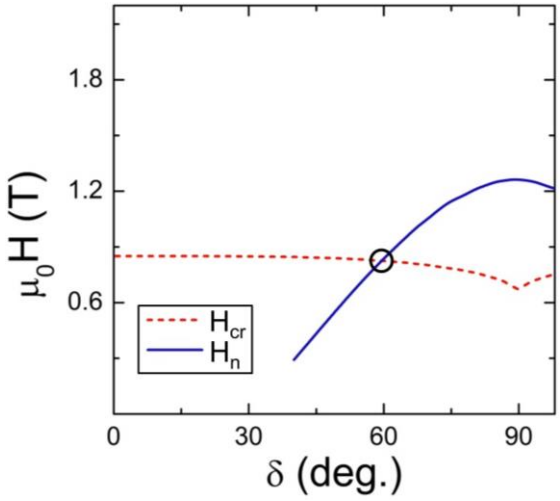

Figure 4.9: H_{cr} (δ), red dashed line, and H_n (δ), blue line curves calculated for a 200 nm thick film with a PMA field value of $\mu_0 H_k$ = 1.1 T, adapted from [144]. The crossing of H_{cr} (δ) and H_n (δ) is highlighted by a black circle.

Due to the relevance of such a fundamental change in magnetization reversal behavior, it is important to understand and study what defines and governs the existence and position of this crossing point. Therefore, it is of crucial importance to identify and adequately separate the three possible different magnetic phases to achieve an unambiguous confirmation of its presence. As already mentioned, one should keep in mind that the underlying phase transitions are both triggered by the competition between magnetostatic

energy, which tries to avoid out-of-plane magnetization orientations, and the magnetocrystalline anisotropy, which favors out-of-plane magnetization orientation in PMA films. As already described in Section 4.1, a suitable experimental starting point is the relative variation of these two energy contributions in an otherwise unaltered physical system. This can easily be done for PMA Co films, because Co exhibits a very strong temperature dependence of the magnetocrystalline anisotropy just above RT [97,148], whereas other materials properties, including the saturation magnetization and thus the magnetostatic energy vary only minimally in this temperature regime.

4.5. Temperature and composition dependent magnetic characterization

Fig. 4.10 shows $\Delta M/M_S(\delta, \mathrm{H})$ color-coded maps in the $303\,\mathrm{K} \leq \mathrm{T} \leq 563\,\mathrm{K}$ temperature range, using temperature steps of 40 K (measurements have actually been performed every 10 K). The angular and field resolutions used in these measurements are the same as for the RT measurements. As can be clearly seen, the resulting $\Delta M/M_S(\delta, \mathrm{H})$ maps strongly depend on temperature, showing significant changes especially in the high magnetic field regime. The most relevant modification involves the two islands near the out-of-plane field orientation, which are associated with domain nucleation hysteresis.

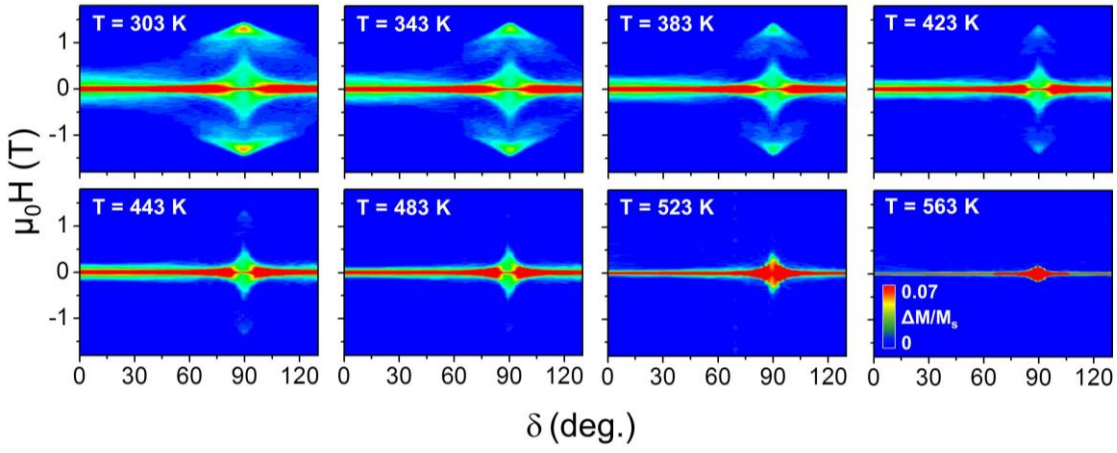

Figure 4.10: $\Delta M/M_S$ (color-coded) maps as a function of field angle δ and strength μ_0H measured for a 200 nm thick epitaxial Co (0001) film at the different temperatures that are indicated in each map. The scale (color code) is defined in the figure.

Without changing in field position, their angular extension shrinks progressively upon increasing the temperature, up to the point where they collapse entirely. In contrast to this change in the nucleation behavior, the central hysteresis band does not disappear, but

instead actually increases significantly at T = 523 K near the out-of-plane field orientation, before it decreases again for even higher T. Also, it is worth mentioning that M_S maintains a nearly constant value in the entire temperature range studied here. As discussed above, the angular extension of the nucleation islands is controlled by the intersection between the $H_{cr}(\delta)$ and $H_n(\delta)$ curves [144]. Thus, the experimental observations in Fig. 4.10 reflect the temperature-induced changes in the existence ranges of the two magnetization reversal mechanisms that are triggered by the temperature dependence of the magnetocrystalline anisotropy.

In order to visualize this dependence of the reversal mechanism at a certain angle, the same datasets were plotted as $\Delta M/M_S(\mathrm{T},\mathrm{H})$ color-coded maps for different field angles δ, displayed in Fig. 4.11 for four specific δ values. For the IP configuration, Fig. 4.11(a), a gradual reduction of the central hysteretic band with increasing temperature is visible without the appearance of any other hysteretic structure in the entire temperature range.

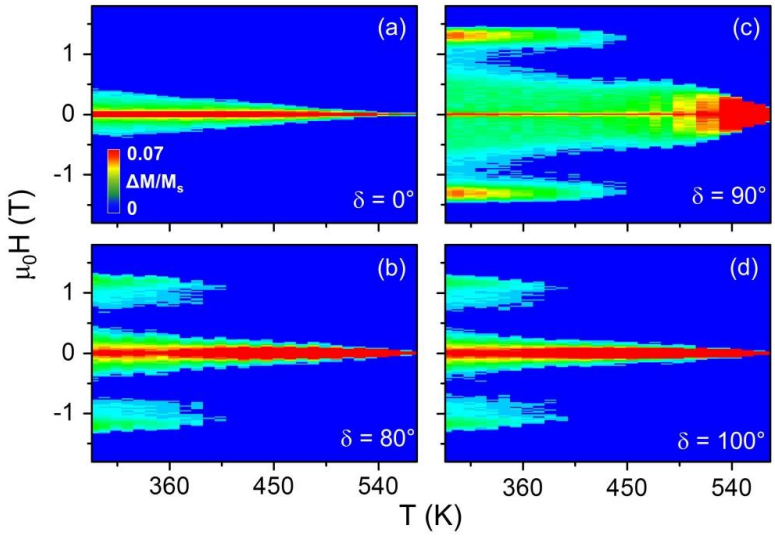

Figure 4.11: $\Delta M/M_S$ (color-coded) maps as a function of field strength μ_0H and temperature T measured for a 200 nm thick epitaxial Co (0001) film at different values δ = 0°, 80°, 90°, 100°. The scale (color code) is defined in the figure.

This behavior is fully consistent with the high field hysteresis-free phase transition of an instability induced stripe domain pattern that leads to a hysteresis peak around zero field due to the existence of a net in-plane magnetization component for this state. As the temperature increases, this in-plane magnetization reversal becomes gradually less hysteretic. For the OP geometry, Fig. 4.11(c), an increase of the temperature corresponds initially to a gradual reduction of the two high field islands, followed by their complete

disappearance at $T \approx 450$ K. Conversely, the central band stays nearly constant up to about 500 K, where it starts to expand significantly before it shrinks again at the highest temperatures used in the experiment. If the field is applied along $\delta = 80°$, Fig. 4.11(b), or $\delta = 100°$, Fig. 4.11(d), the two nucleation islands appear shifted towards lower fields with respect to the OP geometry, and more relevantly they vanish at a significantly lower temperature, namely $T \approx 400$ K, while the central hysteretic band exhibits only moderate changes in the entire temperature range. By associating the existence of high field hysteretic behavior with nucleation and the absence of it with instability-driven stripe domain generation, Fig. 4.11 reveals that the $H_n(\delta)$- and $H_{cr}(\delta)$-curves cross at $\delta = 80°$ for $T = 400$ K, while they cross at significantly smaller δ at lower temperature and not at all anymore for $T \geq 450$ K.

In order to exclude the possibility that a temperature induced reorientation transition with only an in-plane magnetization at elevated temperature is responsible for the disappearance of the nucleation reversal process, Fig. 4.12 shows a comparison between the in-plane (b) and out-of-plane (a) magnetization curves M(H) measured at $T = 493$ K for a 200 nm thick Co sample. Hereby, it is important that for the IP configuration, i.e. Fig. 4.12(b), the persistence of a strong curvature of the loop is found that exhibits only a very small remanent magnetization. Thus, the sample is evidently not in an in-plane magnetization state in remanence, meaning that it must go through a perpendicular domain generation process as one lowers the externally applied field. The absence of high-field hysteresis at $T = 493$ K independent from δ thus means that the domain instability process is occurring for all field orientations, while domain nucleation is completely absent.

While a direct confirmation of the high temperature out-of-plane remanent domain state via MFM measurements is not feasible with the available equipment, the fabricated 200 nm thick *hcp*-$Co_{90}Ru_{10}$ (0001) alloy thin film exhibits a room temperature magnetic behavior that mimics the high temperature Co-film properties very well. Figs. 4.12(c) and (d) show RT - M (H) curves for this alloy sample in direct comparison with the data for the pure Co-film measured at 493 K. As can be seen, the IP curve for the alloy film, Fig. 4.12(d), shows a small central hysteresis, a strong curvature and only a small remanent magnetic moment. The OP data for this sample, Fig. 4.12(c), also show very comparable results to the high temperature Co-film, including the absence of high field nucleation

hysteresis near saturation. The remanent magnetic domain structures connected to the two measured magnetization reversals have been investigated via MFM measurements.

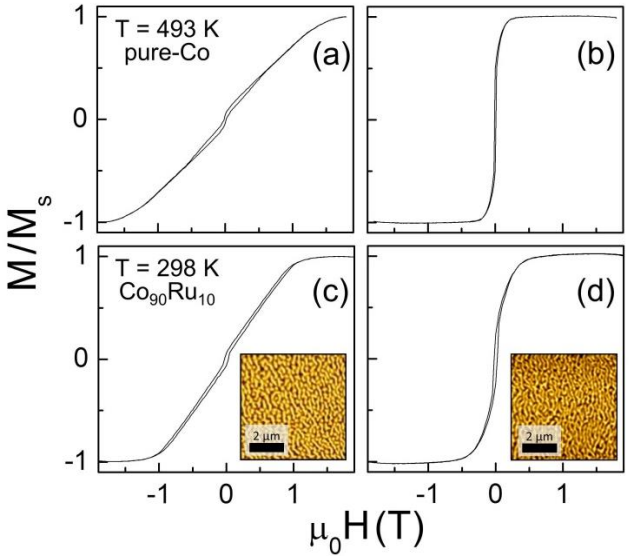

Figure 4.12: OP (a) and IP (b) hysteresis loops measured at T = 493 K for a 200 nm thick epitaxial Co (0001) film; OP (c) and IP (d) hysteresis loops measured by at room temperature for a 200 nm thick epitaxial $Co_{90}Ru_{10}$ (0001) film; the insets in (c) and (d) display room temperature MFM images measured in remanence by first reducing the magnetic field from $\mu_0 H$ = 1.8 T to 0 T at fixed angles near OP (c) and IP (d) for the same $Co_{90}Ru_{10}$ alloy sample.

First, the $Co_{90}Ru_{10}$ sample has been brought to saturation, applying an external magnetic field with a magnitude of $\mu_0 H$ = 1.8 T; then the field has been removed reducing its amplitude in steps of $\mu_0 \Delta H$ = 0.1 T down to $\mu_0 H$ = 0 T. Both images, shown as insets in Figs. 4.12(c-d), have then been recorded in the absence of any external magnetic field. Although a meager deterioration of the stripe-like pattern configuration compared to the pure Co-film case is visible, most likely attributable to the slightly worse quality of the alloy sample, both geometries show that the tendency to form stripe-like pattern is certainly not reduced upon going from in-plane, Fig. 4.12(d), to out-of-plane field orientation, Fig. 4.12(c), even if the stripe alignment force of the IP field component is vastly reduced. In addition, MFM measurements confirm that the system still develops a perpendicular stripe domain state at remanence, which can only occur if the out-of-plane orientation of the magnetization is preferred.

Utilizing this strong link between the magnetization reversal processes for pure Co at high temperature and the room temperature $Co_{90}Ru_{10}$ alloy behavior, the assumption that there is a temperature range in which Co has perpendicular stripe domains without

undergoing domain nucleation processes even for the out-of-plane field orientation has been confirmed. Moreover, this means that upon sufficiently lowering the magnetocrystalline anisotropy, an angular independent reversal process is achievable by either heating or by alloying.

4.6. Comparison to micromagnetic simulations

In order to further confirm the validity of the physical picture deduced from the experimental data, micromagnetic simulations of the field induced reversal processes have been performed by Prof. Dr. Ondrej Hovorka (see Appendix A for technical details). Here, we present the comparison of the results of these simulations to the experimental data and discuss what information can be extracted from this comparison.

In Fig. 4.13, simulated magnetization curves for $K = 5.5 \times 10^5\,\mathrm{J/m^3}$ are visualized as (black) thick solid lines, for the out-of-plane (a) and the in-plane (b) field orientations together with the respective experimental data, shown as (red) thin solid lines[8]. Exhibiting an excellent level of similarity with the experimental results, the simulations (Fig. 4.13(b)) show that the in-plane magnetization becomes unstable upon lowering the magnetic field from saturation, leading to a transition into a non-uniform magnetization state without the occurrence of any hysteresis. Only at very low field values, hysteretic behavior is observed, which is associated with the reversal of the weak remanent in-plane magnetization component. When the field is applied perpendicular to the sample surface, Fig. 4.13(a), the simulated $M(H)$ data show that the originally saturated state changes its magnetization rather suddenly at the nucleation field. In panels (c) and (d) of Fig. 4.13, the corresponding values for $\Delta M/M_S$(H) are displayed in direct comparison with the experiments. For the in-plane case, Fig. 4.13(d), only the narrow central peak of in-plane magnetization reversal near remanence is visible and its height and position are very well reproduced by the simulation. For the out-of-plane case, Fig. 4.13(c), the calculated curve exhibits hysteresis only at high fields, where the local formation and annihilation of individual up or down domains occurs.

[8] For this particular comparison, it has been assumed that the saturation magnetization is $M_S = 1448 \times 10^3$ A/m, a micromagnetic exchange coupling constant $A = 1.5 \times 10^{-11}$ J/m and a uniaxial anisotropy constant $K = 5.5 \times 10^5\,\mathrm{J/m^3}$.

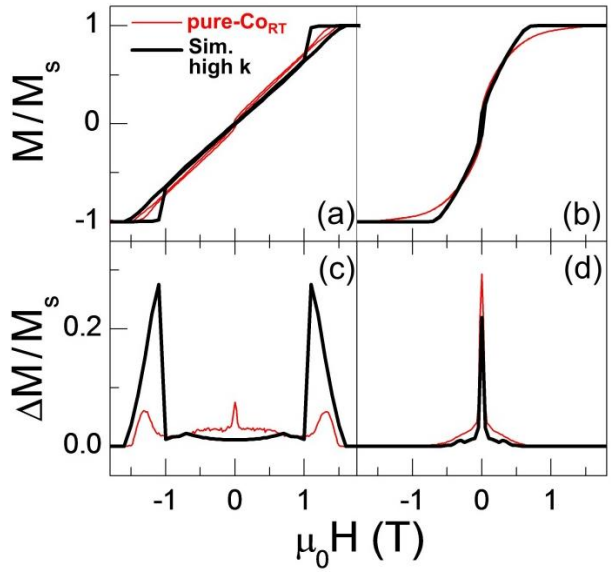

Figure 4.13: Hysteresis loops for a 200 nm thick epitaxial Co (0001) film: experimental data are shown as red lines, while simulation results are displayed as black thick lines; (a) shows the out-of-plane and (b) the in-plane behavior. The corresponding $\Delta M/M_S$ curves are shown in (c) for the out-of-plane and in (d) for the in-plane cases.

While reproducing the positions of the experimental high field peaks very accurately, the peaks resulting from the numerical simulations are enhanced with respect to the experimental case. Also, the calculations do not show the small peak at low fields, which has been found experimentally and which is associated with the limited mobility of the domain walls in the samples. These quantitative differences in both field orientations can be explained by an imperfect representation of structural disorder, e.g. defects of the crystal lattice and grain structure, as well as the lack of thermal activation, which is present only in the experimental system. Overall, however, the simulation successfully reproduces all key features, namely OP-nucleation and IP-low field hysteresis, and thus it is in very good qualitative agreement with the experimental data, hereby verifying the fundamental differences between the in-plane and out-of-plane magnetization reversal processes. In order to confirm the entire field orientation dependence, Fig. 4.14(c) shows simulated $\Delta M/M_S$ (δ, H) results for $K = 5.5 \times 10^5$ J/m^3 as color-coded map. The low magnetic field hysteresis is clearly visible at small δ, while it is absent in the proximity of $\delta = 90°$. The two high field islands, representing the domain nucleation hysteresis, are centered at $\delta = 90°$.

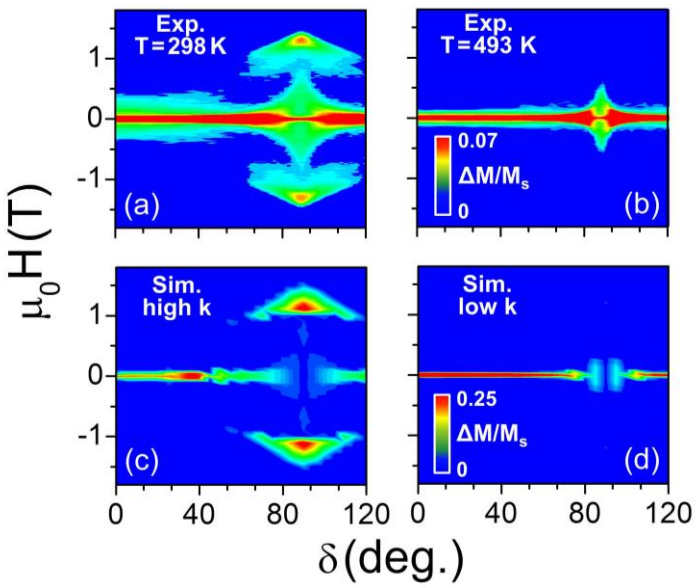

Figure 4.14: $\Delta M/M_S$ maps as a function of field angle δ and strength μ_0H measured for a 200 nm thick epitaxial Co (0001) film at T = 298 K (a) and T = 493 K (b). The corresponding color code scale is defined in (b). Calculated $\Delta M/M_S$ (δ,H) maps for a 200 nm thick Co film assuming K = 5.5 × 10^5 Jm^{-3} (c) and K = 8.0 × 10^4 Jm^{-3} (d). The color code scale for (c,d) is defined in (d).

They reduce gradually upon shifting δ away from the out-of-plane orientation, and they disappear for $\delta < 60°$. Thus, the calculated map in Fig. 4.14(c) reproduces all key features of the experimental room temperature data, plotted in direct comparison in Fig. 4.14(a), with good quantitative agreement in terms of the magnetic field amplitude and angular range, in which the different hysteretic structures are visible. To explore the behavior of Co-films at high temperatures, micromagnetic simulations of the field induced reversal have been also performed for a smaller anisotropy value, namely $K = 8 \times 10^4$ J/m^3, without changing any of the other magnetic parameters. Fig. 4.14(d) shows the $\Delta M/M_S$ (δ, H) color-coded map generated by the simulations in this case. In the entire angular range, only the low-field hysteresis band is present, exhibiting its largest ΔM values in the proximity of $\delta = 0$. Upon changing δ, the hysteresis band stays fairly constant up to the proximity of $\delta \approx 90°$, where it first increases its field extension and subsequently disappears along the out-of-plane field orientation. Just as in the high temperature experimental regime for the Co-films, which is displayed in Fig. 4.14(b) for the purpose of comparison, there are no high field nucleation islands, meaning that in the entire angular range, the reversal process proceeds via the instability of the uniform magnetic state.

Fig. 4.14 clearly illustrates that qualitatively different behaviors can emerge depending on the value of anisotropy *K*. For *K* values that are relatively low, but still sufficiently large to support a stripe domain state in remanence, a case obtained experimentally at T = 493 K in the Co-films (the right column plots), the nucleation type hysteresis is absent in contrast to the high *K* case (the left column plots). In the calculations, the absence of the nucleation phase at low *K* is confirmed in the entire H-δ parameter space upon analyzing the micromagnetic domain pattern, as illustrated in Fig. 4.15(a). For this, domain pattern were evaluated along the hysteresis loop branch that starts from positive saturation for all orientation angles δ. In the calculated domain pattern, shown in Fig. 4.15(a) and (b), the dark and bright regions correspond to the out-of-plane magnetization component being up or down, and the intermediate gray scale indicates in-plane alignment. In both figures, the film sample is uniformly magnetized for all values of δ if the applied magnetic field H is sufficiently strong. Reducing H gradually leads to the appearance of the stripe domain pattern in Fig. 4.15(a) for all values of the field angle δ. Thus there exists only a single type of phase boundary, shown as a dashed (purple) line, which is due to the instability of the uniform state and which triggers a second order phase transition into a stripe domain state for all δ. The onset of nucleation could still result in a positive nucleation field for δ values near the out-of-plane field orientation, which is indicated by the dashed-dotted (blue) line in Fig. 4.15(a), but this transition never occurs, because the system has already undergone the instability transition prior to reaching field values, where nucleation would be feasible. Thus, the first order phase transition into a nucleation domain state is suppressed here. It is worth mentioning that the dashed line in panel (a) has been generated by examining the evolution of the simulated domain patterns, whereas the dashed-dotted line has been derived from a theoretical model calculation according to [144]. The situation is very different and more complex when *K* is large, i.e. the low temperature case for the Co-films, as shown in Fig. 4.15(b). While the behavior for low δ values is fundamentally unchanged, the behavior is substantially altered for sufficiently large δ because nucleation occurs at higher field values than the stripe domain instability. Thus, the nature of the phase transition changes upon increasing δ from a second order phase transition near in-plane orientations to a first order phase transition near the out-of-plane

field alignment. Together with this change in the nature of the phase transition, occurs a change in the domain type that is found, as can be seen in Fig. 4.15(b).

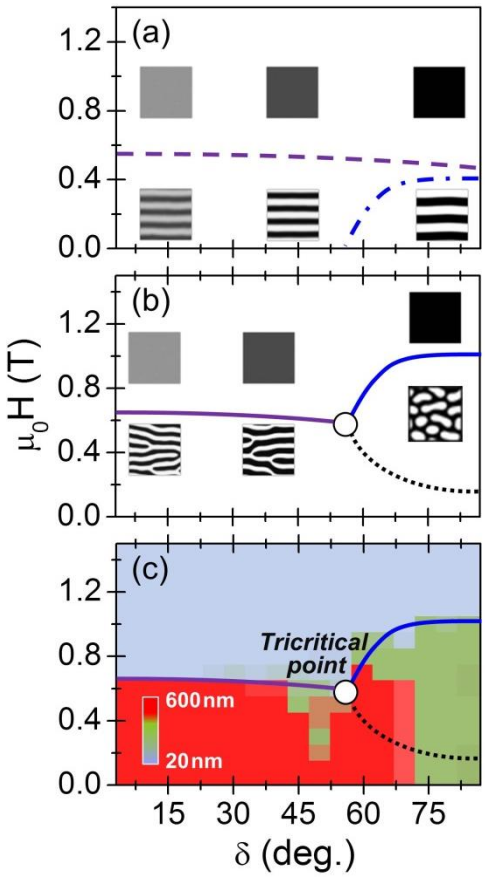

Figure 4.15: Calculated phase diagram for a 200 nm thick Co film assuming $K = 8.0 \times 10^4$ Jm^{-3} (a) or $K = 5.5 \times 10^5$ Jm^{-3} (b). The insets in (a) and (b) show simulated domain pattern, with an area of 1 μm × 1 μm, at different field strengths and angles, both corresponding to the position of the inset frame center in each case. (c) Color-coded map of the H and δ dependence of the order parameter *Op* for $K = 5.5 \times 10^5$ Jm^{-3} that identifies three different phases, their transition lines and the tricritical point connecting them. The corresponding *Op* scale bar (color code) is displayed in the figure.

While the low δ domain state consists of system size stripe domains that represent a collective magnetization state, at intermediate field strengths and large δ the magnetization structure is characterized by localized reversal domains that change in density and form, but have a lateral extension far smaller than the system size. This difference in the domain state nature also means that there must be a third phase line that separates the stripe domain states from the nucleation domain states for intermediate field strength. This phase line is also displayed in Fig. 4.15(b) as a dotted (black) line, together with the *tricritical point* that joints all three phase lines, represented by a circle. The

nature of the low field phase line[9] and the fact that it does not extend all the way to $H = 0$ will be discussed in conjunction with Fig. 4.16.

For the purpose of corroborating the qualitative discussion of Figs. 4.15(a) and (b) given above, a quantitative analysis of the underlying order parameter has been performed (see information in Appendix A), which allows for a formal distinction of the various phases. It is also worth mentioning that a certain microstructural non-uniformity has been assumed into the calculations by having a random lateral variation of K (see information in Appendix A). The resulting color-coded *Op* (H, δ)-map for the high *K* value of 5.5×10^5 J/m^3, corresponding to Fig. 4.15(b), is shown in Fig. 4.15(c). Here, the three phases appear as clearly distinct regions corresponding to clearly different order parameter values, which allow a localization of the individual phase boundaries and a confirmation of the qualitative discussion that was presented above in conjunction with Fig. 4.15(b). A certain level of noise in the region of the tricritical point, noticeable between $\delta = 45°$ and 50°, is apparent and generally expected as a result of the phase coexistence and the extremely flat energy landscape. The standard physical picture is that the nature of the tricritical point leads to a higher multiplicity of state space trajectories that are available within a micromagnetic system and, consequently, it leads to increased fluctuation-like order parameter variations. In the simulations, these "fluctuations" could be averaged-out by increasing the system size or averaging over an increased number of simulations with different microscopic realizations of the anisotropy distribution. In addition to this, another aspect of Fig. 4.15(c) deserves attention, because the low-field phase line, drawn schematically on top of the order parameter plot, deviates from the actual *Op*-values in the vicinity of $H = 0$. Specifically the, *Op*-values seem to indicate that this phase line intersects with the $H = 0$ axis. Fundamentally, however, this intersection of the phase line does not make any sense, because for $H = 0$, i.e. in the absence of any applied field, all δ values on the $H = 0$ axis represent only a single phase space point, given that δ is the field orientation axis. Thus, along the $H = 0$ axis, there ought to be only one magnetization state that

[9] The phase boundaries that are depicted in panels (b) and (c) of Fig. 4.15 as solid lines are smoothed out curves based upon of the observed order parameter change, which has been extracted from the simulations. On the other hand, the phase boundary shown as a dotted line in panels (b) and (c) of Fig. 4.15 is merely an approximate representation of the actual phase boundary, which can be computed by means of angular dependent calculations of the domain state energy as shown in Fig. 4.16.

represents the actual minimum of the free energy. Correspondingly, the low field phase line cannot extend all the way to H = 0 and cannot cross the H = 0 line. Instead, it ought to intercept the δ = 90º axis at a non-vanishing H-value. The discrepancy between this phase line and the calculated *Op* data can be explained if the low field phase line would represent a first order phase transition. In this case, the nucleation domains would remain a metastable magnetic state for very low H values in the vicinity of δ = 90º and the lack of thermal excitation in the simulations simply would not allow for the transition to a stripe domain state to occur in this regime. Correspondingly, the phase line could not be exactly positioned by means of the order parameter calculations.

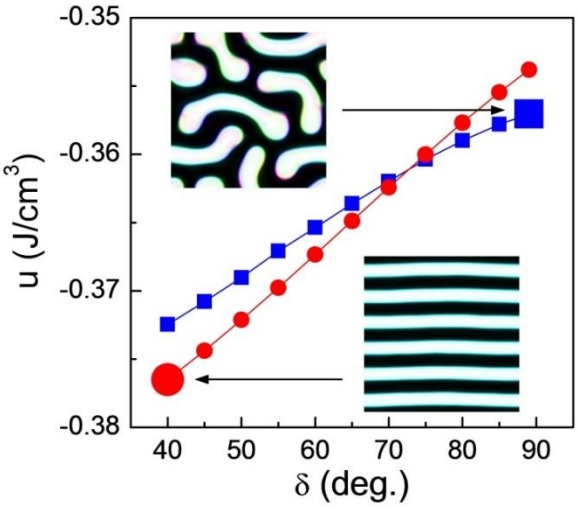

Figure 4.16: δ dependence of the energy density at μ_0H = 0.1 T for two different initial magnetization reversal states, namely: (i) shown as red dots, energy values for a stripe domain state that was initially generated via field reduction from saturation at constant δ = 40º and (ii) shown as blue squares, energy values for a nucleation domain state produced initially via field reduction from saturation at δ = 89º. The two insets show the simulated starting pattern for the two different domain states, which are found to change only minimally in the entire δ range shown here. The area of the domain pattern is 1 μm × 1 μm.

To check this point and to advance the understanding further, the nature of the phase line separating the stripe and nucleation domains in the low field region has been studied (dashed line in Figs. 4.15(b) and 4.15(c)). For this, Fig. 4.16 shows micromagnetic calculations of the domain state energy density across this phase boundary as a function of the field orientation δ at a fixed H, upon starting the δ-variation from two different initial states associated with the respective stripe and nucleation domain phase regions. In particular, the red dot symbols in Fig. 4.16 have been calculated by first reducing the magnetic field from μ_0H = 1.5 T to 0.1 T at a fixed angle of δ = 40º, which produces a stripe

domain state (see Fig. 4.16(b) or (c)), upon which the field orientation is changed by increasing δ stepwise all the way to 89º. On the other hand, the data represented by blue squares are generated by first reducing the magnetic field from $\mu_0 H = 1.5$ T to 0.1 T at a fixed angle of δ = 89º, which produces a nucleation domain state, upon which the field orientation is changed by decreasing δ stepwise all the way down to 40º. These calculations now enable one to identify the type of phase transition that is given by the low field phase line. First, Fig. 4.16 demonstrates that two stable solutions with distinct energies persist in the entire δ-range that is investigated here. Also, the inspection of the domain states verifies that the nature of each individual state remains intact, meaning that all red dots and all blue squares in Fig. 4.16 correspond to stripe domain and nucleation domain states, respectively. Furthermore, the energy levels of these two states cross each other, with the stripe domain state being the lowest energy state for small δ, while for δ near 90º the nucleation domain state has lower energy. For $\mu_0 H = 0.1$ T, the crossing occurs at δ = 73º. The existence of multiple (meta-)stable solutions that cross in energy at a specific point verifies the fact that the low field phase line in Figs. 4.15 (b) and (c) is indeed a first order phase transition line, which also explains the slight disagreement in between the schematic phase boundary location and the OP-data. With the results in Fig. 4.16, the nature of all the phase lines in Figs. 4.15 (b) and (c) has been identified, hereby achieving a detailed understanding of the field orientation dependence of the magnetization reversal in Co-films with perpendicular magnetic anisotropy as well as the qualitative changes that occur upon temperature variation.

4.7. Conclusions

In this part of the thesis, epitaxial Co (0001) and $Co_{90}Ru_{10}$ (0001) thin films with a magnetic easy axis perpendicular to the film plane have been successfully fabricated, hereby achieving a very small *c*-axis dispersion and an almost complete absence of the *fcc* phase. The room temperature measurements of the pure Co-films reveal the presence of two very different magnetization reversal processes depending on the applied field angle δ, namely an instability driven process leading to the generation of stripe domains for δ values near in-plane field orientation, and a nucleation domain process near out-of-plane field orientation that is hysteretic in nature. The temperature dependent study shows a

gradual shrinking of the nucleation regime, so that at sufficiently high temperatures, only the instability-driven second order phase transition occurs for all δ. The disappearance of the nucleation regime is driven by the strong temperature dependence of the magneto-crystalline anisotropy, and occurs before the anisotropy becomes too weak to support a stripe domain state altogether, i.e. it occurs while the stripe domain instability is still dominating the magnetization reversal process. The same types of results have been observed when the magnetocrystalline anisotropy is reduced by means of alloying Co with Ru. This type of alloy samples even allows the experimental verification of the stripe domain phase by means of MFM observations for samples, for which the nucleation domain process is already suppressed. Without taking into consideration the specific nature of the magnetocrystalline anisotropy of Co, namely the unusually strong role that K_2 plays for Co, micromagnetic simulations successfully reproduce the room temperature and high temperature magnetization reversal processes, as a function of the applied field angle[10]. Furthermore, by introducing a suitable order parameter based upon the different domain geometries associated with the different domain reversal processes, the H-δ phase diagram of PMA Co-films at room temperature has been found to contain three different magnetic phases. The nature of all the phase lines has been precisely identified, allowing one to unambiguously define the crossing point between $H_n(\delta)$- and $H_{cr}(\delta)$-curves as a *tricritical point*. It has furthermore permitted the derivation of a complete phase diagram for a perpendicular magnetic film in an applied field of any orientation and with the full incorporation of the magnetostatic energy term, which leads to a non-trivial modification of the magnetic phases. Given the simple assumptions made for the micromagnetic simulations, one can expect these findings to extend to many different ferromagnetic materials that exhibit out-of-plane magnetocrystalline anisotropies.

[10] In the micromagnetic model only a first order uniaxial anisotropy energy term K_1 has been introduced for the description of the orientation dependence of the free energy. Higher order components, which can be rather substantial in Co, have not been considered.

5. Chromia-Alumina alloys thin films

The magnetoelectric antiferromagnet Cr_2O_3 (chromia) develops an equilibrium net magnetization at its (0001) surface, which can be exploited to switch the coupled antiferromagnetic order parameter solely by magnetic means in single crystal thin chromia films with (0001) orientation. This chapter investigates whether these findings can be extended to alloys containing different oxide materials, focusing on the effect of Al_2O_3 doping onto the structural and magnetic properties of Cr_2O_3.

5.1. Introduction

As mentioned in Section 1.2.1, the corundum-type oxide of chromium Cr_2O_3 represents the archetypical material for the so-called magnetoelectric effect [23-26,28,32,159-161]. It exhibits a spin-polarized layer or boundary magnetization at the (0001) surface, which is symmetry protected and fully coupled to the bulk antiferromagnetic order parameter [27-29,162,163]. It has been demonstrated that both can be reversed together by the combined application of an electric and a magnetic fields in bulk chromia [28,29].

At the same time, it is known that material properties of epitaxially grown thin films are profoundly affected by the film thickness. In particular, thin film confinement may lead to substantial differences in the magnetic behavior of Cr_2O_3. In fact, the BM may create a sizable contribution in thin layers, whereas in thick films the magnetic surface energies have only a marginal contribution to the total magnetic energy. Accordingly, this chapter discusses how thickness may affect the reversal of the boundary magnetization in Cr_2O_3 samples with (0001) orientation, grown epitaxially on Al_2O_3 (sapphire) substrates. Previously, sapphire single crystals have been demonstrated to allow for epitaxial growth of chromia films due to the structural isomorphism and relatively low lattice mismatch [28,29,164]. The main purpose of the thickness dependence study is to investigate whether a pure magnetic switching of the BM could take place and, moreover, how sensitive the switching would be with respect to the film thickness and temperature.

On the other hand, bulk Cr_2O_3 exhibits the highest Néel temperature (T_N = 307 K) among the well-characterized ME-antiferromagnets, which has triggered a lot of work on this material, but unfortunately it does not provide enough flexibility for practical device operations [28]. The tuning of T_N in order to satisfy the requirements of spintronic devices is therefore an important issue. It is well known that alloying of materials is a crucially important pathway towards property optimization for application purposes, but it still remains an open fundamental question whether the BM is robust with respect to alloying chromia with another material. In fact, the persistence of the surface magnetism should happen only if the magnetoelectricity remains robust against alloying and thus space-inversion and time-reversal symmetries remain broken, while their combined effect is still a symmetry operation for the resulting alloy [27,165]. Therefore, a suitable pathway towards the optimization and preservation of the BM properties should be achievable by

alloying chromia with isostructural materials. In order to study the fundamental viability and soundness of this approach, Al_2O_3 doping has been selected here. Correspondingly, $Cr_{2-x}Al_xO_3$ alloy films with (0001) surface orientation are fabricated as a most suitable test case for the investigation of structural and magnetic properties, especially in terms of the robustness of boundary magnetization, which has been entirely unexplored so far [166-169].

It is hereby important to clarify that the work presented in this chapter takes place against the background of significant prior knowledge on the existence of BM in chromia (0001) surfaces, which is not directly verified here. However, all the findings that will be presented are completely consistent with the assumption of a boundary magnetization and its strong coupling to the bulk antiferromagnetic order parameter. The presence of a surface magnetic moment is a theoretically predicted phenomenon [27,28,162] based on rigorous symmetry arguments applicable for magnetoelectric antiferromagnets [27]. Experimentally the surface moment has been observed by magneto-optical measurements and spin-resolved photoemission [28], XMCD-PEEM [29] and with the highest surface sensitivity by inverse photoemission [29].

5.2. Fabrication process

Cr_2O_3 and $Cr_{2-x}Al_xO_3$ thin films were deposited on double side polished, 330 μm thick *c*-Al_2O_3 (0001) substrates. Before deposition, the substrates were ultrasonically cleaned using acetone, methanol and deionized water in consecutive cleaning steps. The conventional sputter deposition method for the production of Cr_2O_3 is DC-reactive sputtering using chromium targets under mixed argon and oxygen gas flow at high temperature [170]. The presence of oxygen very often results in unsteady deposition rates as well as target poisoning despite the usual obtainment of the desired stoichiometry after the optimization of the process parameters. In order to avoid these complications, sintered stoichiometric Cr_2O_3 and Al_2O_3 ceramic disk targets (99.9% pure) were utilized in the deposition process via RF magnetron sputtering. The deposition processes were started only after pre-sputtering of the oxide targets for at least 5 minutes with the shutters of the guns closed. In the initial part of this pre-sputter process, a 2 W/s time ramp was followed in order to reach the desired deposition power. All samples were then deposited at room

temperature (RT), in an Ar gas atmosphere of 4×10^{-1} Pa. A plasma power of 200 W was applied to the Cr_2O_3 target for the fabrication of pure chromia samples, whereas a power of 250 W for the Cr_2O_3 target and a varying power between 50 W to 165 W for the Al_2O_3 target have been selected in order to access the intended composition range of $x = 0\text{-}0.6$ (0-30%) for the deposition of the alloy films. In previous studies, it was shown that a combination of RT depositions with high temperature annealing is an effective method for the growth of epitaxial Cr_2O_3 thin films [21,164,168,171,172]. Therefore, the as-grown samples were recrystallized via ex-situ thermal annealing in vacuum (pressure < 3 Pa) for 1h at T = 1273 K in an external furnace (Carbolite wire wound single zone tube furnace). It is worth mentioning that in-situ annealing and high-temperature deposition approaches were explored as well, but with unsatisfactory results, which may be ascribed to the fact that the deposition system only reaches temperatures of up to 1123 K.

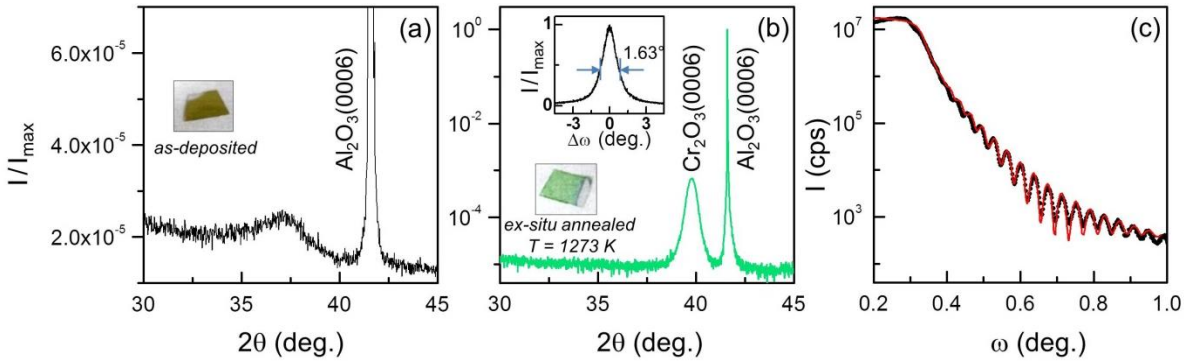

Figure 5.1: XRD θ-2θ scans of the as-deposited 100 nm thick Cr_2O_3 sample (a) and after T = 1273 K ex-situ annealing (b). On the left-hand side, photos of exemplary samples are shown in the as-deposited (a) and annealed state (b). The inset in (b) shows a rocking curve measurement for the Cr_2O_3 (0006) peak. (c) XRR curve measured for the annealed 100 nm thick Cr_2O_3 film. The red solid line represents the least-squares fit achieved with the X'Pert Reflectivity software.

Fig. 5.1(a) shows the XRD θ-2θ scan for the as-deposited sample of 100 nm thickness. After the RF sputter deposition at room temperature, a weak and fairly broad peak around $2\theta = 37°$ is visible, which is accompanied by the strong and narrow peak at $2\theta = 41.68°$ corresponding to the Al_2O_3 substrate (0006) diffraction. Comparative Energy-dispersive X-ray spectroscopy (EDX) measurements reveal that the as-grown films consist primarily of Cr_2O_3, which is either amorphous or nano-crystalline. After ex-situ thermal annealing at T = 1273 K, the sample transforms into an epitaxial layer of Cr_2O_3 as demonstrated by the intense and sharp diffraction peak at $2\theta = 39.78°$, corresponding to the (0001) surface orientation. The thermal "metamorphosis" of the sample is further supported by the

absence of any other peak in the XRD scan and visually by the appearance of the characteristic green color, as seen in picture in Fig. 5.1(b). To verify the narrow *c*-axis dispersion in the samples, rocking curve measurements have been performed for the Cr_2O_3 (0006) peak (inset in Fig. 5.1 (b)). The full width at half maximum value of the peak is $1.63° \pm 0.02°$, indicating that the Cr_2O_3 films achieved very good alignment of the *c*-axis orientation normal to the sample surface after the ex-situ thermal annealing. In order to monitor for possible interface diffusion of Al atoms from the substrate into the thin films during the high temperature sample processing, XRR measurements were performed after the ex-situ annealing step. Fig. 5.1(c) shows the XRR data for a 100 nm thick Cr_2O_3 sample together with the fitting result (red straight line) obtained by the X'Pert Panalytical Reflectivity software. The large number of very well defined Kiessig fringes, due to the high chemical gradient at the film-substrate interface, indicates very limited interdiffusion. From the data fit, it has been determined that the Cr_2O_3 film has a thickness $t = 101.40 \pm 2.10$ nm and an interface roughness of only $r = 0.32 \pm 0.11$ nm. Very similar XRR-data have been measured for all the samples, with an estimated interface roughness of less than 0.5 nm in all cases. Furthermore, the findings are fully consistent with the scientific literature, where significant interface diffusion has only been observed for temperatures above 1473 K [173]. Therefore, in order to achieve consistently good epitaxy, T = 1273 K has been utilized as annealing temperature for the different oxide samples studied in this thesis after the initial RF sputter deposition at room temperature onto 330 μm thick *c*-Al_2O_3 (0001) sapphire substrates. For the Cr_2O_3 thin films, t = 26, 50, 60 and 100 nm thicknesses were selected, while for all $Cr_{2-x}Al_xO_3$ samples the film thickness was fixed at 100 nm. The nominal Al content x (atomic percent), to which this chapter refers, has been determined through measurements of the deposition rates for the two different oxides, which were done with high accuracy via XRR as explained already in Section 2.1.1. This method allowed for the determination of the atomic content with a relative error of better than $x = 0.02$ in the entire range explored in this chapter. In order to check for possible compositional modifications induced by the ex-situ high temperature annealing, EDX measurements have been performed on the samples before and after the heat treatment, which verify the preservation of the relative proportion of Al and Cr upon high temperature

annealing and confirm the nominal chemical composition values in the entire concentration range explored.

5.3. Structural characterization

XRD θ-2θ scans in the angular range from 36° to 43° (a-c) and from 83° to 93° (d-f) are shown in Fig. 5.2, normalized to the intensity of the Al_2O_3 (0006) peak in each individual scan, for pure chromia samples of thicknesses t = 26, 50, and 60 nm after the ex-situ annealing. At low scattering angles (Figs. 5.2 (a-c)) the measurements show two clearly separated Bragg diffraction peaks. Beside the reference substrate Al_2O_3 (0006) signals, appearing at 2θ = 41.68°, the three different thicknesses show only an intense and sharp diffraction peaks at 2θ = 39.78°, which correspond to the desired (0001) orientation of Cr_2O_3. For larger scattering angles, shown in Figs. 5.2(d-f), only two constructive interference peaks in each measurement are observed at the positions of Al_2O_3 (00012) and Cr_2O_3 (00012). The presence of higher order diffractions is a clear indication of the good crystallographic quality achieved after the heat treatment. In fact, in case of poor epitaxy, they would not be visible or even further reduced. Accordingly, in addition to the substrate peaks, the total angular range shows only well-defined (0006*n*) Cr_2O_3 peaks, without the appearance of any other Bragg reflection. Fig. 5.2 also shows XRR data for the 26 nm (g), 50 nm (h) and 60 nm (i) thick Cr_2O_3 samples together with the corresponding fit result (red straight line) obtained by the X'Pert Panalytical Reflectivity software.

Nominal thickness (nm)	*Thickness (nm)*	*Interface roughness (nm)*	*Density (g/cm^3)*
26	25.8 ± 0.8	0.48 ± 0.12	5.22 ± 0.21
50	49.5 ± 0.6	0.36 ± 0.08	5.12 ± 0.08
60	59.8 ± 0.4	0.47 ± 0.10	5.20 ± 0.09

Table 5-I: **Material parameters obtained by the least-squares fit to the XRR data achieved with the X'Pert Reflectivity software.**

In all cases, the observed large number of very well defined Kiessig fringes, whose spacing is inversely proportional to the thicknesses, indicates the presence of a high chemical gradient at the chromia-alumina interface. From the data fit, the Cr_2O_3 films thickness, interface roughness and density have been determined, shown in Table 5-I. It is also noteworthy that the three samples have a density close to the room temperature bulk value of Cr_2O_3, i.e. 5.21 g/cm^3.

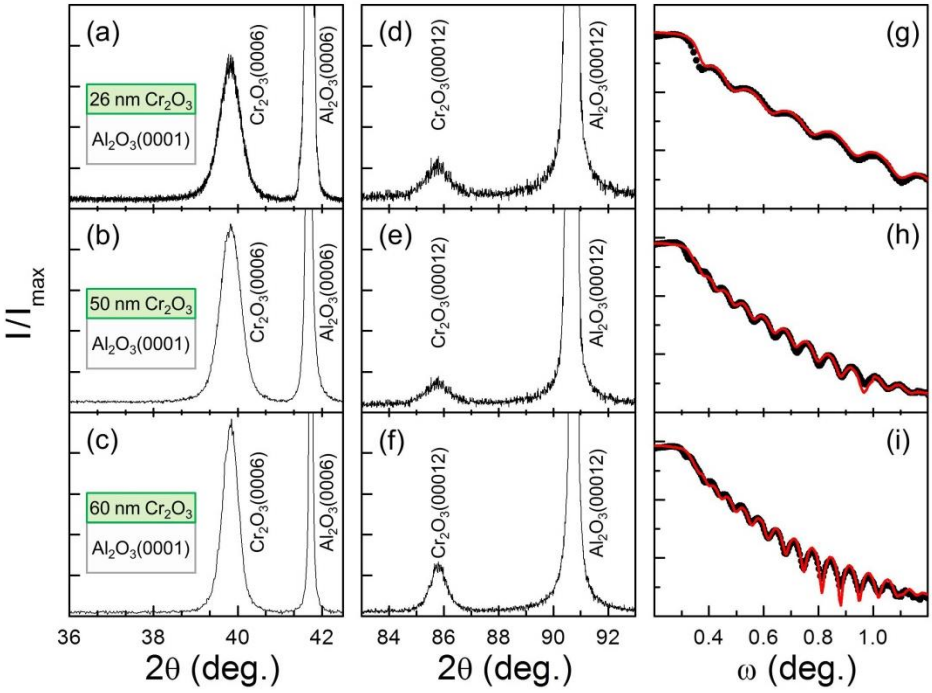

Figure 5.2: XRD θ-2θ scans of the ex-situ annealed 26 nm (a,d), 50 nm (b,e) and 60 nm thick (c,f) Cr_2O_3 samples. XRR curves measured for the annealed 26nm (g), 50 nm (h) and 60 nm (i) thick Cr_2O_3 films. The red solid lines represent the least-squares fit, from which the layer thickness and interface roughness are determined.

For the $Cr_{2-x}Al_xO_3$ films, θ-2θ scans were performed using the coplanar and non-coplanar geometries[11] described in Section 2.2.2 and depicted respectively in Figs. 2.9(a) and (c) in order to identify the crystal structure and to determine the lattice parameters. Fig. 5.3(a) shows the coplanar XRD θ-2θ patterns for the entire set of samples, normalized to I_0, which is the intensity of the $Cr_{2-x}Al_xO_3$ (0006) peak in each individual scan. Beside the reference substrate peaks, the entire set of data shows well-defined $Cr_{2-x}Al_xO_3$ (0006) peaks of nearly uniform width without the appearance of any other crystallographic diffraction signal. Fig. 5.3(b) shows the non-coplanar XRD θ-2θ scans normalized to I_0, which is the intensity of the $Cr_{2-x}Al_xO_3$ $(10\bar{1}4)$ peak in each individual scan. Also for this measurements, only $Cr_{2-x}Al_xO_3$ $(10\bar{1}4)$ peaks of consistently narrow width associated with the (0001) surface orientation were found in addition to the substrate signal. Thus, the structural sample analysis verifies the persistence of the original corundum crystal

[11] In the non-coplanar configuration, the diffraction measurement parameters were optimized only for the epitaxial alloy film reflections. Therefore, the Al_2O_3 $(10\bar{1}4)$ diffraction peaks exhibit a certain level of variation, without however affecting the reliability of the experimental data.

structure in the entire set of samples, necessary for the survival of the boundary magnetization [27].

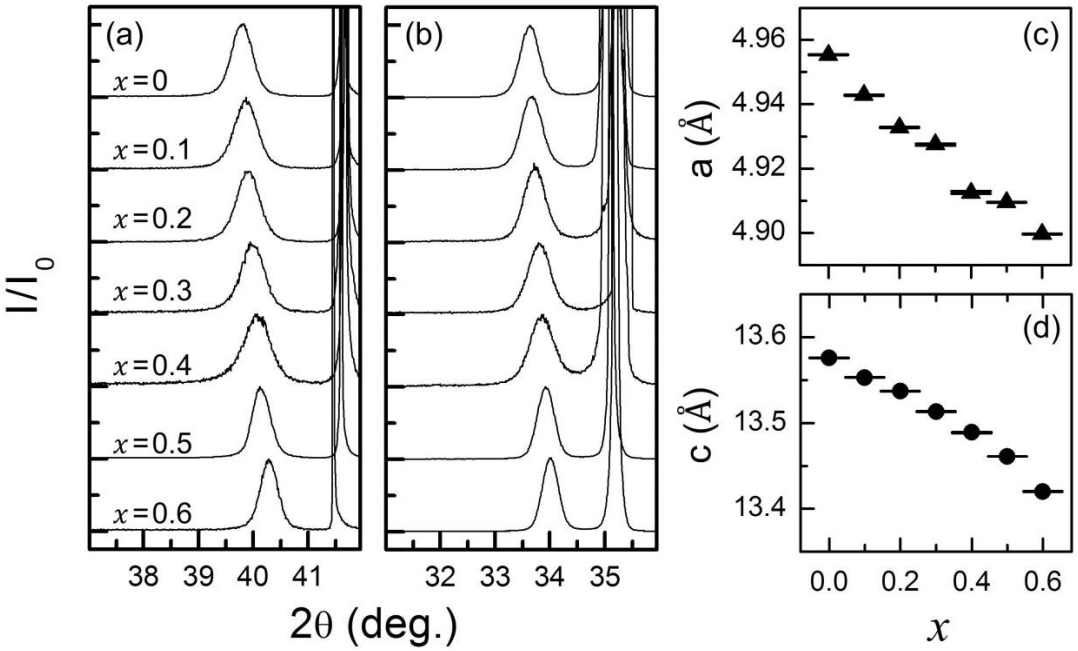

Figure 5.3: XRD θ-2θ scans of 100 nm thick $Cr_{2-x}Al_xO_3$ films of varying dopant concentration *x*, displayed in (a) and (b) respectively. (c,d) display the *x* dependence of the $Cr_{2-x}Al_xO_3$ lattice parameters, determined from (a,b).

The ionic radius of the Cr^{3+} is larger than that of Al^{3+}, so that the distance between the lattice planes decreases upon increasing the amount of alumina in the alloy [169]. Correspondingly, the XRD peak positions in the samples shift from diffraction angles of 39.75° (0006) and 33.6° ($10\bar{1}4$) for the pure Cr_2O_3, towards the Al_2O_3 (0006) and ($10\bar{1}4$) diffraction peaks upon increasing *x*. This *x*-dependent peak shift in the absence of significant broadening verifies the simple Cr^{3+} substitution by Al^{3+} and the corresponding formation of isovalent solid solutions type samples in the entire range between $x = 0$ and $x = 0.6$. Also, the XRD data verify the epitaxial quality of the growth process, which allowed for the fabrication of chromia-alumina alloy films with *c*-axis surface orientation in the here investigated concentration range. The lattice constants *a* and *c* of the alloy films were measured from the peak positions in the θ-2θ scans and are plotted in Figs. 5.3(c,d). Both *a* and *c* decrease linearly with *x*, further corroborating the smooth tunability of the high-quality growth process. The agreement with lattice constants published for polycrystalline bulk $Cr_{2-x}Al_xO_3$ alloy samples is very good, as can be seen from the comparison in Table 5-II [167,168].

Sample composition		This work		Reference values[167]		Reference values[168]	
Al_2O_3 at%	Cr_2O_3 at%	*a* (nm)	*c* (nm)	*a* (nm)	*c* (nm)	*a* (nm)	*c* (nm)
0	100	0.4955	1.3578	0.4958	1.3594	0.4954	1.3573
5	95	0.4943	1.3553				
10	90	0.4932	1.3537	0.4934	1.3502	0.4939	1.3530
15	85	0.4927	1.3513				
20	80	0.4912	1.3489	0.4910	1.3424	0.4922	1.3471
25	75	0.4909	1.3461				
30	70	0.4899	1.3422	0.4889	1.3356	0.4903	1.3417

Table 5-II: **Comparison between bulk lattice parameters and values found in this work.**

Thus, the structural sample analysis verifies the high crystallographic quality achieved by means of the optimized growth process resulting in well-ordered corundum Cr_2O_3 and $Cr_{2-x}Al_xO_3$ thin films with perpendicular *c*-axis orientation aligned with the substrate lattice, which is necessary for the development of the boundary magnetization [27].

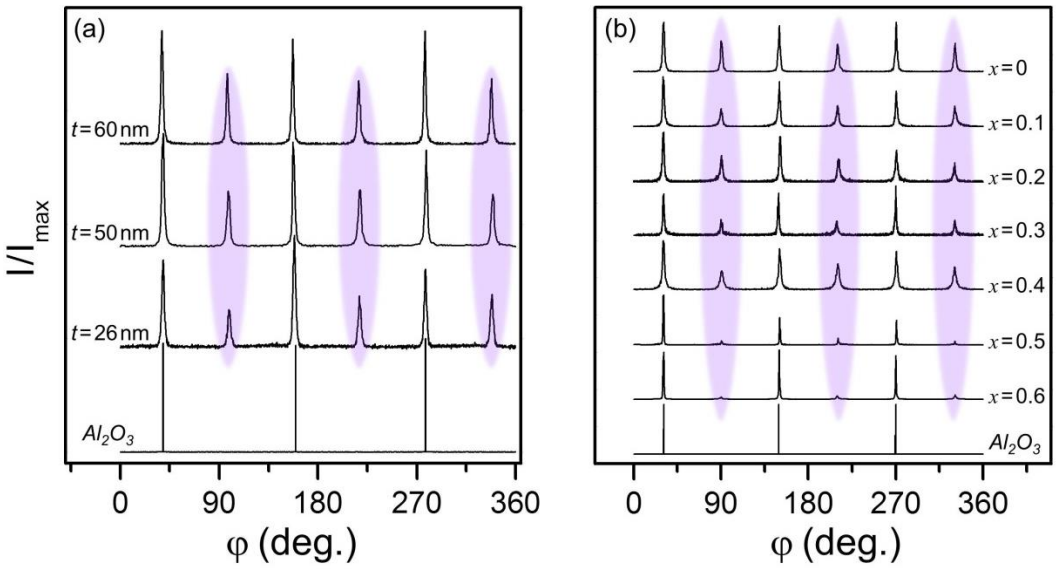

Figure 5.4: XRD φ-scans at the 2θ pole of the $(10\bar{1}4)$ planes for Cr_2O_3 thin films of different thickness (a), for various $Cr_{2-x}Al_xO_3$ thin films (b), and for the Al_2O_3 substrates (a,b). The purple ellipses mark the twinned domain positions.

The in-plane orientation relationship between the substrates and the epitaxial thin layers was studied as usually by means of XRD φ-scans at the $\{10\bar{1}4\}$ poles via full 2π rotation measurements, shown in Figs. 5.4(a,b). In both sets of data the sapphire substrate gives rise to three diffraction peaks separated by 120°. In contrast to the substrate, the pure Cr_2O_3

(Fig. 5.4(a)) and the alloy $Cr_{2-x}Al_xO_3$ (Fig. 5.4(b)) samples exhibit six peaks, separated by 60°. Since the corundum crystal structure has three-fold symmetry along the [0001] direction, the occurrence of the six-fold symmetry indicates that the films contain twinned domains (marked by purple ellipsis in Figs. 5.4(a,b)), which have been previously reported to occur due to the high temperature annealing [21,164,174]. Whereas the pure chromia samples show a constant intensity of the diffraction peaks corresponding to twinned domains, by increasing the Al content x and consequently by reducing the lattice mismatch, their presence diminishes in the alloy samples and the corresponding XRD intensity of the twinned domain peaks decreases, disappearing almost entirely for $x = 0.6$.

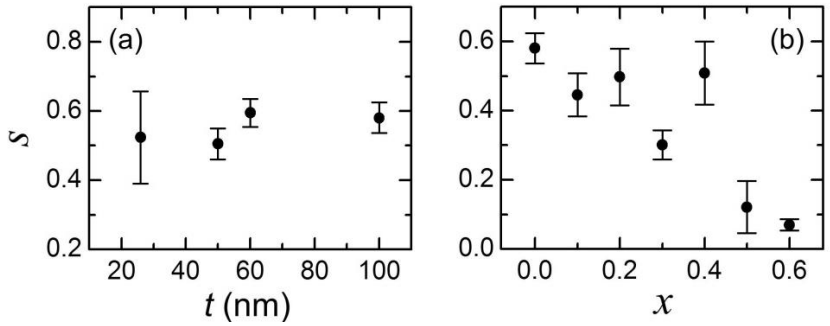

Figure 5.5: (a) thickness dependence of *S* for $x = 0$. (b) x dependence of *S* for $t = 100$ nm.

To visualize this effect more clearly, Fig. 5.5 shows the quantity S, the ratio between the average φ-scan XRD intensity of the twinned domains normalized to the untwinned ones, i.e. $S = \langle I \rangle_{twinned} / \langle I \rangle_{untwinned}$. As can be seen, S stays approximately constant upon changing the chromia thickness, Fig. 5.5(a), whereas it decreases substantially for large x, Fig. 5.5(b), which means that an improvement of the epitaxial growth quality has actually been achieved by alloying Cr_2O_3 with Al_2O_3. As will be shown later, this aspect turns out to be important for the boundary magnetization, because the magnetic surface polarization depends on the ratio of twinned to untwinned domains [174].

5.4. Giant temperature sensitivity of the coercive field in epitaxial chromia

The most common way to characterize a ferromagnetically ordered system is by measuring the magnetic moment in its isothermal response to an externally applied magnetic field. This results in the common m vs. H hysteresis loop, as described in Section 1.1.1. However, in the case of chromia thin films, magnetometry in large applied magnetic fields

is plagued by an ill-defined background signal, which masks the weak moment originating from the BM coming from a single layer of magnetic moments. Therefore, the characterization via isothermal hysteresis loops is not a viable option. Consequently, a more elaborated experimental procedure has been developed and conducted, shown in Figs. 5.6(a,b), which allows studying the temperature dependence of out-of-plane remanent moment. First, the sample is cooled from T = 350 K > T_N down to T = 100 K in a positive magnetic field to polarize the surface spins. After the field removal, a zero field heating (ZFH) curve is then measured. Note that for the measurements here, and the ones reported in the next section, true ZFH conditions have been achieved by quenching the superconducting magnet in order to eliminate any magnetic background contribution, i.e. insuring the absence of paramagnetic and diamagnetic signals.

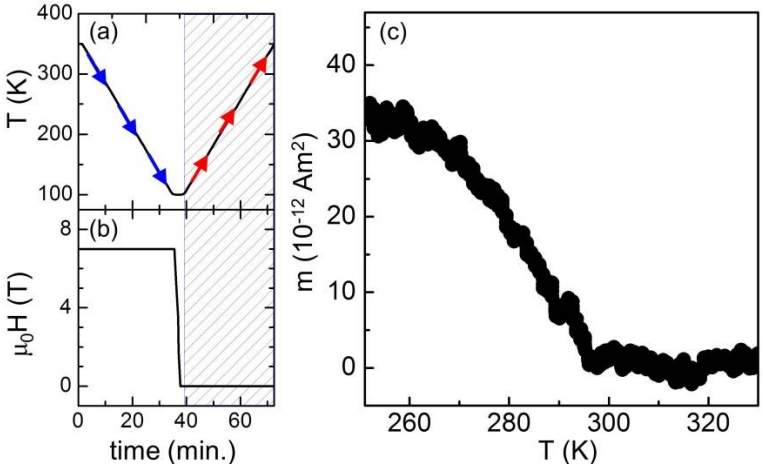

Figure 5.6: (a) and (b) display the experimental protocol showing temperature variation (a) and the simultaneous magnetic field variation vs. time (b). The dashed rectangular regions indicate the ZFH part of the sequence, where magnetization data were actually measured. (c) temperature dependence of the out-of-plane remanent moment in a 26 nm thick Cr_2O_3 sample.

Fig. 5.6(c) shows the temperature dependence of *m* for the 26 nm thick chromia sample. In order to improve the signal to noise ratio the displayed data represent the arithmetic average of six independent data sets. A linear background has been determined for T > 310 K > T_N (t = 26 nm) and after extrapolation to T < T_N it has been removed from the data for all T. The measurements show a positive remanent magnetization value due to the positive magnetic field applied during FC. Upon increasing the temperature, the signal decreases continuously until it vanishes at T≈297 K. For higher temperatures, the BM disappears simultaneously with the antiferromagnetic order and the sample shows a PM behavior

including a vanishing remanent magnetization in the absence of an external magnetic field. Note that the BM is measured as remanent magnetic moment on ZFH, which implies that FC in positive H selects a positive AFM order parameter. The AFM spin structure and its corresponding BM have been energetically favored by the Zeeman energy via the magnetic field-induced alignment of the surface spins. Here, due to reduced interaction with its neighbors, spins are aligned preferentially parallel to the applied field and act as a two dimensional surface nucleus while the AFM long-range order is being established. Condensation of the AFM order evolves from the surface into successive layers due to strong coupling between the BM and the AFM order parameter. The smallness of the Zeeman energy of the BM in an applied field renders this mechanism ineffective if the ratio of surface-to-bulk spins becomes small in the limit of bulk chromia. Thus, an applied axial magnetic field of $\mu_0 H = 7$ T, which is the maximum achievable by the SQUID system, has been always chosen for any FC performed in this thesis in order to maximize the energetic contribution of the BM. However, as the detailed quantitative analysis in the next section discloses, the resulting Zeeman energy is not sufficient to induce a single domain AFM spin structure. Nonetheless, it is capable to promote a net preferential orientation parallel to the field direction applied during the cooling. In addition, it is observed here that the thin films show reduced Néel temperatures relative to the bulk critical temperature of $T_N = 307$ K. Usually, in thin films, finite size effects and defects such as potential oxygen vacancies can reduce T_N substantially below the bulk value, and $T_N << 307$ K is commonly observed [176]. The critical temperatures of the sputtered thin films here, $T_N \approx 297$ K (t = 26 nm), 299 K (t = 50 nm), and 300 K (t = 60 nm), are remarkably close to the bulk value in comparison with thin film critical temperatures reported in the literature, which indicates an overall excellent sample quality compared to previous work [176].

The measurement sequence shown in Fig. 5.6(a,b) only permits the measurement of the remanent magnetic moment after applying the highest magnetic field achievable with the experimental setup. Therefore, in order to study the magnetization reversal of the BM, the experimental protocol has been modified by adding an intermediate step, which allows monitoring the reversal as a function of temperature rather than magnetic field.

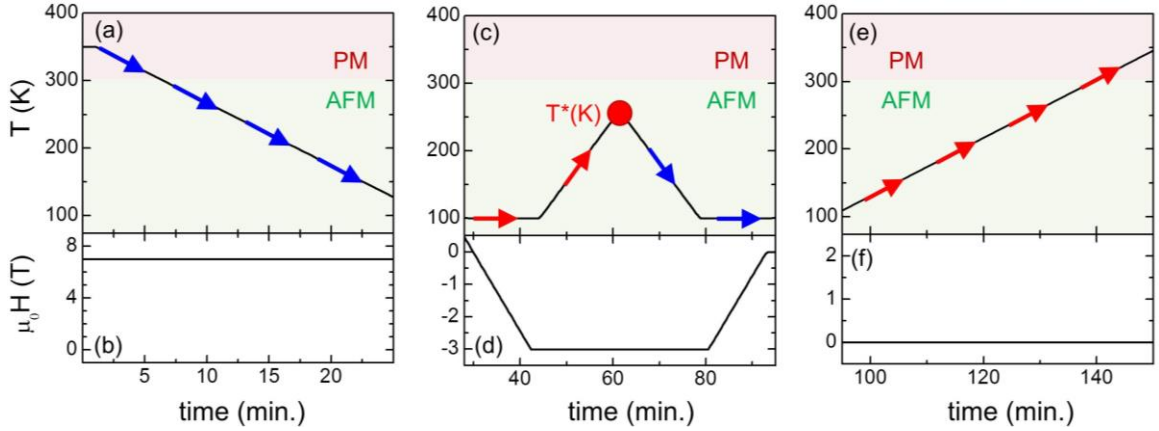

Figure 5.7: (a)-(f) show the three consecutive steps that compose the experimental protocol for the reversal. (a), (c) and (e) display the temperature variation vs. time while the simultaneous magnetic field variations vs. time are shown in (b), (d) and (f).

Figs. 5.7(a)-(f) shows the three consecutive steps that form the adjusted experimental sequence. The FC procedure (Figs. 5.7(a,b)) is followed by the application of the negative reversal magnetic field $\mu_0 H_R$ at T = 100 K. Subsequently the sample is field heated (FH) to a variable target temperature *T**(K), marked by a red circled in Fig. 5.7(c). Here the system is maintained in thermal equilibrium for a waiting time of 2 minutes. Afterwards, the sample is field-cooled again still in the presence of the $\mu_0 H_R$ down to T = 100 K, Figs. 5.7(c,d). Note that *T** does not exceed the magnetic ordering temperature. Moreover, it insures that AFM long-range order is maintained at all times without crossover into the paramagnetic phase. After FC from *T** back to T = 100 K, a ZFH curve is measured, Figs. 5.7(e,f). Some details of the experimental protocol outlined above are particularly crucial for the consistent interpretation of the data. It is of paramount importance to keep in mind that the data displayed in Fig. 5.8 are ZFH data and that the applied reversal fields of substantial magnitude have negative sign while the remanent moment of the sample has positive sign until reversal through thermal activation is achieved. These facts eliminate the possibility that the measured moments are field-induced residuals of finite susceptibility or the result of long-range ordered FM impurities. Fig. 5.8 shows selected ZFH curves for *T** = 150 (light blue triangles), 290.6 (black circles), 290.8 (green hexagons), 291.2 (blue rhombi), and 292.0 K (dark red pentagons) for a reversal field of $\mu_0 H_R = -3$ T, respectively. As one can clearly see from these data sets, the magnetic

switching of the BM takes place in a small temperature range around T_f = 291 K. At T << T_f, the BM is virtually unperturbed by the presence of the negative reversal field.

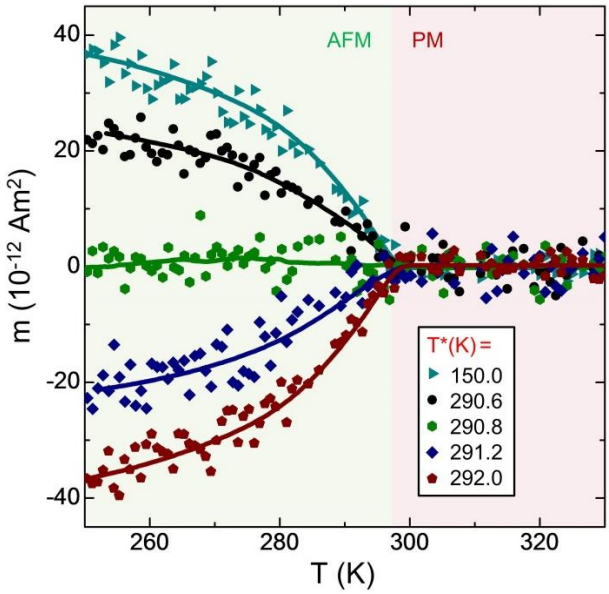

Figure 5.8: ZFH *m*(*T*) data of the 26 nm thick Cr_2O_3 sample after applying the field-temperature sequence shown in Fig. 5.7(a-f) with $\mu_0 H_R$ = -3T and temperatures T* = 150.0 (light blue triangles), 290.6 (black circles), 290.8 (green hexagons), 291.2 (blue rhombi), and 292.0 K (dark red pentagons). The solid lines are guides to the eyes.

However, upon approaching and ultimately exceeding T_f = 291 K the BM is reversed. To visualize the sharpness of the reversal and to allow for a further data analysis, Fig. 5.9 shows the result of a numerical integration for the *m*(T) data normalized to the corresponding maximum integral value, i.e.:

$$\langle m \rangle_T = \frac{1}{50\ K} \int_{250}^{300} m(T) dT \tag{5.1}$$

$$\langle m \rangle'_T = \langle m \rangle_T / (\langle m \rangle_T)_{max} \tag{5.2}$$

of the ZFH data *m*(T) of the 26 nm thick samples for different reversal magnetic field values $\mu_0 H_R$ = -7 T (a), -5 T (b) and -3 T (c), respectively. Vertical bars represent the average standard deviations of the *m*-data for 250 K ≤ T ≤ 300 K. The dependence of $\langle m \rangle'_T$ on T^* is used to define the flipping temperature T_f for each magnetic reversal field value $\mu_0 H_R$. In the hypothetical absence of noise, the reversal of the BM could be deduced from a single data point *m*. However, in order to take advantage of statistics, the average defined via Eq. 5.1 has been introduced. Although the integration interval has an element of arbitrariness, the results of the analysis do not depend on details of the definition of $\langle m \rangle_T$.

The $\langle m\rangle'_T$ (T^*) data illustrate that the reversal takes place at a reverse field dependent $T^* = T_f$. It is defined as the inflection point of $\langle m\rangle_T$ (T^*).

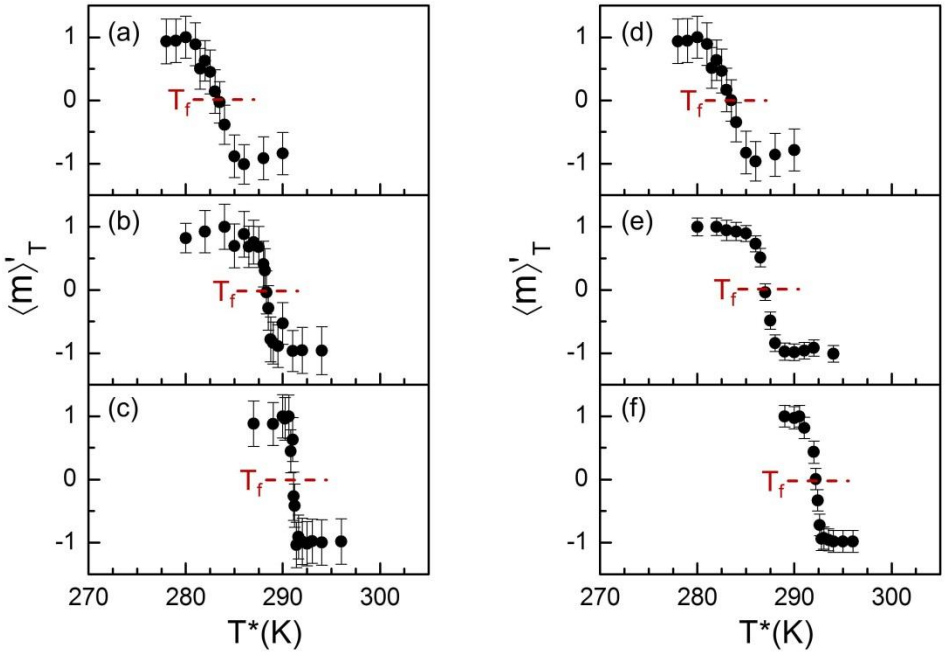

Figure 5.9: $\langle m\rangle'_T$ (T^*) data for the 26 nm thick Cr_2O_3 sample after μ_0H_R = -7 T (a), -5 T (b), and -3 T (c). $\langle m\rangle'_T$ (μ_0H_R = -7 T, T^*) for 26 nm (d), 50 nm (e), and 60 nm (f) sample thicknesses. The red dashed lines indicate the inflection points that define T_f.

The data sets in Figs. 5.9(a-c) show that, at a fixed thickness, T_f increases by decreasing the absolute value of the reversal field and, moreover, the transition from positive to negative BM becomes increasingly sharp. Furthermore, Figs. 5.9(d-f) show selected $\langle m\rangle'_T$ vs. T^* curves measured for a reversal field of $\mu_0H_R = -7$ T for three chromia samples, having a thickness of 26 nm (d), 50 nm (e) and 60 nm (f), respectively. The data in (d-f) show that at a fixed reversal field both the position and the sharpness of the BM reversal depend on the thickness. For the thinnest film, a broad transition occurs at T_f = 283.6 K, while for the thickest film, a narrow switching takes place at T_f = 292.1 K. Therefore, the experiments show that both T_f and the temperature dependent width w of the reversal depend on the chromia thickness. In an isothermal magnetization reversal at $T = T_f$ one would identify the reversal field with the coercive field H_C of the hysteresis. Therefore H_C and H_R can be used synonymously. Fig. 5.10 represents a summary of the extensive magnetometry investigations. Triangles, circles, and squares show $\mu_0|H_C|(T_f)$ for the three samples with different thickness. The horizontal bars quantify the transition width w of the

reversal of the BM determined from the full width at half maximum of $d\langle m\rangle_T/dT^*$. Extrapolation of $\mu_0|H_C|(T_f)$ towards the interception with the x axis defines $T_f(\mu_0 H_C = 0, t)$.

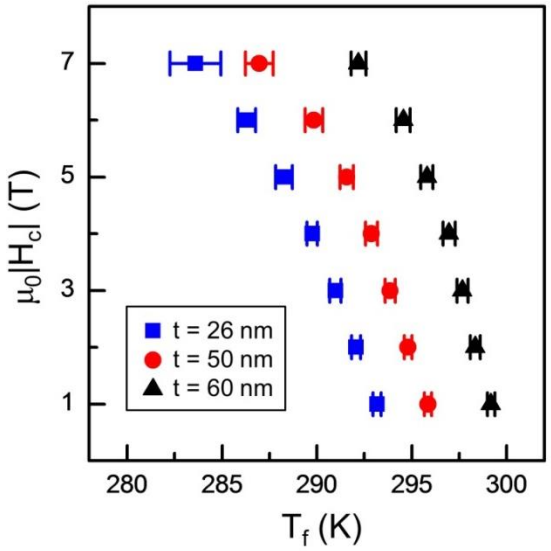

Figure 5.10: Coercive field versus flipping temperature T_f for 26 nm (squares), 50 nm (circles) and 60 nm (triangles) thick samples. The horizontal bars quantify the transition width (see text for definition).

At this temperature an infinitesimal small magnetic field suffices to reverse the BM. Although BM and AFM order parameter are substantially reduced in magnitude due to thermal excitation they both remain finite at $T_f(\mu_0 H_C = 0, t)$, which increases with increasing thickness of the Cr_2O_3 layer and is expected to approach asymptotically the bulk Néel temperature. In addition, also the steepness of $\mu_0|H_C|(T_f)$ increases with increasing film thickness. This is quantified by the thickness dependence of $\mu_0|dH_C/dT_f| \approx 1.10$ T/K (t = 60 nm), 0.78 T/K (t = 50 nm), and 0.56 T/K (t = 26 nm). Comparison of $\mu_0|dH_C/dT_f|$ for chromia thin films with presently investigated materials optimized for energy assisted magnetic recording reveals the enormous potential of magnetoelectric antiferromagnets with switchable BM for magnetic recording media. In fact, values of only up to 0.09 T/K, i.e. one order or magnitude smaller than measured here, have been reported so far [175]. Also the fact that it is the ferromagnetically ordered surface layer that responds to the externally applied magnetic field, makes these materials especially suitable for utilization in magnetic recording schemes, as this would allow for an ideal minimization of the effective head-media spacing. However, in order to develop chromia thin films into practical heat assisted recording media, tuning of the Néel temperature towards higher ordering temperatures is a necessary prerequisite.

5.5. Tuning of the Néel temperature

The highly oriented epitaxial nature of the alloy film samples allows the use of the boundary magnetization as a probe to study the magnetic transition and consequently the Al_2O_3 concentration x dependence of the critical temperature T_N values. Also here, in order to suppress any background susceptibility contribution, the remanent magnetic signal has been measured in the complete absence of any applied magnetic field. Figs. 5.11(a-b) show the ZFH magnetization measurement sequence, starting at T = 100 K and followed up to T = 350 K, after first FC the sample in an applied magnetic field of $\mu_0 H$ = 7 T from T = 350 K down to T = 100 K. Fig. 5.11(c) shows the resulting m(T) curves for the entire set of the epitaxial $Cr_{2-x}Al_xO_3$ alloy films. All data show a positive magnetization value at low temperature due to the positive magnetic field applied during FC, which leads to the selection of a state with positive BM. Upon increasing the temperature, the remanent signal decreases continuously until it disappears at a clearly defined temperature. For higher temperatures, no magnetization can be observed anymore in the absence of an external magnetic field.

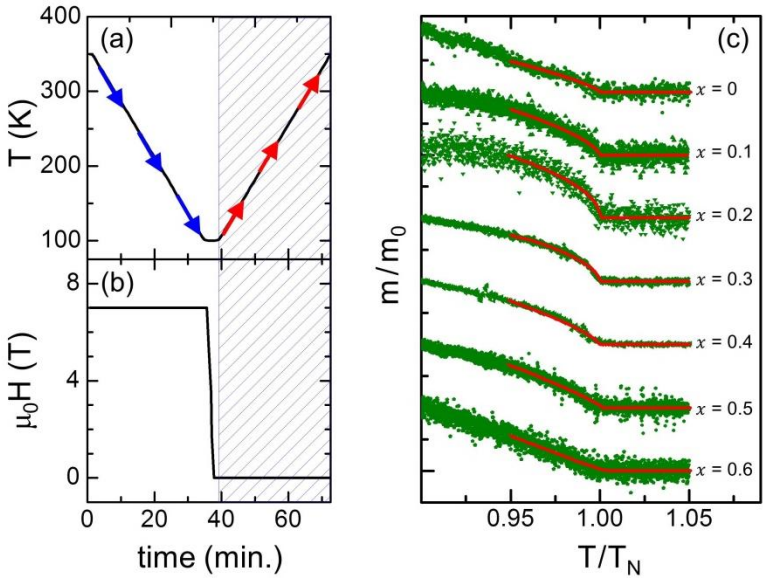

Figure 5.11: (a) and (b) display the experimental protocol showing temperature variation vs. time (a) and the simultaneous magnetic field variation vs. time (b). The dashed rectangular regions indicate the ZFH part of the sequence, where the data were actually measured; (c) temperature dependence of the out-of-plane remanent moment in $Cr_{2-x}Al_xO_3$ thin films with varying concentration x. The red lines show least-squares fits to Eq. 5.3 for each of the sample data sets.

For the purpose of a side-by-side comparison of the m(T) data of all samples in Fig. 5.11(c), the magnetic signal was normalized by the respective moment measured at $T = 0.9 \times T_N(x)$, called m_0, with $T_N(x)$ being the critical temperature of the antiferromagnetic order in the $Cr_{2-x}Al_xO_3$ alloy film of composition x. $T_N(x)$ itself, together with the critical exponent β, was determined by fitting the experimental data in the temperature range $0.95 \times T_N(x) < T < 1.05 \times T_N(x)$ to the power law function:

$$m(T) = A \cdot (T_N - T)^{\beta} \cdot H(T_N - T) \tag{5.3}$$

with $H(T_N - T)$ being the Heaviside function. Hereby, the critical exponent β, the Néel temperature T_N and a scaling factor A were utilized as fit parameters. Fig. 5.11(c) shows the fitting results as red solid lines in direct comparison to the experimental data. In each case, an excellent agreement has been found between the experimental data and the least-squares fit according to Eq. 5.3. The dependence of the BM on the AFM ordering allows one to identify the critical temperatures. This is a crucial observation for the epitaxial $Cr_{2-x}Al_xO_3$ film samples, because it means that substituting Cr atoms by Al atoms destroys neither the AFM order, nor the BM. The extracted values for the critical temperature $T_N(x)$ are shown in Fig. 5.12(a). For pure Cr_2O_3, i.e. x = 0, T_N is very close to the value for bulk Cr_2O_3, specifically it has been determined to be T_N = 303 K, and also very similar to previously reported values for samples of comparable thickness, grown by different deposition techniques [28,29,176]. In the case of the alloy films, $T_N(x)$ decreases upon introducing Al into the Cr_2O_3 lattice and does so in an almost linear fashion with x. The reduction of $T_N(x)$ upon increasing x is not surprising, given that Al^{3+} ions reduce the AFM exchange interaction of the crystal. Quantitatively, the decrease of the critical temperature is in accordance with the results observed for bulk polycrystalline $Cr_{2-x}Al_xO_3$ samples [168,169]. The extracted β values for the critical exponent, together with the associated errors estimated from each of the least-squares fits, are plotted in Fig. 5.12(b) as a function of x, along with critical exponents for the 3D Heisenberg (β = 0.365) and the 3D Ising (β = 0.3265) models, and prediction made for the critical exponent of the surface of a 3D Ising system (β = 0.78) [177-179]. Despite notable variations in between the extracted critical exponents for the samples, all β values are consistently and substantially larger than what one would expect for a 3-dimensional system. On the other hand, the average value $\bar{\beta} = 0.73 \pm 0.07$ that has been determined from the experiments is consistent within the

statistically estimated error with the critical exponent value $\bar{\beta}_S = 0.78 \pm 0.02$ that was predicted by Binder for the surface magnetization of a 3D Ising model. The estimated error assigned to the average critical exponent $\bar{\beta}$ above is the standard deviation of the mean.

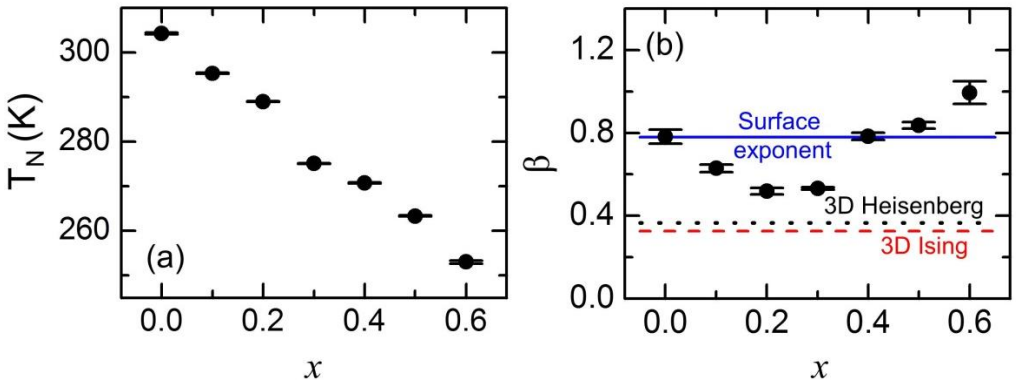

Figure 5.12: Al_2O_3 concentration x dependence of the extracted critical temperature T_N values (a) and of the extracted critical exponent β (b). The straight blue line indicates the surface exponent predicted by Binder et al., the black dotted line indicates the 3D Heisenberg model value, and the dashed red line shows the 3D Ising model β [177-179].

Under the assumption of a purely statistical Gaussian distribution for the observed β values, one would correspondingly expect that 68% of all data fall into the interval defined by $\bar{\beta} \pm \sigma$, with $\sigma = 0.17$ being the standard deviation. Experimentally, this is almost fulfilled with 4 out of 7 experimental β values being located in this range. However, the data in Fig. 5.12(b) do not appear to represent a random sequence, but instead follow a superimposed parabolic behavior, with a minimum occurring for $x = 0.2$, which suggests the existence of an underlying doping dependence of β. This is especially evident, if one considers the rather small estimated error for each individual data point. Thus, in assessing the reliability of the data analysis, one has to keep in mind that the experimentally determined mean value $\bar{\beta} = 0.73 \pm 0.07$ and its associated standard deviation are derived without the explicit consideration of an x-dependent critical exponent β. In order to further investigate this systematic variation of the experimentally determined critical exponents with the Al concentration x, the absolute moment per hexagonal surface unit, $\langle m \rangle^*$, was determined. Fig. 5.13 shows the experimental $\langle m \rangle^*$ values as a function of x as black circular dots. The green straight line represents the value for a fully polarized hexagonal Cr_2O_3 unit cell at the surface, which was estimated by Binek et al., as an expected limit for the maximum possible BM value [28].

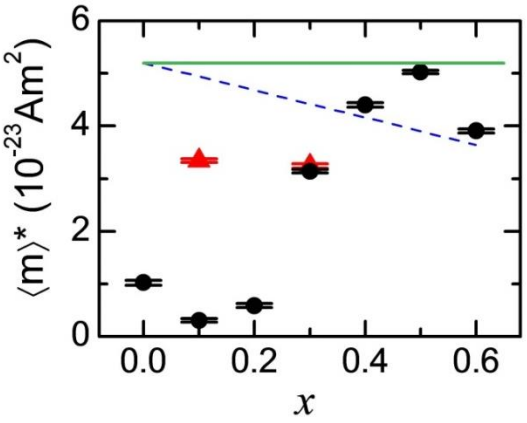

Figure 5.13: Al_2O_3 concentration *x* dependence of the absolute magnetization per hexagonal unit area ⟨*m*⟩*. The black circles represent the values measured at T = 100 K at remanence after magnetic field cooling. The red triangles represent the values measured at 100K in the presence of $\mu_0 H$ = 200 mT after prior field cooling. The straight green line marks the expected value for a fully polarized hexagonal unit cell at the surface for pure Cr_2O_3 [28]. The dashed blue line represents the expected value for a full polarized hexagonal surface unit cell for a randomly mixed $Cr_{2-x}Al_xO_3$ under the assumption that Al does not carry any magnetic moment.

The dashed blue line represents the corresponding value for a fully polarized hexagonal $Cr_{2-x}Al_xO_3$ unit cell under the assumption that Al does not carry any magnetic moment and that the surface layer has the exact same alloy concentration as the film on average. The samples for small *x* show small ⟨m⟩* values, while the high *x* materials exhibit ⟨m⟩* values close to the theoretical expectation for a full uniform surface magnetization. It is hereby important to notice that the entire set of observed ⟨m⟩* values never exceeds the theoretical BM threshold. To understand the strong *x* dependence of ⟨m⟩*, one has to recall that films with low Al concentration possess a lower crystal quality. Specifically, the low *x* samples exhibit a far higher presence of twinned crystallographic domains if compared to the Al-rich, high *x* samples, for which the twinning almost disappears. As reported before, twinned domains can cause the occurrence of different magnetic sublattices at the surface [174]. This suggests a strong connection between twinning and the observable remanent BM: the lower the percentage of twinning is, the more stable will be the magnetization at the boundary after the field cooling procedure. In order to test this hypothesis, in addition to its obvious consistency with the ⟨m⟩* vs. *x* data in Fig. 5.13, the *m*(T) behavior has been measured following the procedure applied for the data in Fig. 5.11, but in the presence of a positive axial field $\mu_0 H = 0.2\,T$ for the $x = 0.1$ and $x = 0.3$ samples. From these measurements, ⟨m⟩* values have been determined in the presence of a magnetic field,

which are shown in Fig. 5.13 as red triangles. The x = 0.3 sample shows a value that is nearly unchanged from its already large remanent value, which means that almost the entire saturation magnetization is retained in the measurement procedure when the field is removed after field cooling in $\mu_0 H = 7\,T$. On the other hand, the x = 0.1 sample shows a substantially enhanced $\langle m \rangle^*$ value upon applying a field, bringing both samples to nearly identical $\langle m \rangle^*$ levels. This can be explained if one assumes that, once the magnetic field is switched off upon the completion of the FC sequence, the surface develops a magnetic multidomains state caused by the twinned crystal domains, but still has a majority of the surface moments pointing in the direction of the originally applied field during the FC sequence. As a consequence, the evaluated exponents β for the low Al concentration samples must be considered to be less reliable, because they are extracted from measurements on multi domain states, even if there still is a net polarized state that follows the previously applied saturation field.

This insight also has to be taken into consideration in the analysis and discussion of the ZFH data of the 26, 50, and 60 nm thick Cr_2O_3 samples in Section 5.4. Also there, the external magnetic field was not sufficient to select a single BM domain state in these pure Cr_2O_3 films. Instead, a multidomain state with a net magnetic moment pointing parallel to the direction of the external applied field was developed by the surface. Nonetheless, it results in a very sharp switching process as shown in Figs. 5.8. and 5.9, which indicates a strongly correlated collective reversal of the entire sample, even if its net moment is reduced in comparison to the ideal of a uniform BM state throughout the entire sample, which can only develop if no structural imperfections, such as the crystallographic twinning, impede it.

5.6. Conclusions

This chapter presents a detailed study of the magnetoelectric antiferromagnet chromia when geometrically confined in the form of a thin film. It is found that in such thin films surface magnetic moments can be reversed solely by magnetic means. This finding is in strong contrast to bulk chromia, where a simultaneous presence of electric and magnetic fields is necessary to achieve reversal of the surface magnetization and the underlying AFM spin structure. The here observed coercive fields show a giant temperature

sensitivity. This property of chromia thin films suggests magnetoelectric antiferromagnets as promising candidates for HAMR by means of storing magnetic bits via the surface magnetization of otherwise antiferromagnetically ordered films.

Furthermore, the effect of Al_2O_3 doping on the structural and magnetic properties of Cr_2O_3 has been investigated in detail. The findings demonstrate the fundamental viability of tuning the critical temperature of chromia-based magnetoelectric antiferromagnets by means of alloying, while preserving the symmetry of the antiferromagnetic order state, as well as the associated existence of the BM. Specifically, the highly oriented epitaxial alloy film samples allow the use of the boundary magnetization as a probe to study the magnetic transition. The critical exponent and the absolute magnetization level of the BM have been evaluated, and are both found to be in good agreement and consistent with the predicted values [28,177-179]. Although the achieved tuning of T_N towards lower ordering temperatures does not directly aid chromia's suitability for technological applications, it is worth highlighting that the study presented here constitutes an actual proof of the fundamental viability of the tuning chromia by alloying with isostructural materials.

The findings here may be expected to extend to other magnetoelectric antiferromagnetic materials and alloys as long as lattice structure and symmetries are equally preserved, which should ultimately enable technological applications of the BM phenomenon by combining its unique properties with a broad material class for novel functional devices.

6. Conclusions and outlooks

This thesis presents detailed research work that is mainly devoted to achieving a better understanding of the influence of crystallographic order, composition and thickness onto the magnetic properties of metallic and oxide thin films.

It has been demonstrated that the effective Curie temperature of a ferromagnetic alloy thin film can be continuously varied as a function of depth via a corresponding compositional gradient over tens of nm. In particular, the here designed graded structure allows for the temperature tuning of the correlation or decorrelation of the magnetic state and reversal behavior. However, over short enough distances, a ferromagnetic system cannot be local and interlayer exchange coupling must start to dominate the effects of the compositional gradient. Understanding this localization limit is important for potential applications, as it dictates the length scale, below which graded material design stops being a viable engineering tool. In order to determine the localization limit for such compositionally graded materials, a series of 100 nm thick $(10\bar{1}0)$ $Co_{1-x}Ru_x$ alloy films have been fabricated, for which x follows an "oscillatory" depth profile produced by a "triangular" dopant content with a wavelength λ that changes from sample to sample.

Preliminary PNR measurements indicate that the magnetization profiles remain strongly modulated, i.e. exhibit "local" behavior for λ = 20 and 10 nm, whereas similar modulations seem to be largely disappearing when λ is reduced to 5 nm. Further work will be needed to clearly identify in which parameter regime ferromagnets behave as if they were defined by their local T_C-structure.

In this thesis, also the nature of three distinct magnetic phases that form the phase diagram of PMA ferromagnetic thin films has been identified. Most importantly, it has been demonstrated that their phase boundaries intersect in a single point, which is

tricritical in nature. A detailed experimental characterization has been presented, which furthermore reveals the possibility of changing the complexity of the phase diagram via temperature or alloying. Triggered by the reduction of the magnetic anisotropy, the disappearance of the *tricritical point* has been induced and observed. While this is a substantial step forward in understanding PMA films it should be mentioned, that the magnetic phase diagram could be more complicated still, because the experimental and theoretical techniques may not be sufficiently sensitive to distinguish different nucleation domain arrays or lattices that could form. Thus, the nucleation domain phase might actually be a superposition of multiple phases, representing different nucleation lattice orders, an aspect that will have to be studied still. Therefore, as future work on this subject, one can envision to extend this type of study to other materials, such as CoPt alloys, which allow the fabrication of materials with low Curie temperature and high magneto-crystalline anisotropy. This would enable a study of the nucleation phase for elevated temperatures near the Curie temperature, in which different nucleation domain lattice order types might occur with sufficient long-range coherence that they can actually be distinguished experimentally.

Furthermore, the work of this thesis has provided experimental evidence that the reversal of the antiferromagnetic order parameter in thin films of magnetoelectric antiferromagnets by pure magnetic means is possible when these types of materials are geometrically confined in thin films. The coercive fields of this reversal phenomenon shows a giant temperature sensitivity, which makes chromia in particular and magnetoelectric antiferromagnetic thin films in general promising candidates for future magnetic media utilization in HAMR technology. Furthermore, the viability of tuning the critical temperature upon alloying pure chromia while preserving its boundary magnetization has been demonstrated. This has been achieved by selecting Al_2O_3 as isostructural dopant material to enable high quality epitaxial film growth and insure conservation of the crystal symmetry. In order to develop suitable materials for technological applications, T_N needs to be actually increased above the chromia bulk value. Therefore, different isostructural materials with higher ordering temperatures could be explored. Specifically, (0001) oriented Cr_2O_3-Fe_2O_3 ($Cr_{2-x}Fe_xO_3$) alloys thin films have been successfully fabricated in the concentration range between $0 \leq x \leq 0.6$. Preliminary

SQUID magnetometry data, however, show a decrease of the critical temperature, even if the BM is preserved. As future work on this subject, one can envision to extend this study to different dopant material such as Co, Gd, Mn that do not necessarily form a isostructural by themselves, but might be compatible with one in an alloy. Moreover, a well-controlled and reproducible process, which guarantees the increase of the ordering temperature, may result in the use of chromia alloys and other ME-AFM for a wide variety of spintronic device applications.

A. Micromagnetic simulations

Extensive micromagnetic simulations using the open-source GPU-accelerated micromagnetic software MuMax3 [180] have been performed by Prof. Dr. Ondrej Hovorka (University of Southampton) to complement the magnetometry and MFM experiments of Chapter 4 and to gain further insight into the nature of the underlying magnetization reversal and domain pattern formation. The micromagnetic model of the sputter deposited film samples consists of a simulation unit cell of size 1 μm × 1 μm in the film plane and 200 nm thickness along the surface normal. Periodic boundary conditions are included by adding 10 cell repetitions in every direction except for along the thickness axis. The finite difference mesh discretization was chosen to produce 256 × 256 × 64 mesh elements, which for the choice of material constants for Co (saturation magnetization $M_S = 1448 \times 10^3$ A/m, and micromagnetic exchange coupling constant $A = 1.5 \times 10^{-11}$ J/m [2]) guaranteed that the discrete mesh feature variation is below the characteristic exchange length in all directions. This specific calculation geometry leads to a mesh resolution that is much finer than the domain width, while at the same time allowing to capture numerous domains within the calculated system size.

Two values of the uniaxial anisotropy constant have been considered, $K = 8 \times 10^4$ J/m^3 and 5.5×10^5 J/m^3, which allowed us to mimic the expected behavior at high and low temperatures. To incorporate non-uniformities that are present in any real thin film sample, random variations of the anisotropy constant around its mean value K have been included into the modeling, as well as local deviations of the anisotropy axis orientation away from the surface normal. Both are described by their respective standard deviations σ_K and σ_θ. To implement this local parameter variation, the in-plane simulation unit cell was divided into 16 × 16 regions and randomized anisotropy values and directions were assigned to every region. To reflect the very high quality of crystallographic ordering in the here prepared epitaxial films, the statistical variations were drawn from Gaussian distribution with narrow standard deviations, namely $\sigma_K = 0.5\%$ and $\sigma_\theta = 0.5°$.

The micromagnetic simulations set up in this way have been used to generate two different types of calculations, namely a magnetization state evolution driven by changing the external field amplitude H at a fixed field angle δ, i.e. the conventional magnetization

reversal process, and a state evolution process driven by changing δ at fixed H. The respective calculations were done by varying either H or δ in small steps always starting from positive saturation, and relaxing the total energy at every step. The optimum step size was chosen by means of reducing it until the calculated behavior no longer changed upon further reduction. Finally, at every value of H and δ, the corresponding domain pattern was exported and its main features analyzed using image processing techniques, which allowed a classification and analysis of the phase space. This also requires the definition of an order parameter that is capable of capturing the qualitative change of the domain structure from the approximately circular shape of nucleation domains to the elongated shape of stripe domains. In order to achieve sufficient insensitivity to inhomogeneities and the apparent irregular shapes of magnetized regions within the domain patterns (see Fig. 4.15(b)), the order parameter *Op* (H,δ) has been defined for any domain pattern corresponding to a specific pair of H and δ as:

$$Op(\mathrm{H},\delta) = \langle r_{g,i} \rangle_{H,\delta} = \frac{1}{N_{sub}} \sum_{i=1}^{N_{sub}} r_{g,i} \Bigg|_{H,\delta} \tag{4.2}$$

where N_{sub} is the number of individual disconnected magnetic subdomain regions *i* with the magnetic moment pointing down (i.e. sub-regions with $m_z < 0$), that are present within the overall pattern at any positive magnetic field value H. Hereby, $r_{g,i}$ is the radius of gyration for sub-region *i*. The $r_{g,i}$ values are calculated in a standard way by discretizing the area of a subdomain *i* into *n* subsections at positions $\vec{r_j}$ and evaluating the sum:

$$r_{g,i}^2 = \frac{1}{2n^2} \sum_{k,l}^{n,n} (\vec{r}_k - \vec{r}_l)^2 \tag{4.3}$$

The order parameter defined in this way vanishes in the presence of a uniform magnetization state, is small but not vanishing for isolated nucleation domains, and exhibits values of the order of the system size for the stripe domain phase.

List of publications

Work related to this thesis has also resulted in the following publications:

L. Fallarino, A. Berger, and Ch. Binek "Giant temperature dependence of the spin reversal field in magnetoelectric chromia" Appl. Phys. Lett. **104**, 022403 (2014).

L. Fallarino, A. Berger, and Ch. Binek "Magnetic field-induced switching of the antiferromagnetic order parameter in thin films of magnetoelectric chromia" Phys. Rev. B. **91**, 054414 (2015).

L. Fallarino, Ch. Binek, and A. Berger "*Boundary magnetization properties of epitaxial* $Cr_{2-x}Al_xO_3$ *thin films*" Phys. Rev. B. **91**, 214403 (2015)

L. Fallarino, O. Hovorka, and A. Berger "Temperature and angular dependence of the tricritical point properties in epitaxial Co (0001) epitaxial thin films" Phys. Rev. B **94**, 064408 (2016).

L. Fallarino, B. J. Kirby, M. Pancaldi, P. Riego, A. L. Balk, C. W. Miller, P. Vavassori, and A. Berger "*Magnetic properties of epitaxial CoCr films with depth-dependent exchange coupling profile*" Submitted to Phys Rev. B. (02.11.2016).

Other publications:

O. Idigoras, U. Palomares, A. K. Suszka, L. Fallarino, and A. Berger "*Magnetic properties of room temperature grown epitaxial* $Co_{1-x}Ru_x$*-alloy films*" Appl. Phys. Lett. **103**, 102410 (2013).

M. Isasa, E. Villamor, L. Fallarino, O. Idigoras, A. K. Suszka, A. Berger, L. E. Hueso and F. Casanova "*Spin transport enhancement by controlling the Ag growth in lateral spin valve*", J. Phys. D: Appl. Phys **48**, 215003 (2015).

C. Gonzalez Fuentes, J. B. Gonzalez-Diaz, L. Fallarino, J. A. Arregi, and A. Berger "*Influence of the light incidence angle on the precision of generalized magneto-optical ellipsometry*", J. Magn. Magn. Mat. **386**, 150 (2015).

L. Pietrobon, L. Fallarino, A. Berger, A. Chuvilin, F. Casanova, and L. E. Hueso "*Weak Delocalization in Graphene on a Ferromagnetic Insulating Film*", Small **11**, 6295 (2015).

L. Fallarino, V. Sluka, B. Kardasz, M. Pinarbasi, A. Berger, and A. D. Kent "*Interlayer exchange coupling between layers with perpendicular and easy-plane magnetic anisotropies*" Appl. Phys. Lett. **109**, 082401 (2016).

Acknowledgments

This is the last chapter of my Ph.D. thesis, and it is really hard putting in words, using few pages, so much appreciation that I have towards many people. It is even harder because I cannot stop thinking, thinking about this last for years of my life, in which I met extraordinary people, people that I definitely want with me in this wonderful journey called life. I still remember my first day in nanoGUNE, when I met Andreas in his office, and I could not realize from the beginning how lucky I was to have him as supervisor. Let me thank you very much Andreas, for giving me the tremendous opportunity to work with you. You are a terrific scientist and advisor, and more important, a great person. I am especially thankful because four years ago you believed in me, and from that moment you always supported and guided me throughout my PhD. You have been able to keep me always motivated especially through the difficulties of experimental science and, more important, daily life. Vielen dank Andreas!!!

I am very grateful to Paolo Vavassori, for many stimulating discussion we had, for being always so helpful and available. Unfortunately we could not have chances to work a lot together, but your smiles and happiness have been so contagious that I am so happy to have had you as a research scientist in the group. Particularly, I would like to thank you very much for your support at the beginning of this experience, you really helped me a lot!

I am extremely thankful to Christian Binek, during the six months you were in nanoGUNE I learned so many things. You introduced me in this so interesting world of magnetic oxides, and I will never forget these nice afternoons in front of the SQUID magnetometer waiting for a magnetic signal.

I must to say that this experience has been definitely shaped by my group members, past and current ones. Their support has been essential. Especially I would like to acknowledge Ania, Olatz, Jon Ander and Patricia for teaching me so many things and for helping me in all the experiments we have done together. I have really learned a lot from you. Many thanks to our technician Cesar for helping me many times doing HF, opening the sputter chamber, and especially with the SQUID system. I would not want to forget thanking Eva, for bringing a breeze of fresh air to the group, Juan, Txema, Ananda, Alberto, and Adrian. Nicolò and Matteo both deserve a special recognition: we have been

sharing many things during our PhDs, and I am really very grateful for the friendship we developed and experienced. I am sure that it is so solid that will continue through our lives.

I am most thankful to the Basque Government for the financial support from the "Programa de Formación de Personal Investigador" promoted by the Department of Education, Universities and Research. This also allowed me to spend a wonderful three months period at the New York University. My thanks go to Andrew D. Kent, who has hosted me visiting his group. I would like also to thank the people from New York, for what I learned there and for making me feel at home during my short stay: Volker, Sohrab, Marion, Eason, Christian, Georg, Jinting, Laura, Gabriel, Yu-Ming, thank you very much dudes!!!!

Thanks to Brian J. Kirby and Ondrej Hovorka for agreeing to read the thesis and giving their feedbacks for the international doctoral mention. Particularly, I am extremely thankful to Brian with which I spent an incredible week measuring our samples at NIST-NCNR and to which I owe big time for all the measurements he performed. At the same time, I would like to thank very much Ondrej for having performed micromagnetic calculations and for having been so supportive and collaborative. Let me tell you that I have really enjoyed working and collaborating with both of you.

I would like to add that I have been really lucky to have Angelique, Andrea and Alvaro as flatmates. You have been my "Donosti" family together with Guido, Raisa and the little Dante. Indelible memories will remain in my mind of those wonderful days spent together laughing, joking, crying, playing, cooking and dancing. I will never forget you!!!

Greetings also to all the rest of people in CIC nanoGUNE, particularly to the nanodevices group members for the nice hours spent together in the labs, to Roger for the technical support. I would like especially to thank Marta, Subir, Jorg, Stefan, Maria, Michele, Oihana, Raul, Mikko, Wiwat, Marco, Luca, Fabiano, Jon, Mano, Estitxu, Miren, Thales, Edu, Amilcar and Saul for the great time we had inside and outside nanoGUNE (I hope I am not forgetting anybody).

Special thanks also to Gorka Pazos, Christopher Tollan, and Ralph Gay for all their help with experimental instruments.

My sincere gratitude to José María Pitarke for the opportunity to work and carry out my experiments at CIC nanoGUNE.

Acknowledgments

Definitely, I would like to thank my family and friends from Città della Pieve for your support, trust and caring: *quattro anni fà presi la decisione di lasciare l'Italia ed il mio amato paese per continuare il mio sogno di fare ricerca. Già, sono veramente volati, mi sembra ieri che stavamo tutti insieme festeggiando la mia laurea...l'inizio è stato difficile, ma poco a poco ho cominciato a capire l'importanza che ha avuto per me questa esperienza. Mi ha permesso di togliermi le bende che avevo agli occhi, capendo finalmente quanto voi, mamma e babbo, siete stati, siete e sarete importanti nella mia vita e quanto vi ami. Nonostante la lontanza, la felicità nei vostri occhi durante le nostre chiamate quotidiane su skype, i caldi abbracci in aeroporto, le vostre lacrime durante le mie partenze (e le mie nascosto in aereo), hanno fatto si che ogni giorno capissi sempre più l'amore che avete per me. E questo ha aiutato a farmi capire quanto vi voglio bene. Semplicemente grazie per essere come siete!!! Allo stesso modo voglio ringraziare delle persone fantastiche che ogni volta che sia tornato nel mio piccolo paese sono sempre state li, aspettandomi come se non me ne fossi mai andato. Grazie mille Luca, Mirko, Giacomo e Federico (e fidanzate), siete fantastici e non posso che augurarvi tutta la felecità possibile nelle vostre vite!!! Non posso non fare un ringraziamento speciale ai miei grandi nonni Esterina, Giuseppe, Averino e Maria, siete stati un esempio di vita per me, ed ai miei zii e cugini.*

Claramente esta tesis es también mérito de una persona súper especial. Gracias Aintz por haber hecho estos últimos cuatro años de mi vida tan fantásticos. Cada día me has hecho sentir la persona más afortunada del mundo.

Lorenzo,

January 2017

Bibliography

[1] N. A. Spaldin, *Magnetic Materials, Fundamentals and Device Applications* (Cambridge University Press, Cambridge, U. K., 2003).

[2] G. Bertotti, *Hysteresis in Magnetism, for Physicists, Materials Scientists, and Engineers* (Academic Press, Inc, San Diego, California, 1998).

[3] S. Blundell, *Magnetism in Condensed Matter* (Oxford University Press, Oxford, U. K., (2006).

[4] S. Bandyopadhyay and M. Cahay, *Introduction to Spintronics* (CRC Press Taylor & Francis Group, Boca Raton, Florida, 2008).

[5] B. D. Cullity and C. D. Graham, *Introduction to Magnetic Materials* (IEEE Press, Wiley, Hoboken, New Jersey, 2009).

[6] C. Kittel, Rev. Mod. Phys. **21**, 541 (1949).

[7] J. M. D. Coey, *Magnetism and Magnetic Materials* (Cambridge University Press, Cambridge, U. K., 2010).

[8] A. Hubert and R. Shafer, *Magnetic Domains: The Analysis of Magnetic Microstructures* (Springer Verlag, Berlin, Germany, 1998).

[9] L. Landau and E. Lifshits, Phys. Zeitsch. der Sow. **8**, 153 (1935).

[10] E. C. Stoner and E. P. Wohlfarth, Philosophical Transactions of the Royal Society A: Mathematical, Physical and Engineering Sciences **240**, 599 (1948).

[11] A. Aharoni, Rev. Mod. Phys. **34,** 227 (1962).

[12] W. F. Brown, *Micromagnetics* (Wiley, New York, 1963).

[13] R. Skomski, J. Phys.: Condens. Matter **15**, R841(2003).

[14] S. Chikazumi and C. D. Graham, *Physics of Ferromagnetism* (Oxford University Press, Oxford, U. K.,1997).

[15] L. Duò, L. M. Finazzi, and F. Ciccacci, *Magnetic Properties of Antiferromagnetic Oxide Materials* (Wiley VCH, Weinheim, Germany, 2010).

[16] C. G. Shull, W. A. Strauser, and E. O. Wollan, Phys. Rev. **83**, 333 (1951).

[17] Y. Y. Li, Phys. Rev. **101**, 1450 (1956).

[18] J .Volger, Nature **170**, 1027 (1952)**.**

[19] B. N. Brockhouse, J. Chem. Phys. **21**, 961 (1953).

[20] R. W. G. Wyckoff, *Crystal Structures* (Interscience Publishers. Inc., New York, 1948).

[21] A. Kilian, F. Bernardi, A. Pancotti, R. Landers, A. de Siervo, and J. Morais, J. Phys. Chem. C **118**, 20452 (2014).

[22] S. Shi, A. L. Wysocki, and K. D. Belashchenko, Phys. Rev. B **79**, 104404 (2009).

[23] I. E. Dzyaloshinskii, Sov. Phys. JETP **10**, 628 (1959).

[24] D. N. Astrov, Sov. Phys. JETP **11**, 708 (1960); **13**, 729 (1961).

[25] V. J. Folen, G. T. Rado, and E. W. Stalder, Phys. Rev. Lett. **6**, 607 (1961).

[26] T. H. O'Dell, *The Electrodynamics of Magneto-Electric Media* (North-Holland, Amsterdam, Netherlands, 1970).

[27] K. D. Belashchenko, Phys. Rev. Lett. **105**, 147204 (2010).

[28] X. He, Y. Wang, N. Wu, A. N. Caruso, E. Vescovo, K. D. Belashchenko, P. A. Dowben, and Ch. Binek, Nat. Mater. **9**, 579 (2010).

[29] N. Wu, X. He, A. L. Wysocki, U. Lanke, T. Komesu, K. D. Belashchenko, Ch. Binek, and P. A. Dowben, Phys. Rev. Lett. **106**, 087202 (2011).

[30] R. Wiesendanger, H. J. Güntherodt, G. Güntherodt, R. J. Gambino, and R. Ruf, Phys. Rev. Lett. **65**, 247 (1990).

[31] J. A. Kelber, Ch. Binek, P. A. Bowden, and K. D. Belashchenko, *U.S. Patent Application No. 14/182 521* (2014).

[32] P. Borisov, T. Ashida, T. Nozaki, M. Sahashi, and D. Lederman, Phys. Rev. B **93**, 174415 (2016)

[33] J. L. Wang, J. A. Colon Santana, N. Wu, C. Karunakaran, J. Wang, P. A. Dowben, and Ch. Binek, J. Phys.: Condens. Matter **26**, 055012 (2014).

[34] K. Seshan, *Handbook of Thin-Film Deposition Processes and Techniques*, 2nd ed., (Noyes Publications/William Andrew Publishing, Norwich, New York, 2002).

[35] D. L. Smith, *Thin-Film Deposition: Principles and Practice* (McGraw-Hill Inc., New York, 1995).

[36] K. Wasa and S. Haykawa, *Handbook of Sputter Deposition Technology: Principles, Technology and Applications* (Noyes Publication, New Jersey, 1992).

[37] J. S. Chapin, *U.S. Patent Application No. 4, 166 018* (1979).

[38] P. J. Kelly and R. Arnell, Vacuum **56**, 159 (2000).

[39] F. Adibi, I. Petrov, J. E. Greene, L. Hultman, and J. E. Sundgren, J. Appl. Phys. **73**, 8580 (1993).

[40] M. Birkholz, *Thin Film Analysis by X-ray Scattering* (Wiley-VCH, Weinheim, Germany, 2006).

[41] B. D. Cullity and S. R. Stock, *Elements of X-ray Diffraction* (Prentice Hall, New Jersey, 2001).

[42] M. Yasaka, J. Rigaku **26**, 1 (2010).

[43] E. Meyer, H. J. Hug, and R. Bennewitz, *Scanning Probe Microscopy: The Lab on a Tip* (Springer, New York, 2004).

[44] G. Haugstad, *Atomic Force Microscopy Understanding Basic Modes and Advanced Applications* (John Wiley & Sons, Ltd, New Jersey, 2012).

[45] S. Foner, Rev. Sci. Instrum., **30**, 548 (1959).

[46] F. Fiorillo, Metrologia **47**, S114 (2010).

[47] J. Clarke and A. I. Braginski, *The SQUID handbook* (Wiley-VCH, Weinheim, Germany, 2004).

[48] http://www.qdusa.com/products/mpms3.html

[49] M. J. Freiser, IEEE Trans. Mag. **4**, 152 (1968).

[50] S. Visnovsky, Czech. J. Phys. B **36**, 625 (1986).

[51] Z. Q. Qiu and S. D. Bader, Rev. Sci. Instrum. **71**, 1243 (2000).

[52] C. Y. You and S. C. Shin, J. Appl. Phys. **84**, 541 (1998).

[53] P. Vavassori, Appl. Phys. Lett. **77**, 1605 (2000).

[54] C. F. Majkrzak, Physica B **173**, 75 (1991).

[55] J. F. Ankner, G. P. Felcher, J. Magn. Magn. Mat. **200**, 741 (1999).

[56] C. F. Majkrzak, K. V. O'Donovan, and N. F. Berk, in Neutron Scattering from Magnetic Materials, edited by T. Chatterji (Elsevier Science, New York, 2005).

[57] B. J. Kirby, P. A. Kienzle, B. B. Maranville, N. F. Berk, J. Krycka, F. Heinrich, and C. F. Majkrzak, Curr. Opin. Colloid Interface Sci. **17**, 44 (2012).

[58] in ISO/IEC Guide 98-3-:2008/Suppl 1:2008, Propagation of distributions using a Monte Carlo method (International Organization for Standardization, Geneva, Switzerland, 2008) 1st ed.

[59] J. A. Vrugt, C. J. F. ter Braak, C. G. H. Diks, B. A. Robinson, J. M. Hyman, and D. Higdon, Int. J. Nonlinear Sci. Numer. Simul. **10**, 273 (2009).

[60] G. P. Felcher, Physica B **267**, 154 (1999).

[61] R. E. Camley and R. L. Stamps, J. Phys.: Condens. Matter **5**, 3727 (1993).

[62] I. Žutić, J. Fabian, and S. D. Sarma, Rev. Mod. Phys. **76**, 323 (2004).

[63] C. A. Ramos, D. Lederman, A. R. King, and V. Jaccarino, Phys. Rev. Lett. **65**, 2913 (1990).

[64] U. Bovensiepen, F. Wilhelm, P. Srivastava, P. Poulopoulos, M. Farle, A. Ney, and K. Baberschke, Phys. Rev. Lett. **81**, 2368 (1998).

[65] R. Skomski and D. J. Sellmyer, J. Appl. Phys. **87**, 4756 (2000).

[66] M. Pärnaste, M. Marcellini, and B. Hjörvarsson, J. Phys.: Condens. Matter **17**, L477 (2005).

[67] E. Kneller and R. Hawig, IEEE Trans. Magn. **27**, 3588 (1991).

[68] J. Barnas, Phys. Rev. B **45**, 10427 (1992).

[69] R. Skomski and J. M. D. Coey, Phys Rev. B **48**, 15812 (1993).

[70] E. E. Fullerton, J. S. Jiang, M. Grimsditch, C. H. Sowers, and S. D. Bader, Phys. Rev. B **58**, 12193 (1998).

[71] E. E. Fullerton, J. S. Jiang, and S. D. Bader, J. Magn. Magn. Mat. **200**, 392 (1999).

[72] D. C. Crew, J. Kim, L. H. Lewis, K. Barmak, J. Magn. Magn. Mater. **233**, 257 (2001).

[73] J. S. Jiang and S. D. Bader, J. Phys.: Condens. Matter **26**, 064214 (2014).

[74] J. S. Jiang, J. E. Pearson, Z. Y. Liu, B. Kabius, S. Trasobares, D. J. Miller, S. D. Bader, D. R. Lee, D. Haskel, G. Srajer, and J. P. Liu, J. Appl. Phys. **97**, 10K311 (2005).

[75] J. P. Wang, W. K. Shen, and J. M. Bai, IEEE Trans. Magn. **41**, 3181 (2005).

[76] D. Suess, T. Schrefl, F. S. Fähler, M. Kirschner, G. Hrkac, F. Dorfbauer and J. Fidler, Appl. Phys. Lett. **87**, 012504 (2005).

[77] R. H. Victora and X. Shen, IEEE Trans. Magn. **41**, 537 (2005).

[78] D. Suess, Appl. Phys. Lett. **89**, 113105 (2006).

[79] A. Berger, N. Supper, Y. Ikeda, B. Lengsfield, A. Moser, and E. E. Fullerton, Appl. Phys. Lett. **93**, 122502 (2008).

[80] D. Suess, J. Fidler, G. Zimanyi, T. Schrefl, and P. Visscher, Appl. Phys. Lett. **92**, 173111 (2008).

[81] D. Goll, A. Breitling, L. Gu, P. A. van Aken, and W. Sigle, J. Appl. Phys. **104**, 083903 (2008).

[82] M. Morcellini, M. Pärnaste, B. Hjörvarsson, and M. Wolff, Phys. Rev. B **79**, 144426 (2009).

[83] T. J. Zhou, B. C. Lim, and B. Liu, Appl. Phys. Lett. **94**, 152505 (2009).

[84] B. J. Kirby, J. E. Davies, K. Liu, S. M. Watson, G. T. Zimanyi, R. D. Shull, P. A. Kienzle, and J. A. Borchers, Phys. Rev. B **81**, 100405 (2010).

[85] B. J. Kirby, S. M. Watson, J. E. Davies, G. T. Zimanyi, K. Liu, R. D. Shull, and J. A. Borchers, J. Appl. Phys. **105**, 07C929 (2009).

[86] V. Alexandrakis, D. Niarchos, K. Mergia, J. Lee, J. Findler, and I. Panagiotopoulos, J. Appl. Phys. **107**, 013903 (2010).

[87] J. S. Chen, L. S. Huang, J. F. Hu, G. Ju, and G. M. Chow, J. Phys. D: Appl. Phys. **43**,185001 (2010).

[88] V. Bonanni, Y. Fang, R. K. Dumas, C. Zha, S. Bonetti, J. Nogues, and J. Akermann, Appl. Phys. Lett. **97**, 202501 (2010).

[89] C. L. Zha, R. K. Dumas, Y. Fang, V. Bonanni, J. Nogues, and J. Akerman, Appl. Phys. Lett. **97**, 182504 (2010).

[90] R. K. Dumas, Y. Fang, B. J. Kirby, C. Zha, V. Bonanni, J. Nogues, and J. Akerman, Phys. Rev. B **84**, 054434 (2011).

[91] Y. Fang, R. K. Dumas, C. I. Zha, and J. Akermann, IEEE Magn. Lett. **2**, 5500104 (2011).

[92] C. Le Graët, T. R. Charlton, M. McLaren, M. Loving, S. A. Morley, C. J. Kinane, R. M. D. Brydson, L. H. Lewis, S. Langridge, and C. H. Marrows, APL Mater. **3**, 041802 (2015).

[93] B. J. Kirby, H. F. Belliveau, D. D. Belyea, P. A. Kienzle, A. J. Grutter, P. Riego, A. Berger, and C. W. Miller, Phys. Rev. Lett **116**, 047203 (2016).

[94] S. Honda, K. Takahashi, and T. Kusuda, Jap. J. Appl. Phys. **26**, L593 (1987).

[95] N. Inaba, M. Futamoto, and A. Nakamura, IEEE Trans. Magn. **34**, 1558 (1998).

[96] N. Inaba, Y. Uesaka, and M. Futamoto, IEEE Trans. Magn. **36**, 54 (2000).

[97] W. Yang, D. N. Lambeth, and D. E. Laughlin, J. Appl. Phys. **85**, 4723 (1999); **87**, 6884 (2000).

[98] O. Idigoras, U. Palomares, A. K. Suszka, L. Fallarino, and A. Berger, Appl. Phys. Lett. **103**, 102410 (2013).

[99] O. Idigoras, A. K. Suszka, P. Vavassori, B. Obry, B. Hillebrands, P. Landeros and A. Berger, J. Appl. Phys. **115**, 083912 (2014).

[100] J. A. Arregi, J. B. Gonzalez-Dıaz, O. Idigoras, and A. Berger, Phys. Rev. B **92**, 184405 (2015).

[101] M. Grimsditch, E. E. Fullerton, and R. L. Stamps, Phys. Rev. B **56**, 2617 (1997).

[102] F. Ilievski, J. C. Perkinson, and C. A. Ross, J. Appl. Phys. **101**, 09D116 (2007).

[103] R. Schäfer , J. Magn. Magn. Mat. **148**, 226 (1995).

[104] A. Berger, A. Inomata, J. S. Jiang, J. E. Pearson, and S. D. Bader, Phys. Rev. Lett. **85**, 4176 (2000).

[105] J. A. Arregi, O. Idigoras, P. Vavassori, and A. Berger, Appl. Phys. Lett. **100**, 262403 (2012).

[106] I. S. Anderson, P. J. Brown, J. M. Carpenter, G. Lander, R. Pynn, J. M. Rowe, O. Schärpf, V. F. Sears, and B. T. M. Willis, *International Tables for Crystallography* (Wiley, Hoboken, New Jersey, 2006) Chap. 4.4, p. 430.

[107] C. F. Majkrzak, C. Metting, B. B. Maranville, J. A. Dura, S. Satija, T. Udovic, and N. F. Berk, Phys. Rev. A **89**, 033851 (2014).

[108] W. Cain, A. Payne, M. Baldwinson, and R. Hempstead, IEEE Trans. Magn. **32**, 97 (1996).

[109] S. N. Piramanayagam, J. Appl. Phys. **102**, 011301 (2007).

[110] T. Garel and S. Doniach, Phys. Rev. B **26**, 325 (1982).

[111] D. J. Singh, Phys. Rev. B **44**, 7451 (1991).

[112] R. Allenspach, J. Magn. Magn. Mat. **129**, 160 (1994).

[113] K. De'Bell, A. B. MacIsaac, and J. P. Whitehead, Rev. Mod. Phys. **72**, 225 (2000).

[114] C. Kittel , Phys. Rev. **70**, 965-971 (1946).

[115] C. Kooy and U. Enz, Philips Res. Rep. **15**, 7 (1960).

[116] M. W. Muller, Phys. Rev. **122**, 1485 (1961); W. F. Brown Jr., Phys. Rev. **124**, 1348 (1961).

[117] P. J. Grundy, D. C. Hothersall, G. A. Jones, B. K. Middleton, and R. S. Tebble, Phys. Status Solidi (a) **9**, 79 (1972).

[118] C. Chappert, K. Le Dang, P. Beauvillain, H. Hurdequint, and D. Renard, Phys. Rev. B **34**, 3192 (1986).

[119] D. Pescia, M. Stampanoni, G. L. Bona, A. Vaterlaus, R. F. Willis and F. Meier, Phys. Rev. Lett. **58**, 2126 (1987).

[120] C. Liu, E. R. Moog and S. D. Bader, Phys. Rev. Lett. **60**, 2422 (1988).

[121] T. Beier, H. Jahrreiss, D. Pescia, Th. Woike and W. Gudat, Phys. Rev. Lett. **61**, 1875 (1988).

[122] R. Allenspach, M. Stampanoni, and A. Bischof, Phys. Rev. Lett. **65**, 3344 (1990).

[123] R. Allenspach and A. Bischof, Phys. Rev. Lett. **69**, 3385 (1992).

[124] B. Schulz and K. Baberschke, Phys. Rev. B **50**, 18 (1994).

[125] A. Berger, A.W. Pang and H. Hopster, J. Magn. Magn. Mater. **137**, L1 (1994).

[126] A. Berger, A.W. Pang and H. Hopster, Phys. Rev. B **52**, 1078 (1995).

[127] A. Berger and H. Hopster, J. Appl. Phys. **79**, 5619 (1996).

[128] D. M. Donnet, K. M. Krishnan, and A. Yajima, J. Phys. D: Appl. Phys. **28**, 1942 (1995).

[129] F. Gregg, W. Allen, K. Ounadjela, M. Viret, M. Hehn, S. M. Thompson, and J. M. D. Coey, Phys. Rev. Lett. **77**, 1580 (1996).

[130] M. Hehn, K. Ounadjela, R. Ferré, W. Grange, and F. Rousseaux, Appl. Phys. Lett. **71**, 2833 (1997).

[131] J. U. Thiele, L. Folks, M. F. Toney, and D. K. Weller, J. Appl. Phys. **84**, 5686 (1998).

[132] R. L. Stamps and B. Hillebrands, Phys. Rev. B **43**, 3532 (1991).

[133] O. Portmann, A. Vaterlaus, and D. Pescia, Nature **422**, 701 (2003).

[134] G. Leaf, H. Kaper, M. Yan, V. Novosad, P. Vavassori, R. E. Camley, and M. Grimsditch, Phys. Rev. Lett. **96**, 017201 (2006).

[135] P. Landeros, R. E. Arias, and D. L. Mills, Phys. Rev. B **77**, 214405 (2008).

[136] J. Brandenburg, R. Hühne, L. Schultz, and V. Neu, Phys. Rev. B **79**, 054429 (2009).

[137] N. Saratz, A. Lichtenberger, O. Portmann, U. Ramsperger, A. Vindigni, and D. Pescia, Phys. Rev. Lett. **104**, 077203 (2010).

[138] M. Hehn, S. Padovani, K. Ounadjela, and J. P. Bucher, Phys. Rev. B **54**, 3428 (1996).

[139] M. Hehn, K. Cherifi-Khodjaoui, K. Oundjela, J. P. Bucher, and J. Arabski, J. Magn. Magn. Mater. **165**, 520 (1997).

[140] M. Kisielewski, A. Maziewski, and V. Zablotski, J. Magn. Magn. Mater. **316**, 277 (2007).

[141] O. Donzelli, M. Bassani, F. Spizzo, and D. Palmeri, J. Magn. Magn. Mater. **320**, e261 (2008).

[142] N. Bergeard, J. P. Jamet, A. Mougin, J. Ferré, J. Gierak, E. Bourhis, and R. Stamps, Phys. Rev. B **86**, 094431 (2012).

[143] J. Gao, S. Tang, Y. Li, W. Xia, T. Tang, and Y. Du, J. Appl. Phys. **112**, 073913 (2012).

[144] A. K. Suszka, A. Etxebarria, O. Idigoras, D. Cortés-Ortuño, P. Landeros, and A. Berger, Appl. Phys. Lett. **105**, 222402 (2014).

[145] O. Kitakami, N. Kikuchi, S. Okamoto, Y. Shimada, K. Oikawa, Y. Otani, and K. Fukamichi, J. Magn. Magn. Mat. **202**, 305 (1999).

[146] I. Zana, G. Zangari, and M. Shamsuzzoha, J. Magn. Magn. Mat. **292**, 266 (2005).

[147] T. Shimatsu, H. Sato, Y. Okazaki, H. Aoi, H. Muraoka, Y. Nakamura, S. Okamoto, and O. Kitakami, J. Appl. Phys. **99**, 08G908 (2006).

[148] D. M. Paige, B. Szpunar, and B. K. Tanner, J. Magn. Magn. Mater. **44**, 239 (1984).

[149] I. S. Lee, H. Rhu, H. J. Lee, and T. D. Lee, J. Appl. Phys. **85**, 6133 (1999).

[150] D. Weller, H. Brändle, G. Gorman, C. J. Lin, and H. Notarys, Appl. Phys. Lett. **61**, 2726 (1992).

[151] S. Okamoto, N. Kikuchi, O. Kitakami, T. Miyazaki, Y. Shimada, and K. Fukamichi, Phys. Rev. B **66**, 024413 (2002).

[152] J. U. Thiele, K. R. Coffey, M. F. Toney, J. A. Hedstrom, and A. J. Kellock, J. Appl. Phys. **91**, 10 (2002).

[153] A. Sato, S. Nakagawa, and M. Takahashi, IEEE Trans. Magn. **36**, 2387 (2000).

[154] N. Honda, J. Ariake, K. Ouchi, and S. Iwasaki, IEEE Trans. Magn. **30**, 4023 (1994).

[155] S. Oikawa, A. Takeo, T. Hikosaka, and Y. Tanaka, IEEE Trans. Magn. **36**, 2393 (2000).

[156] Y. Inaba, T. Shimatsu, T. Oikawa, H. Sato, H. Aoi, H. Muraoka, and Y. Nakamura, IEEE Trans. Magn. **40**, 2486 (2004).

[157] G. A. Bertero, D. Wachenschwanz, S. Malhotra, S. Velu, B. Bian, D. Stafford, W. Yan, T. Yamashita, and S. X. Wang, IEEE Trans. Magn. **38**, 1627 (2002).

[158] H. Gong, M. Rao, D. E. Laughlin, and D. N. Lambeth, J. Appl. Phys. **85**, 4699 (1999).

[159] Ch. Binek and B. Doudin, J. Phys.: Condens. Matter **17**, L39 (2005).

[160] M. Fiebig, J. Phys. D: Appl. Phys. **38**, R123 (2005).

[161] T. J. Martin and J. C. Anderson, IEEE Trans. Magn. **2**, 446 (1966).

[162] A. F. Andreev, JETP Lett. **63**, 758 (1996).

[163] S. Cao, X. Zhang, N. Wu, A.T. N'Diaye, G. Chen, A. K. Schmid, X. Chen, W. Echtenkamp, A. Enders, Ch. Binek, and P. A. Dowben, New J. Phys. **16,** 073021 (2014).

[164] S. Y. Jeong, J. B. Lee, H. Na, and T. Y. Seong, Thin Solid Films **518**, 4813 (2010).

[165] S. Foner and M. Hanabusa, J. Appl. Phys. **34**, 1246, (1963).

[166] Y. Kitaoka, K. Nakamura, T. Akiyama, and T. Ito, J. Cryst. Growth **362**, 42 (2013).

[167] F. Bondioli, A. M. Ferrari, C. Leonelli, and T. Manfredini, L. Linati and P. Mustarelli, J. Am. Ceram. Soc. **83**, 2036 (2000).

[168] V. A. Drebushchak and A. I. Turkin, J. Therm. Anal. Cal. **90**, 795, (2007).

[169] S. H. Yang, S. J. Liu, Z. H. Hua, and S. G. Yang, J. Alloys Compd. **509**, 6946, (2011).

[170] T. Ashida, T. Oida, M. Shimomura, N. Nozaki, T. Shibata, and M. Sahashi, Appl. Phys. Lett. **104**, 152409 (2014).

[171] H. Mashiko, T. Oshima, and A.Ohtomo, Jpn. J. Appl. Phys. **51**, 11PG11 (2012).

[172] F. S. Stone and J. C. Vickerman, Trans. Faraday Soc. **67**, 316-328 (1971).

[173] Y. K. Ahn, J. G. Seo, and J. W. Park, J. Cryst. Growth **326**, 45 (2011).

[174] N. Iwata, T. Kuroda, and H. Yamamoto, Jpn. J. Appl. Phys. **51**, 11PG12 (2012).

[175] J. U. Thiele, K. R. Coffey, M. F. Toney, J. A. Hedstrom, and A. J. Kellock, J. Appl. Phys. **91**, 6595 (2002)

[176] X. He, W. Echtenkamp, and Ch. Binek, Ferroelectrics **426**, 81 (2012).

[177] K. Binder and P. C. Hohenberg, Phys. Rev. B **9**, 2194 (1974).

[178] K. Binder and D. P. Landau, Phys. Rev. Lett. **52**, 318 (1984).

[179] D. P. Landau and K. Binder, Phys. Rev. B. **41**, 4633 (1990).

[180] A. Vansteenkiste, J. Leliaert, M. Dvornik, M. Helsen, F. Garcia-Sanchez, and B. Van Waeyenberge, AIP Advances **4**, 107133 (2014).